UNIVERSITÀ DEGLI STUDI DI TRIESTE

XXIX CICLO DEL DOTTORATO DI RICERCA IN FISICA

GROWTH AND PROPERTIES OF GRAPHENE BASED MATERIALS

Settore scientifico-disciplinare: FIS/03

DOTTORANDO
DAVIDE CURCIO

COORDINATORE
PROF. LIVIO LANCERI

SUPERVISORE DI TESI
PROF. ALESSANDRO BARALDI

ANNO ACCADEMICO 2016/2017

UNIVERSITY OF TRIESTE

Department of Physics

Graduate School in Physics, Cycle XXIX

PhD Thesis

Growth and Properties of Graphene-Based Materials

Supervisor:
Prof. Alessandro Baraldi

Candidate:
Davide Curcio

Academic Year 2016-2017

A Jessica.

Contents

Chapter 1

Introduction

Material science has been, ever since its ancient beginnings, one of the driving forces behind technological innovation. When a material with new, revolutionary properties is discovered, it is always an upheaval for all the fields of technology. And when the new material is as exceptional as graphene, the scientific community becomes truly captured.

This material has been observed in its free standing phase for the first time in 2004 by A. Geim and K. Novoselov, for which they were awarded the Nobel Prize in Physics in 2010. Single layers of graphite on transition metals have been known to exist long before, probably being created for the first time as far back as 1962 [1]. However, it did not become a "hot topic" until the 2000s, when the surface science technology was more mature, and the interest shifted from carbon nanotubes and fullerenes towards their constituent material, graphene. Interestingly, its thermodynamic instability was proven by Landau [2] and later also by Mermin [3], demonstrating how nature always finds ways to surprise us with unexpected new things. Regarding graphene, it is composed by a single layer of sp^2 hybridized carbon atoms, forming a honeycomb lattice. This material has incredible properties, such that it sometimes becomes hard to think of it as a nanometric material: the one-atom thick layer of carbon is so strong it can behave as a macroscopic sheet of fabric, theoretically being able to support 4 kg for a 1 m^2 sheet, while only weighing 4 mg. It is, in fact, the strongest material known to date (by weight). This is due to the strong, sp^2 hybridized C-C bonds that exist between the constituent atoms, and also to the honeycomb structure. Furthermore, it generally grows with a high degree of perfection, with exceptionally low density of defects. This results in an intrinsic strength of 130 GPa [4], 500 times that of structural steel, and so rigid it has Young's modulus of 1 TPa [4], 10 times that of aeronautic grade aluminum. Also, it also has a negative thermal expansion coefficient, due to the same reasons it can exist in the first place: even though the material is 2 dimensional,

it lives in a 3 dimensional world, and the vibrations of the carbon atoms out of plane make it shrink as the temperature rises [5].

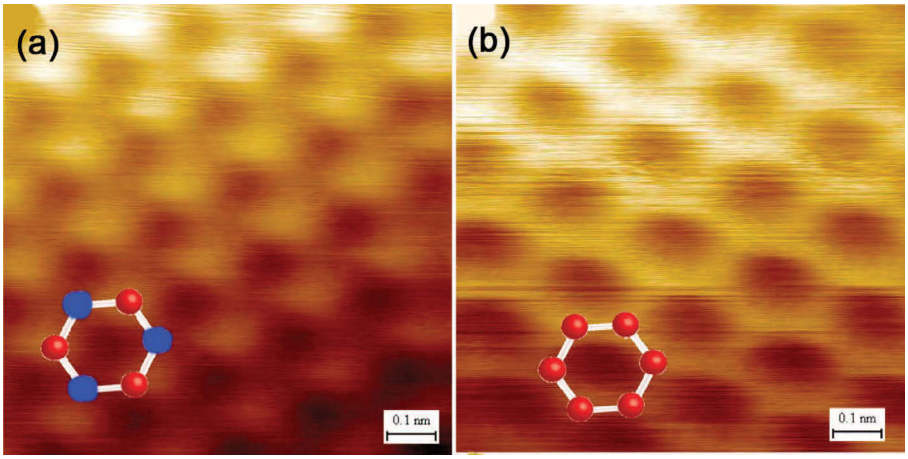

Figure 1.1: (a) STM image of a graphite sample displaying only the three carbon atoms in the unit cell with no neighbor in the layer below. (b) In contrast, all six carbons in the honeycomb structure are equivalent and thus visible in mechanically exfoliated single-layer graphene. Source: Reproduced from Ref. [6].

Another incredible property of graphene is its inertness. For surface scientists, it is unusual to find materials whose atomic structure is preserved when the material is exposed to air: usually such high pressures not only cause atomic surfaces to be completely covered by thick layers of contaminants, but also mechanically destroy the surface order. Graphene will happily survive exposure to air [7], making it an ideal candidate for preservation of more delicate surfaces.

Finally, the electronic structure of graphene is truly unique. In fact, as already predicted in 1947 [8], the electronic dispersion at the Γ points (also known as Dirac points) is linear. When considering the graphene lattice, this linear dispersion gives rise to the Dirac cones, which are one of the defining characteristics for free standing graphene. The dispersion lines at the Dirac point cross each other at the Fermi energy (in free standing graphene), so that the density of states at the Fermi level is null, but so is the bandgap energy: graphene is a degenerate semiconductor. This is both a disadvantage and a benefit: in order to build high performing devices, a bandgap needs to exist. However, the peculiar dispersion relation gives graphene amazing electrical properties: it has a theoretical carrier mobility that is of $10^5\,\mathrm{cm}^2/\mathrm{Vs}$ [10], about 2000 times that of electrons in copper, and 80 times that of electrons in silicon. Also, because of the linear dispersion relation, the carriers behave in the same way as massless Fermions, obeying the Dirac equation rather than the canonical Schrödinger equation, with the speed of light replaced by the Fermi velocity.

With these impressive features, it is surprising that graphene has not revo-

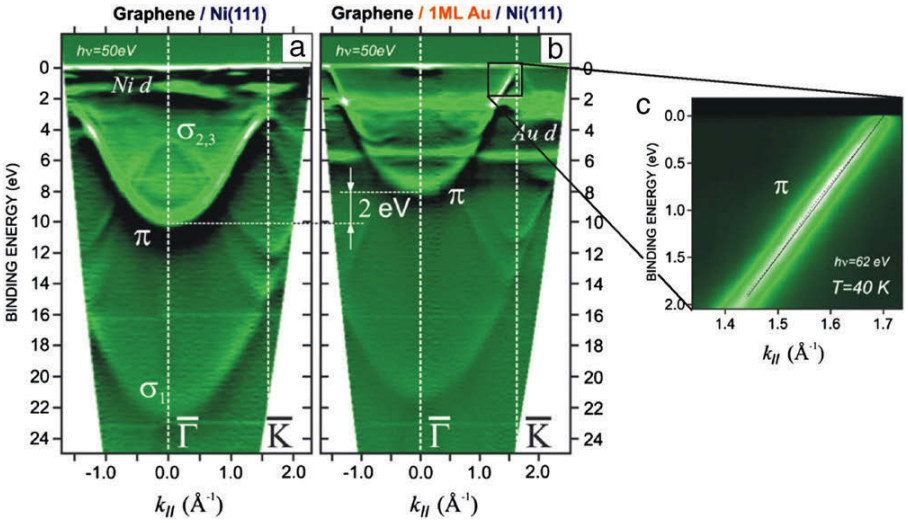

Figure 1.2: ARPES measurement of graphene grown on Ni(1 1 1) before (a) and after (b) intercalation of a monolayer of Au. The linear band dispersion at the Dirac point after Au-intercalation is highlighted in (c). For graphene on Ni the π band is downshifted by 2 eV. Intercalation of Au decouples graphene from the Ni-substrate and forms electronically quasi-freestanding graphene. Source: Reproduced from Ref. [9].

lutionized all sectors of the manufacturing industry, from electronics to high performing mechanical objects. All of graphene's amazing properties rely on the complete absence of defects, the same defects that are currently exploited to try and induce a bandgap by functionalization. Furthermore, silicon and other already well established technologies allow for better, faster, and more reliable transistors than have been ever fabricated with graphene. The idea is then that perfect materials with an innate bandgap should be used instead of graphene. An example are 2D dichalcogenides, and this is an emerging field in physics. But the industry needs better, easier alternatives with an easily engineerable electronic band structure, that will allow new materials to finally be truly competitive with already established technologies. In this respect, it is possible that nano-scale manipulation of these novel materials will be the key to a new era of electronics.

Nanotechnology is all about building things: many materials can be exploited as a starting point, and graphene seems like the most promising for the reasons outlined above. This approach is likely to progress to the point that mass produced atomic scale manufacturing will become possible, simply because the physics allows it. Nanotechnology is the natural development of the never ending process by which with the available tools we build better, more refined, and more precise tools, advancing technology from crude utensils to the brink of atomic manipulation. The idea of building things with a

material as a means for obtaining objects with engineered properties, different from those of the original material, is then an old one, if seen in this light. In our case, we focused on graphene-based nanostructures as a versatile means of manipulating the electronic properties of graphene, while working with objects perfect at the atomic level. This is the nanotechnological approach, where we exploit the infinite possibilities of making small things with a material that, in many instances, surprises us with unexpected behaviors.

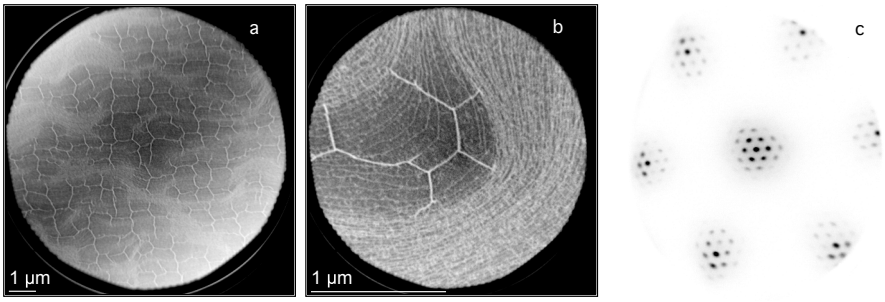

Figure 1.3: (a) LEEM image of graphene grown on Ir(1 1 1) at the Nanospectroscopy beamline of Elettra, with grain boundaries showing as white lines. In (b) a closeup of a single crystal grain, revealing terraces of the Ir surface below the graphene layer and graphene grain boundaries aligned with the crystallographic directions. (c) LEED image for the sample in (a) and (b) showing a large number of satellite spots around the (0,0) spot that are generated by the moiré superlattice, an indication of the high degree of perfection of the graphene layer.

I concentrated my research efforts on graphene-based nanomaterials, because graphene is one of the most exciting materials we have to date, and because manipulation of surfaces at the nano-level is what allows us to make new materials today. In this thesis, I will show how we have created and studied new graphene-based nanostructures by employing cutting-edge surface science techniques. Most of the experimental data we have acquired has been given a new light by powerful Density Functional Theory calculations, that allow for an approach where hardly accessible data (experimentally) becomes indirectly known through numerical calculations, while providing valuable feedback for further aimed calculations. I will show how we have undertaken a route that takes us from a detailed study of how carbon monomers, the building blocks of graphene, come to exist on an Ir(1 1 1) surface after ethylene dissociation. Next, simple nanostructures known as moiré patterns have been exploited, so that the properties of a preexisting graphene layer are manipulated by intercalating different metals between graphene and the substrate. Then I will discuss an experiment where graphene was grown on a highly anisotropic substrate, Ru(1 0 $\bar{1}$ 0), which proved to be an extremely rich system, giving rise to several self-assembled graphene nanostructures, including nanoribbons and one-dimensional quasi free-standing graphene waves. Then, we will progress

to what are commonly perceived as being proper graphene-based nanostructures. We have, in fact, managed to create size selected graphene nanodomes on Ir(1 1 1) using coronene as a precursor, and we have understood many details of the dynamics in the formation of these carbon-based nanostructures, discovering that in certain steps of the reaction they lift from the surface and rotate, before settling in the definitive adsorption position. Furthermore, while performing similar experiments on pentacene (a semiconducting molecule, used the fabrication of molecular FETs) on Ir(1 1 1), we have discovered that the molecules exhibit a reversible dehydrogenation, allowing for a switch between semiconducting molecules and minimalistic graphene nanoribbons, only one aromatic ring wide.

Finally, a size-selected nanocluster source system will be described. In parallel with my research activity, I have been profoundly involved in the commissioning of such a machine that is currently capable of producing size selected nanoclusters. Metallic nanocluster physics is a subject that is also receiving close attention from the scientific community since, when reduced to few tens of Å in size, the electronic and geometrical properties of matter dramatically depend on the precise number of atoms the objects are made of. The best example in this respect is given by Au nanoclusters which are, by far, the most investigated in the cluster family [11–13]. A precise control over the number of atoms is therefore needed in order to properly characterize the cluster properties using experimental techniques that provide space-integrated information. On the other hand, epitaxial graphene represents the ideal substrate for cluster growth and characterization due to its chemical inertness and, is some case, of the moiré corrugation, which is known to be useful as a template for patterned growth [14].

References

[1] Clauss, A.; Fischer, G.; Hofmann, U. Dünnste kohlenstoff-folien. *Zeitschrift Für Naturforschung B* **1962**, *17*, 150.

[2] Landau, L. D. On the theory of phase transitions. I. *Journal of Experimental and Theoretical Physics* **1937**, *11*, 19.

[3] Mermin, N. D. Crystalline Order in Two Dimensions. *Physical Review* **1968**, *176*, 250.

[4] Lee, C.; Wei, X.; Kysar, J. W.; Hone, J. Measurement of the Elastic Properties and Intrinsic Strength of Monolayer Graphene. *Science* **2008**, *321*, 385.

[5] Yoon, D.; Son, Y.-W.; Cheong, H. Negative Thermal Expansion Coefficient of Graphene Measured by Raman Spectroscopy. *Nano Letters* **2011**, *11*, 3227.

[6] Allen, M. J.; Tung, V. C.; Kaner, R. B. Honeycomb Carbon: A Review of Graphene. *Chemical Reviews* **2010**, *110*, 132.

[7] Novoselov, K. S.; Fal'ko, V. I.; Colombo, L.; Gellert, P. R.; Schwab, M. G.; Kim, K. A roadmap for graphene. *Nature* **2012**, *490*, 192.

[8] Wallace, P. R. The Band Theory of Graphite. *Physical Review* **1947**, *71*, 622.

[9] Varykhalov, A.; Sánchez-Barriga, J.; Shikin, A. M.; Biswas, C.; Vescovo, E.; Rybkin, A.; Marchenko, D.; Rader, O. Electronic and Magnetic Properties of Quasifreestanding Graphene on Ni. *Physical Review Letters* **2008**, *101*, 157601.

[10] Hwang, E. H.; Das Sarma, S. Acoustic phonon scattering limited carrier mobility in two-dimensional extrinsic graphene. *Physical Review B* **2008**, *77*, 115449.

[11] Haruta, M. Size- and support-dependency in the catalysis of gold. *Catalysis Today* **1997**, *36*, 153.

[12] Sanchez, A.; Abbet, S.; Heiz, U.; Schneider, W.-D.; Häkkinen, H.; Barnett, R. N.; Landman, U. When Gold Is Not Noble: Nanoscale Gold Catalysts. *The Journal of Physical Chemistry A* **1999**, *103*, 9573.

[13] Li, Z. Y.; Young, N. P.; Di Vece, M.; Palomba, S.; Palmer, R. E.; Bleloch, A. L.; Curley, B. C.; Johnston, R. L.; Jiang, J.; Yuan, J. Three-dimensional atomic-scale structure of size-selected gold nanoclusters. *Nature* **2008**, *451*, 46.

[14] N'Diaye, A. T.; Gerber, T.; Busse, C.; Mysliveček, J.; Coraux, J.; Michely, T. A versatile fabrication method for cluster superlattices. *New Journal of Physics* **2009**, *11*, 103045.

Chapter 2

Experimental Section

The experimental side of surface science is riddled with technical difficulties, but since its birth in 1926 with Davisson and Germer's experiments [1], major improvements in materials, pumping systems, and instrumentation have given scientists unprecedented access to this incredibly rich world.

Ultra high vacuum (UHV) conditions are normally required for surface science experiments, with pressures lower than 10^{-9} mbar ordinarily being employed. In this pressure regime, it is possible to prepare and maintain atomically clean surfaces and avoid contamination during the data acquisition. Moreover, these conditions are also required when using low energy electrons, or ions as probes, in order to avoid scattering from residual gas molecules in the vacuum chamber. The contamination of a surface can be qualitatively estimated by considering the impinging rate and sticking coefficient of residual molecules in gas phase. According to the Hertz-Knudsen formula, this is given by:

$$\Phi = \frac{P}{\sqrt{2mk_BT}} \tag{2.1}$$

where P is the pressure, m is the molecular mass of the gas, T is the temperature and k_B is the Boltzmann constant. Assuming the sticking probability (the probability an impinging molecule has of being adsorbed) is 1 (often not too far from the real value for many molecules on clean single crystal surfaces) and a background pressure of 10^{-6} mbar, a sample with typical surface atomic density would get covered by a complete layer of contaminants in about one second. Therefore, in order to be able to perform measurements on a clean surface for a useful amount of time, the background pressure is normally kept in the 10^{-10} mbar range (or better). A stainless steel vacuum chamber and an efficient pumping system is generally used to achieve this pressure, and a bake-out procedure has to be carried out to induce water desorption from the inner walls of the chamber, which would otherwise be the main contribution to the residual pressure.

Mean free paths (λ) for electrons or ions in the vacuum chamber of several centimeters are, as already stated, necessary for most probing techniques. This quantity λ depends on residual pressure by

$$\lambda = \frac{k_B T}{\sqrt{2} P \sigma}, \tag{2.2}$$

which gives, already for pressures in the 10^{-6} mbar range, a λ of hundreds of meters (σ being the effective cross section in the classical theory for scattering of rigid molecule), setting a much looser constraint on the pressure at around 10^{-4} mbar.

Besides UHV conditions, in-vacuum surface cleaning techniques are essential to prepare samples for experiments, as surfaces which contain no more than a few percent (and preferably much less) of contaminant species are needed. The noble gas ions bombardment is by far the most widely used method to achieve this in situ cleaning. However, one disadvantage of ion bombardment is that the surface is left in a heavily damaged state, so that the surface must be annealed to restore the long range order of the surface and to promote the formation of large terraces.

Furthermore, to remove carbon contamination from Pt-group and other transition metal surfaces, oxidation and reduction cycles are commonly employed. These are performed by heating the sample in an O_2 atmosphere with a pressure of the order 10^{-8} to 10^{-7} mbar. Then, to remove the adsorbed oxygen, the same procedure is commonly performed in a H_2 atmosphere in a similar range of pressures. For these procedures, and for many other purposes, a gas line equipped with several leak valves and gas bottles is commonly attached to UHV chambers, and allows for such controlled gas leaks.

The measurements which will be presented and discussed in this thesis work were performed mostly at the SuperESCA beamline and at the Surface Science Laboratory at the Elettra synchrotron in Trieste, although some parts were also performed at the Nanospectroscopy and BaDElPh beamlines of Elettra. In the next sections both the experimental techniques and setups used will be discussed in some detail.

2.1 The SuperESCA beamline

Elettra is a third generation synchrotron radiation facility located in Basovizza (Trieste), optimized for the VUV and soft X-ray range. Synchrotron radiation is generated by relativistic electrons when they are accelerated radially, thus emitting a highly collimated photon beam in the tangential direction. The electron bunches are generated in a short LINAC (Linear Accelerator) and injected in a booster ring, from which they are eventually transported to the storage ring at full energy. The storage ring is thus operated in top-up mode, and is made up of different types of magnets (bending magnets, quadrupoles, sextupoles and steering magnets) and includes some straight sections which

usually host insertion devices. These are the primary sources of high brightness X-ray beams. An example of insertion device is an undulator, which consists of two periodic arrays of magnetic poles that force the incoming electrons to follow a wiggling trajectory in such a way to irradiate.

Synchrotron radiation is much preferable to a conventional X-ray source, since it is tunable and has a wide range of photon energies which are accessible by properly adjusting the undulator gap and the monochromator. Moreover, synchrotron radiation yields much higher brilliance (a high photon flux within a narrow energy bandwidth and with a small angular divergence) and a high degree of polarization. The insertion device used at the SuperESCA beamline [2] is a high brilliance 46 mm period undulator made of two modules with 98 periods, that produces photons in the energy range 90-1500 eV. The radiation generated by the undulator is pre-focused into the monochromator (a plane grating Zeiss SX700) [3], and then re-focused on the sample by an ellipsoidal mirror. The resolving power ($E/\Delta E$) of the monochromator is of the order of 10^4 for $h\nu < 500$ eV. The experimental workstation consists of two UHV chambers separated by a valve. The upper stainless steel chamber is used for sample cleaning and preparation, while the second, lower chamber, is made of μ-metal (the typical material of choice to screen the sample from stray magnetic fields due to its high magnetic permeability) and is devoted to the experimental measurements. A technical drawing of the experimental setup is shown in Fig. 2.1.

The manipulator used for our experiments at SuperESCA has four degrees of freedom (corresponding to the x, y, and z axes and to the polar angle θ) and allows cooling the sample down to 25 K and heating it either by filament radiation or by electron bombardment. The chamber is further equipped with a quadrupole mass spectrometer and, of course, the electron energy analyzer. The latter is a hemispherical PHOIBOS electron energy analyzer from SPECS GmbH, with a mean radius of 150 mm, equipped with a locally made delay-line detector. The electron energy analyzer is composed of two hemispherical electrodes (of radius R_1 and R_2, respectively) kept at proper voltages (see Fig. 2.2). It can be demonstrated that, if electrons enter the analyzer at a radius R_0, they are refocused after traveling 180° if they have energy $E_0 = eV_0$, which depends on the potential difference between the hemispherical electrodes and the radii of the electrodes by

$$V_2 - V_1 = 2V_0 R_0 \frac{R_1 - R_2}{R_1 R_2} \tag{2.3}$$

In fact, electrons impinging normal to the entrance slit of the analyzer with energy E_0 follow a trajectory of radius $R_0 = (R_1 + R_2)/2$, which allows them to reach the exit slit and thus to be revealed by the detector, while electrons entering with a different angle follow different paths, being refocused nonetheless at the opposite end of the analyzer if their energy is E_0. Electrons with less energy fall short, while more energetic electrons will have a larger trajectory radius. It is therefore possible to determine a dispersing (radial) and a non-

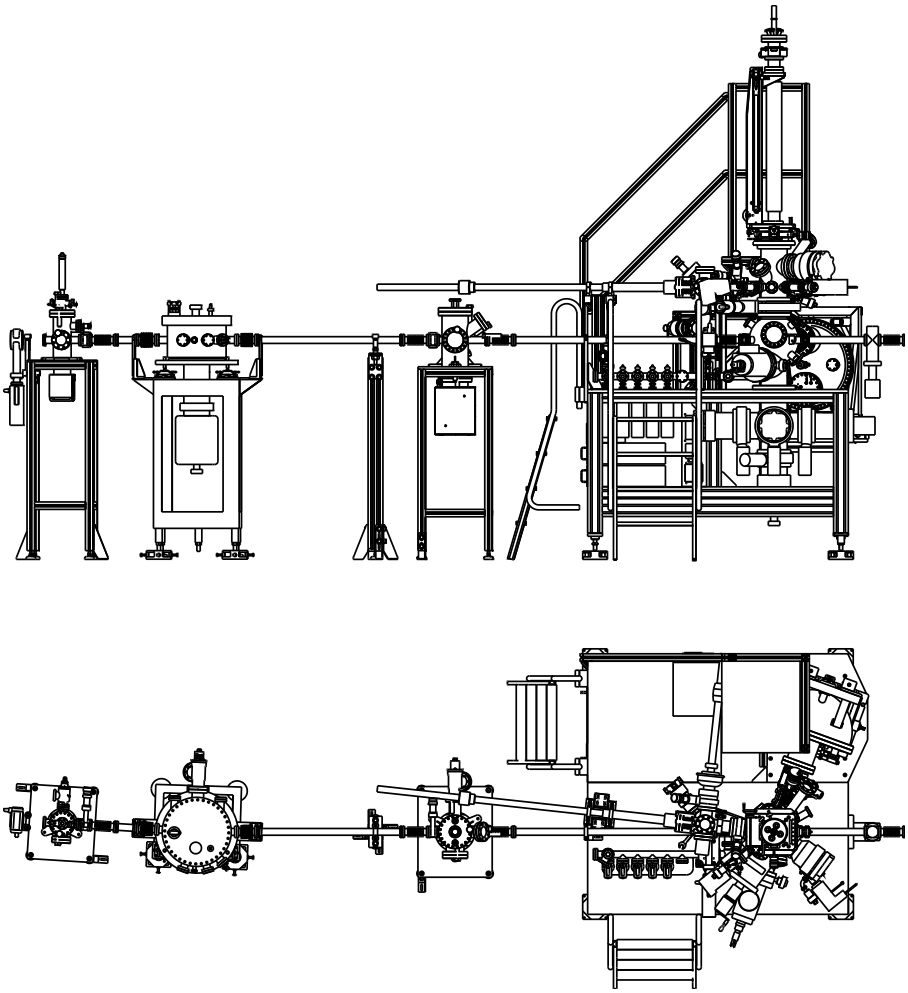

Figure 2.1: Technical drawing of the SuperESCA end-station at Elettra. The synchrotron radiation beam enters the experimental chamber on the right side, where the electron energy analyzer is also visible (hemispherical structure). Recognizable elements include the two-chamber structure, with the preparation chamber above the experimental chamber, the manipulator, and the gas line.

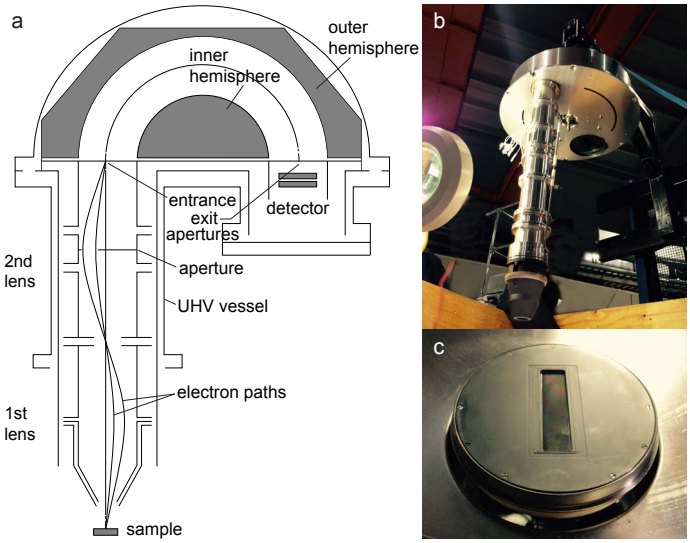

Figure 2.2: (a) Schematic illustration of a hemispherical analyzer. (b) Photograph of the partially disassembled electron energy analyzer from SuperESCA with lenses visible. (c) The top side of the detector, with the micro channel plate (MCP) visible. Small wires spotwelded lengthwise 500 µm apart are used to correct the electric field close to the MCP.

dispersing (tangential) direction at the analyzer exit, and if space-resolved detectors are employed, it is possible to measure a complete spectrum in a single shot.

The instrumental energy resolution of the device depends both on the geometrical parameters of the analyzer and on the angular divergence of the electron beam:

$$\Delta E = E_0 \left(\frac{w}{2R_0} + \frac{\alpha^2}{4} \right) \tag{2.4}$$

where w is the average width of the entrance and exit slits, and α is the incidence angle of the photoelectrons with respect to the normal of the entrance slit. The choice of the pass energy E_0 directly affects the spectral resolution. In fact, a low pass energy improves the resolution, but the electron transmission probability is damped, so that a compromise is actually required between a high energy resolution and a good signal-to-noise ratio. Though the resolution also improves with increasing R_0, technical problems related to the dimensions of the analyzer set an upper bound to the values of R_0 which are actually attainable. The electrostatic lenses in front of the analyzer perform a double task: they collect the incoming photoelectrons from a large solid angle and focus them into the entrance slit of the analyzer, and at the same time, they slow down the electrons to the required kinetic energy E_0. The electrons that reach the exit slit are collected by a microchannel plate coupled to the detector.

When acquiring spectra in sweep (or scanning) mode, the voltages of the two hemispheres V_1 and V_2 (and hence the pass energy) are held fixed while the voltage applied to the electrostatic lenses is swept in such a way that each channel of the detector counts electrons with the selected kinetic energy for an interval equal to a given time window. In order to drastically reduce the acquisition time per spectrum, the snapshot (or fixed) mode can be used. This method exploits the relation between the kinetic energy of a photoelectron and its position inside the detector. If the energy range covered by the detector is wide enough, and if the photoemission signal collected by a large number of channels is sufficiently strong, it is possible to acquire a detector image, thus obtaining a photoemission spectrum in one single shot. This allows to drastically decrease the spectrum acquisition time as little as 400 ms [4] if necessary.

2.2 High Resolution Core Level Photoelectron Spectroscopy

The photoemission process from a solid sample takes place when a photon with enough energy interacts with matter, causing an electron to be removed from an atomic orbital, or from an electronic band, and to reach the vacuum level with positive kinetic energy [5]. This experimental technique has been developed in an analytical tool by K. Siegbahn, 1981 Physics Nobel Prize winner for Electron Spectroscopy for Chemical Analysis (ESCA) [6]. The process has been traditionally described according to a three step model, involving first the optical excitation of the electron (Fig. 2.3), which, in a second step, propagates to the surface, and finally escapes into the vacuum. The N-electron system is thus left in a core-ionized state. Photoemission can take place either from the valence band or from the core levels (Fig. 2.3), which generally show negligible dispersion due to their highly localized atomic-like character. Soft X-rays (the kind of radiation used at the SuperESCA beamline) are especially suitable to probe the core levels of a solid. When a photoemission event takes place, the following energy conservation law applies:

$$h\nu = |E_b^v| + E_k \tag{2.5}$$

where $h\nu$ is the photon energy, $|E_b^v|$ is the electron binding energy prior to ionization, as calculated with respect to the vacuum level, and E_k is the kinetic energy of the photoelectron. If the reference is taken with respect to the Fermi level (as is conventionally done in photoelectron spectroscopy) $|E_b^v|$ can be replaced by the sum of the BE relative to the Fermi level, $|E_b^F|$, and the sample work function, Φ_0 (Fig. 2.4). When the electrons reach the analyzer, their kinetic energy is altered by the difference in work function between the analyzer and the sample. This is true if the analyzer and the sample are kept in electrical contact, so that their Fermi levels align, and an electric potential

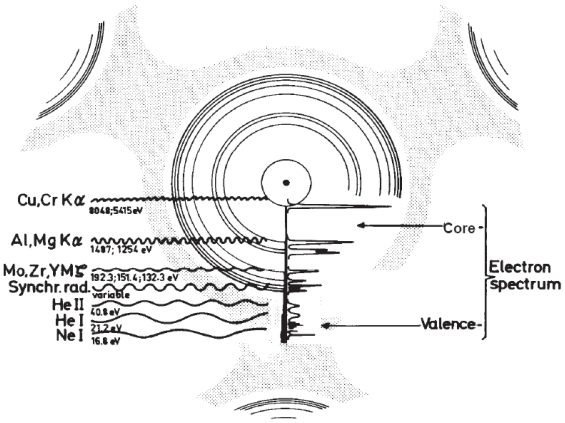

Figure 2.3: Schematic picture from K. Siegbahn's Nobel lecture [6] representing how different X-ray sources can interact with different electrons in a solid.

difference will be present between the sample's and the analyzer's vacuum levels. The kinetic energy of the electrons inside the analyzer can be written as $E_{k,a} = E_k + (\Phi_0 - \Phi_a)$, giving an expression for the photoelectron binding energy:

$$E_b^F = h\nu - E_{k,a} - \Phi_a \tag{2.6}$$

In principle, it is therefore enough to know the photon energy, the analyzer's work function, and to measure the kinetic energy to know the binding energy of a photoelectron. In practice, the small errors encountered in this procedure render this approach useless when measuring tiny binding energy shifts in core levels. It is therefore necessary, if very high accuracy is needed, to also acquire a spectrum of the Fermi level for each core level spectrum, so that a direct calibration can effectively be carried out for each measurement. When measuring both the core level and the Fermi level spectrum, it is straightforward to find the binding energy of the photoelectrons that give origin to a photoemission peak.

One of the fundamental properties of X-ray photoelectron spectroscopy is its chemical sensitivity. First of all, the photoelectron binding energies are a clear fingerprint of the elements present in the sample. Moreover, the chemical environment (the type of bonding, the presence of adsorbates or the oxidation state etc.) experienced by the electron prior to the photoemission event affects its BE resulting in a characteristic chemical shift that can be accurately predicted by Density Functional Theory (DFT) calculations. Therefore core level spectra convey a significant amount of information about the nature of the system under study especially when backed by numerical calculations.

Another remarkable property of photoelectron spectroscopy is its innate surface sensitivity. This is better understood by considering the universal curve of the electron inelastic mean free path, reported in Fig. 2.6. As can be seen

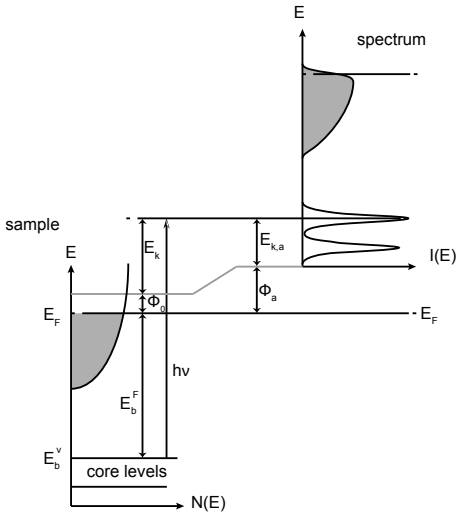

Figure 2.4: Energy diagram for the photoemission process. The emitted electrons show a widening of what would otherwise be delta peak functions due to limited lifetime effects and other contributions discussed in the text.

from the graph, by tuning the photon energy it is possible to maximize the surface sensitivity by selecting emitted electron kinetic energies between 50 and 100 eV, in the minimum of the universal curve, ensuring mean free paths limited to a few Å. This means that detected photoelectrons in that energy range mostly originate from the first few layers of the solid, hence giving photoelectron spectroscopy its usefulness as a primary tool for investigating the electronic structure of thin films and solid surfaces and interfaces.

From the theoretical point of view, the photoemission process is generally described in a semiclassical approach, where the electromagnetic field is still treated classically, while the solid is described in quantum mechanical terms. The one-particle Hamiltonian for an electron subjected to an electromagnetic field is given by:

$$i\hbar\frac{\partial\psi}{\partial t} = \left[\frac{1}{2m}\left(\hat{\mathbf{p}} - \frac{e}{c}\hat{\mathbf{A}}\right)^2 + \hat{V}\right] = \hat{H}\psi \tag{2.7}$$

where ψ is the electron wave function, $\hat{\mathbf{A}}$ is the vector potential of the electromagnetic field and $\hat{V}$ is the unperturbed potential of the solid. In the Coulomb gauge $\nabla \cdot \hat{\mathbf{A}} = 0$, and the vector potential commutes with the momentum operator ($[\hat{\mathbf{p}}, \hat{\mathbf{A}}] = 0$), so that the expression in brackets simplifies to:

$$\left(\hat{\mathbf{p}} - \frac{e}{c}\hat{\mathbf{A}}\right)^2 = \hat{p}^2 - 2\frac{e}{c}\hat{\mathbf{A}}\cdot\hat{\mathbf{p}} + \left(\frac{e}{c}\right)^2\hat{A}^2 \tag{2.8}$$

The quadratic term in $\hat{A}$ can be neglected, since its contribution under normal experimental conditions is typically one order of magnitude smaller than

the first term. Following a first-order perturbation approach, the one-electron Hamiltonian can be split into two terms, an unperturbed Hamiltonian $\hat{H}_0$, plus an interaction Hamiltonian $\hat{H}'$, which accounts for the effects of the electromagnetic field:

$$\hat{H}' = -\frac{e}{mc}\hat{\mathbf{A}} \cdot \hat{\mathbf{p}} \tag{2.9}$$

Time-dependent perturbation theory applied to harmonic perturbations allows us to express the transition rate between the initial state ψ_i and the final state ψ_f by the Fermi Golden rule:

$$W_{i\to f} \propto \frac{2\pi}{\hbar}|\langle\psi_f|\hat{H}'|\psi_i\rangle|^2 \; \delta(E_f - E_i - h\nu) \tag{2.10}$$

where E_i and E_f are the eigenvalues of the unperturbed Hamiltonian in the initial and final state, respectively, and $h\nu$ is the photon energy.

2.3 The Surface Science Laboratory

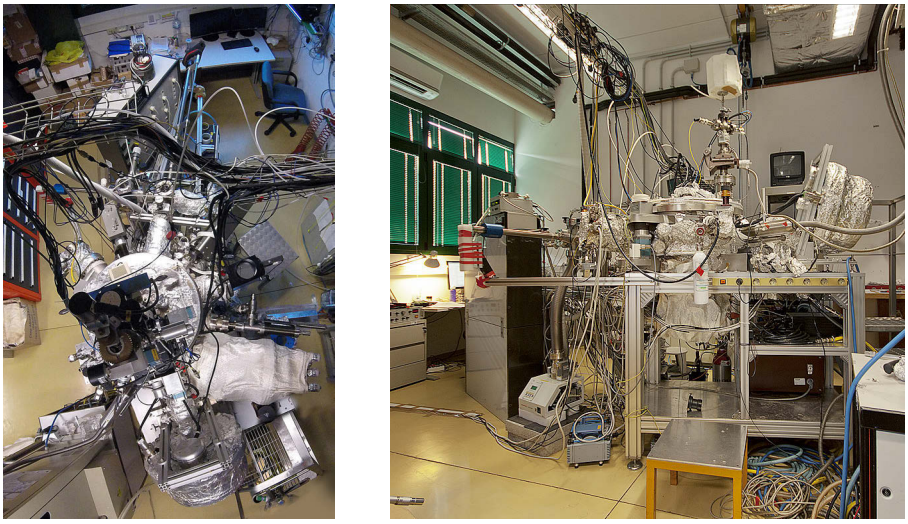

Figure 2.5: The experimental chamber of the Surface Science Laboratory. Seen from above in the left image, counterclockwise from the left, the sputter gun, the Mg-Kα X-ray source, the electron energy analyzer, the Fisons LEED with image acquisition hardware, and the Omicron SPA-LEED. On the right, seen from the side, the X-ray source and the electron energy analyzer are visible in the right portion of the image.

The experimental chamber of the Surface Science Laboratory is primarily devoted to LEED/SPA-LEED and conventional XPS (X-ray Photoelectron Spectroscopy)/XPD(X-ray Photoelectron Diffraction) measurements. It

is equipped with two X-ray sources, an Al-Kα and a Mg-Kα (which generate X-ray radiation at $h\nu = 1486.6$ eV and 1253.6 eV, respectively), and with a hemispherical electron energy analyzer (with mean radius of 150 mm) which collects the photoelectrons emitted from the sample in XPS and XPD experiments. In addition, a quadrupole mass spectrometer residual gas analyzer (RGA) allows Temperature Programmed Desorption (TPD) (also known as Thermal Desorption Spectroscopy) experiments to be performed. The chamber has a highly flexible configuration, owing to the presence of a remote controlled rotating flange, which allows sample movement and alignment in front of the instruments which are mounted on the different flanges of the chamber (LEED, SPA-LEED optics, sputter-ion gun, X-ray sources, RGA). Fig. 2.5 shows a top and a side view of the chamber.

The specimen can be heated either by direct radiation from the tungsten filaments behind or by electron bombardment. In this case a bias is applied between the filaments and the sample in such a way to accelerate the thermionically emitted electrons from the filaments towards the sample. This mounting allows to heat the sample to high temperatures (in our case, up to 1400 K) while keeping a very good background pressure.

A gas line allows for oxidation/reduction cycles to be performed, and reaction gases to be dosed in the UHV chamber in a controlled manner. For oxidation and intercalation experiments at high pressures, an oxygen doser allows for pressures of the order of 1×10^{-3} mbar to be applied in the proximity of the sample while keeping pressures in the rest of the UHV chamber at a level turbomolecular pumps can tolerate.

2.4 Low Energy Electron Diffraction

Low Energy Electron Diffraction (LEED) is an experimental technique used to investigate the surface structure of materials with long-range order. Its serendipitous discovery by Davisson and Germer dating 1927 [1] was not reproduced for many years due to inadequate vacuum techniques and slow detection methods. Eventually, in the 1960s, this powerful technique has been reconsidered and is, even today, one of the most commonly employed tools for the investigation of ordered surfaces owing to its wide range of applicability, its relatively low cost and because it requires only a UHV chamber and the device itself to be used. The high degree of interaction that slow electrons have with matter makes the data obtained with this probe often very difficult to completely explain from simple models, nonetheless potentially bearing incredibly exhaustive descriptions of the analyzed systems.

The investigation of diffraction patterns through low energy electrons (20-400 eV) allows, by analyzing the direction and intensity in which these are scattered, the investigation of long-range order in the surface. In addition, with an approach based on the dynamic theory, it is possible to reconstruct the

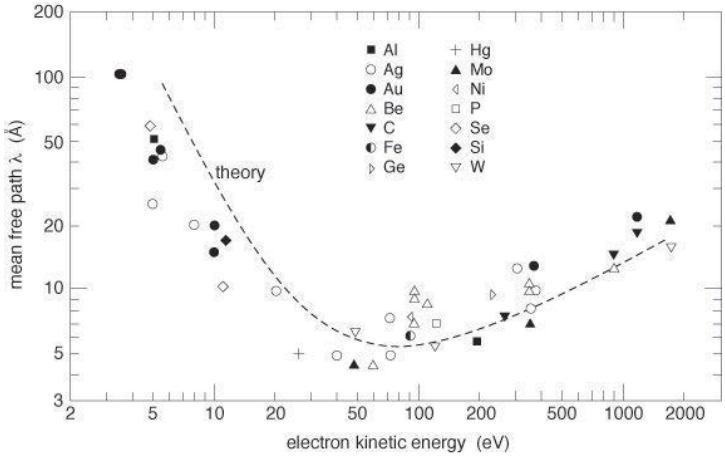

Figure 2.6: Universal curve of the electron inelastic mean free path (MFP). The minimum in MFP is in the range 50-500 eV, and is where maximum surface sensitivity can be achieved.

precise geometric structure of the studied surface, and to obtain information on the bond lengths and the expansion or relaxation effects on the surface. The surface sensitivity is guaranteed by the mean free path of the electrons within the solid being analyzed, which is less than 10 Å in the considered energy range (Fig. 2.6). In the single scattering approximation (kinematic theory), the electron is represented by a plane wave which, interacting with the surface, can be diffracted along preferential directions that satisfy the Laue condition:

$$\boldsymbol{k}_{in} - \boldsymbol{k}_{out} = \Delta \boldsymbol{K} \in G \tag{2.11}$$

where $\boldsymbol{k}_{in}$ and $\boldsymbol{k}_{out}$ are the incoming and outgoing wave vectors, $\Delta \boldsymbol{K}$ is the scattering vector, and G is the reciprocal lattice. This condition can be interpreted through the geometric construction of the Ewald sphere (Fig. 2.7). For a 2D surface in 3D space, reciprocal lattice points are distributed along rods perpendicular to the crystal surface in correspondence to the points of the 2D reciprocal lattice. The points of intersection between these lines and the Ewald sphere, the radius of which depends on the modulus of the k-vector of the incident electrons, determine the direction of the scattered electrons.

A typical LEED apparatus is presented schematically in Fig. 2.8. A heated filament emits electrons, which are collimated by a system of lenses and then accelerated to the desired energy towards a drift tube. Once the collimated monochromatic beam reaches the sample, the electrons are backscattered from the surface and then collected. A first grid, which is grounded to the same reference as the sample, is placed to screen electrostatic potentials and allows the electrons to propagate into a field-free region, preserving angles and trajectories of the backscattered electrons. A second grid is placed at a potential only slightly

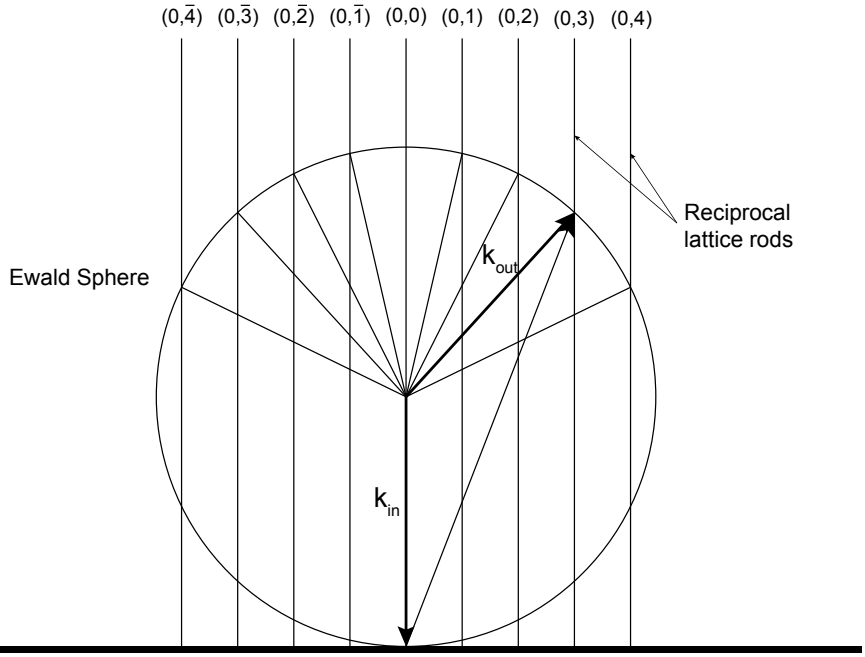

Figure 2.7: A slice of the Ewald construction for 2D surfaces in 3D space. The reciprocal lattice points are distributed along rods perpendicular to the ordered surface. In the LEED geometry, $\boldsymbol{k}_{in}$ is held fixed, while multiple $\boldsymbol{k}_{out}$ are detected at once. Only the ones crossing reciprocal lattice rods give rise to diffraction maxima.

lower from that of the electron gun filament to reject electrons resulting from inelastic scattering events. Elastically scattered electrons, after passing a second grounded grid, are instead allowed to accelerate to a fluorescent screen by a positive potential of a few kilovolts, creating a visible diffraction pattern which is then recorded by a CCD camera placed on the air side of a window.

The resolution in k-space of a LEED system is directly linked to the size in real space of the electron beam when it reaches the phosphor screen, which is therefore the determining factor for the transfer width (TW) of the instrument. The TW is the largest average domain size the particular LEED system can detect on a surface at a given energy. Normally, larger average domain sizes give sharper diffraction spots, according to $FWHM = 2\pi/D$, so that the full width half maximum of the diffraction peak (FWHM) is inversely proportional to the average domain size D. But this is only true until the instrumental resolution is reached, therefore giving a lower limit on the spot size, and an upper limit to the detected average domain size that can be detected. The two main contributions to the TW are the electron beam angular divergence and its energy spread. Normally, in LEED experiments the TW is of the order of 100 Å.

Both the SuperESCA and the Surface Science Laboratory are equipped with a LEED apparatus.

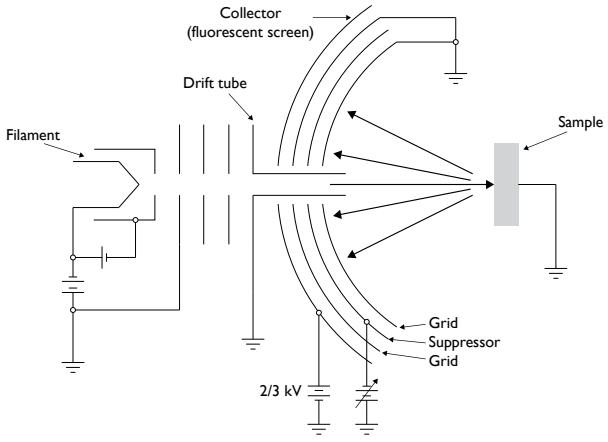

Figure 2.8: Typical LEED apparatus schematic. A hot filament produces electrons by thermionic emission. These are accelerated and focused by a set of electrostatic lenses and sent on the sample surface. After surface interaction, a series of grids suppresses ineastically scattered electrons and accelerates the residual ones towards a phosphor screen.

2.5 Spot Profile Analysis - Low Energy Electron Diffraction

Spot Profile Analysis - LEED (SPA-LEED) is, like LEED, a technique that allows diffraction patterns generated by low energy electrons impinging on long range ordered surfaces to be measured. However, a number of modifications allow for technical advantages which render it a very useful complement to conventional LEED. The most prominent difference with respect to LEED is in the way the image is generated: the diffraction pattern is effectively scanned in a way equivalent to changing the azimuthal and polar angles of the sample, but by using a set of electrostatic deflection plates instead so that no mechanical movement is necessary. The image is scanned over a detector that is not the usual phosphor screen, but is a channeltron with a small (100 µm) aperture in front of it. This and several other differences give the SPA-LEED a transfer width of about 1000 Å, a dynamic range of 10^6 with a linear response (as opposed to dynamic ranges of 10^3 and nonlinear response of phosphor screen/CCD camera systems), and the possibility of observing the (0,0) spot at normal geometry, which is normally covered by the electron gun in conventional LEED systems. On the other hand, acquisition times are one order of magnitude slower, rendering it, for many aspects, a complementary technique to LEED.

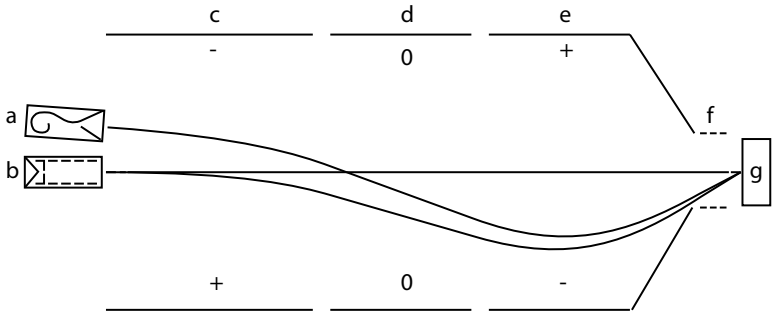

Figure 2.9: Schematic side view of a SPA-LEED system. (a) Channeltron detector, (b) electron gun, (c) first section, (d) second, grounded section, (e) third section, (f) entrance lens, (g) sample. In the image, a particular deflection condition has been frozen in time so that the plates in the first section have an electric field pointing up, while the plates in the third section have an electric field pointing down. The complete system has 8 plates around the central axis (dashed line) that display variable electric fields as the reciprocal space is scanned.

The machine consists of an electron gun, three sets of eight electrostatic deflection plates, an entrance lens, and a detector (see Fig. 2.9). The deflection plates are arranged and operated so that, to a very good approximation, it is possible to scan the angle of incoming and outgoing electrons from the sample, while keeping the location where they impinge on the sample and the angle between them fixed. This is accomplished by creating electrostatic

potentials that cause an S-shaped trajectory in the electron beams. To better understand the mechanism, it is useful to consider the 2D case, schematized in Fig. 2.9. Neglecting edge effects, if the deflection plates have electrical potentials applied as in the figure, electrons emitted from the electron gun will move in three separate constant electrical potential zones (with the second one always grounded), and will have parabolic trajectories in regions where an electric field is present, linear ones where the field is null. The three sections are arranged as follows: in the first, a uniform electric field is present. This causes a deviation in the electron paths in a direction opposite to the electric field. In the second section, a zone with no field is encountered, so that edge effects are minimized. In the third section, an electric field proportional to the first but opposite in direction brings the electron beam back towards the central axis of the system. If the proportionality constant between potentials in the first and third section is kept fixed, the position where the central axis is crossed is independent of the choice of voltage on the plates, and corresponds to the optimal position for sample placement. The specific S-shaped trajectory followed will obviously depend on the choice of voltage on the plates.

For backscattered electrons the process is quite similar: only the ones that follow a specific trajectory will reach the point detector. This trajectory is such that, for small distances of the detector from the electron source, the angle between the electrons that reach the detector and the ones coming from the source is almost constant, independent of deflection voltages. Thus, in the 2D case, just one parameter, the voltage of the first set of deflector plates, univocally determines the incoming and outgoing k vectors for electrons on the crystal surface. To deflect electron beams in a similar way but in 3D, it would be necessary to generate electric fields at arbitrary angles around the longitudinal axis of the instrument. This can be achieved by having multiple plates for each of the three sections around the longitudinal axis, and defining appropriate voltages on each deflecting plate. In commercial SPA-LEED systems there are eight such plates for each section, giving the possibility of defining a uniform electric field with an arbitrary direction in each of the two active sections with only small distortions. To set the voltages appropriately on all the deflection plates, only two potentials (for two orthogonal directions) are actually needed: dividing resistors can take care both of the proportionality between the first section's voltage and the third's, and the distribution of the voltages on the eight plates of each active section. Therefore, in 3D, to any set of two voltages, if the beam energy is fixed, one can univocally associate a specific wavevector $\boldsymbol{k}_{in}$ to electrons impinging on the sample and a specific $\boldsymbol{k}_{out}$ to electrons reaching the detector. If one records the intensity of the electron beam reaching the detector for every set of deflecting voltages, it becomes possible to generate images that map the reciprocal space.

This setup gives specific conditions for diffraction maxima of detected electrons, which are different from the LEED case. Now, $\boldsymbol{k}_{in}$ can have any angle, but $\boldsymbol{k}_{out}$ is fixed at a definite angle with respect to $\boldsymbol{k}_{in}$. When the Laue condition is met for a specific $\boldsymbol{k}_{in}$ and $\boldsymbol{k}_{out}$, the detector will register an intensity

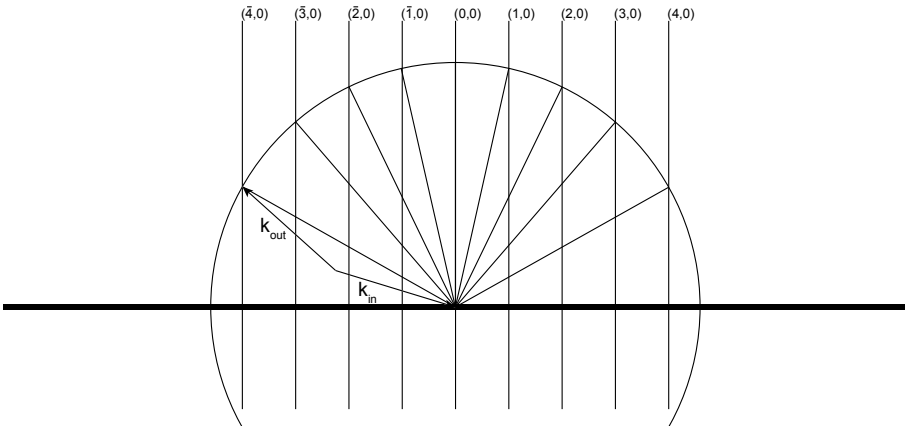

Figure 2.10: The modified Ewald construction for the SPA-LEED. In this case, the angle between $\boldsymbol{k}_{in}$ and $\boldsymbol{k}_{out}$ is kept fixed. When the vector difference (thin lines radially placed in the sphere) touches a reciprocal lattice rod, the diffraction condition is met and, for such a deflection, a diffraction peak will be observed.

peak. To better visualize this, it is possible to build a modified Ewald construction (Fig. 2.10). This is quite similar to the LEED case, but for any given wavenumber, the radius of the modified Ewald sphere will be almost double because of the small angle between $\boldsymbol{k}_{in}$ and $\boldsymbol{k}_{out}$: this allows diffraction images or profiles to map the reciprocal space at almost fixed $\boldsymbol{k}_{\perp}$.

The large transfer width of the instrument is given mainly by two factors. One is the entrance lens, which is an Einzel lens that allows to focus on the detector the image of the virtual source, so the normal divergence of an electron gun can be corrected. In fact, the lens is such that the electrons impinging on the sample are parallelized, and the image generated by the returning electrons can be as small as the size of the virtual source. Furthermore, since the electron source is a LaB_6 crystal, the energy spread of the electron beam is usually around 0.4 eV [7]. This material's thermionic emission has exceptional qualities, which exceed those of tungsten and even thoriated tungsten filaments. The work function is much lower compared to W (2.7 eV for LaB_6, 4.5 eV for W [8]), and although the work function is similar to Th−W, the brightness is 9.7 times higher for LaB_6. This small energy spread allows for a further increase in TW that, having been improved both in energy spread contribution and angular spread contribution, is 1 order of magnitude better than for LEED.

2.6 Data Analysis

2.6.1 Low energy electron diffraction data analysis

Low energy electron diffraction data can be used as a probe for long-range order in surfaces, and is an essential tool for interpreting XPS spectra. These diffraction images can give a wealth of data on the surfaces being investigated, but even a very simple analysis can yield important information. The data extracted from LEED images in this work was mostly derived from spot position or spot shape.

In order to find spot positions for sharp spots, it is often sufficient to find the best-fitting 2D Gaussian to a given set of pixel values in an appropriate range around any particular diffraction spot, even though the spot's intensity distribution is not Gaussian. A standard χ^2 minimization algorithm can be used. The function used for fitting is given by the sum of a 2 dimensional Gaussian and a plane, used to give a first order approximation to the background. The intensity of the spot is taken to be proportional to the integral of the Gaussian.

The Gaussian fitting is not ideal for LEED spots in general, as these do not usually have a pure Gaussian shape. Nevertheless, a Gaussian approximation to peaked functions can be used, as is supported by the small, mostly modulation-free residues obtained in most cases.

On the other hand, to extract data from the spot shape, it is usually much preferable to analyze line profiles going through the peaks at different, high symmetry directions. This is because diffraction peaks can often be fitted by a Voigt function, the Gaussian width being related to the experimental contribution to the spot shape (and therefore to the transfer width), the Lorentzian to the average size of the ordered domains.

More data can be, in principle, extracted from the spot shape, but technical limitations in the device render such refined analysis fruitless, mostly because of the relatively small transfer width. Many more details can be understood by using the SPA-LEED instrument, that has unmatched capabilities in acquiring data for determining the details of spot profile shapes.

Dewarping

LEED and SPA-LEED images must also be corrected prior to analysis, if large portions of the image are relevant (as in finding spot distances, or analyzing particularly large spots), since distortions induced by the fact that a spherical screen is projected on a flat CCD sensor (even in the best case scenario of no lens distortions) for the LEED instrument or by inhomogeneities in the electric field in the case of the SPA-LEED can be corrected by using a calibrated grid and applying a dewarping procedure to each of the acquired images. This is necessary if relative distances between diffraction spots are of interest, and can reduce the systematic error to about 1% in relative distances. This is usually the dominant factor in distance evaluation, since 2D Gaussian fits in

a small interval about the diffraction spots give errors at least one order of magnitude better. The fitting algorithms can also give quantitative information on spot intensity as a function of any parameter, including electron energy (for LEED-IV curves) or annealing temperature.

2.6.2 X-ray Photoemission data analysis

Regarding XPS data, real measurements have a spectral line width that is broadened by core-hole lifetime (τ). Assuming an exponential decay, it is possible to show that the theoretical spectral line shape can be described by a Lorentzian distribution:

$$I(E) \propto \frac{\Gamma/2}{(E - E_B)^2 + (\Gamma/2)^2} \tag{2.12}$$

where Γ is the Lorentzian Full Width Half Maximum (FWHM) and is related to τ. The photoemission event leaves the atom in a highly excited core-hole ionized state, from which it can decay radiatively (by fluorescent emission) or non-radiatively (typically via an Auger process). Besides the aforementioned Lorentzian broadening, photoemission spectra are also affected by a Gaussian broadening, which contains three main contributions, namely the experimental energy resolution, the inelastic scattering caused by exciting or absorbing phonons, and the inhomogeneous broadening. The first effect accounts for the non perfect monochromaticity of the photon beam, which results in a finite bandwidth, and by the limited resolving power of the electron energy analyzer. The vibrational broadening is produced by the excitation of low energy vibrational modes both in the initial and in the final state. Finally, an inhomogeneous contribution may originate from the presence of unresolved core level shifted components in the spectrum. The Gaussian contribution to the experimentally observed broadening can be expressed as:

$$I_G(E) = \frac{I_0}{\sigma\sqrt{2}} \exp\left(-\frac{(E - E_B)^2}{2\sigma^2}\right) \tag{2.13}$$

An accurate description of the line shape of photoemission peaks was formulated by Doniach and Šunjić [9], who elaborated a modified Lorentzian distribution function by including an asymmetry parameter α (also called Anderson singularity index) which accounts for the excitations of electrons from filled to empty states close to the Fermi level. The Donjach-Šunjić (D-S) line shape is expressed as:

$$I_{DS} = I_0 \frac{\Gamma_E(1 - \alpha)}{\left[(E - E_B)^2 - (\Gamma/2)^2\right]^{(1-\alpha)/2}} \, \xi(E) \tag{2.14}$$

where Γ_E is the Euler Gamma function (and is independent of the energy), and

$$\xi(E) = \cos\left[\frac{\pi\alpha}{2} + (1 - \alpha) \arctan\left(\frac{E - E_B}{\Gamma/2}\right)\right] \tag{2.15}$$

All the spectra presented in this thesis work were fitted using a D-S profile convoluted with a Gaussian distribution function to take into account all other possible spectral broadening effects previously described.

In some cases, it is necessary to include a Shirley background [10]. This is, like the D-S, a semi empirical function proportional to the peak integral, which effectively describes a step-like behavior in the background commonly observed on the two sides of photoemission peaks. In the original implementation, an iterative procedure was used to integrate only the signal originating from the peak, and not from the background itself. This procedure commonly converges within 10 iterations, but gives unsatisfactory results in the case a small interval around the core level peak is available in the data, as is often the case. A much more practical approach is to include such a background proportional to the D-S function integral in the fitting function, where no iteration is necessary, since the analytical D-S function is already known and does not need to be separated from the background contribution.

All core level spectra were collected along with their Fermi level and rescaled by the Fermi energy. This has been calculated by a fit with a Fermi-Dirac distribution function convoluted with a Gaussian of the spectrum generated by electrons excited from the Fermi level.

2.6.3 Analysis of the DFT Calculations Results

The DFT results presented throughout the thesis, performed in collaboration with two different groups, have been carried out using the CP2K code (calculations by Prof. Lev Kantorovich's group, illustrated in Ch. 3) or the VASP code (calculations by Prof. Dario Alfè's group, all other cases). The results of the numerical calculations have often been essential for the interpretation of the experimental results, and they have been exploited in many ways, most notably by using the calculated core electron binding energies to interpret experimental XPS spectra. In all cases, the starting point for all the numerical calculations presented in this thesis has been to find the relaxed structures, which are closely related to the expected geometry for the adsorbed graphene-like systems. The relaxed structures themselves can aid in determining what the shifts in core electron binding energy are due to, and they can also give important information on why the systems behave like they do, allowing a critical interpretation of the numerical results.

For this reason, in cases where the structural information was relevant, the atomic coordinates resulting from the relaxed structures were analyzed with the aim of finding two important parameters for adsorbed carbon atoms. First of all, the distance of each carbon atom from the surface can give quantitative information on the degree of interaction with the substrate, therefore helping to determine if a core electron binding energy shift is correlated to the atom-substrate distance. This parameter was determined by first calculating the average first substrate layer z coordinate (the DFT calculations are performed using a slab geometry). It is then straightforward to determine the distance of

an atom from the surface plane once its coordinates are known. The next index that was analyzed, in the case of graphene-like adsorbates, is the average C-C distance for each C atom. This parameter gives a good indication of the local strain, which is another structural parameter that can influence core electron binding energies. The average C-C distance is calculated by averaging all the nearest neighbor distances for every C atom, and is the result of an average of one to three values, depending on coordination. Finally, correlation diagrams are constructed by using the core electron binding energy and the two structural parameters as variables. These can in some cases give insight to the origin of the observed behaviors, and they can reveal any clustering that takes place in the parameter space, allowing the identification of different families of atoms.

References

[1] Davisson, C.; Germer, L. Diffraction of Electrons by a Crystal of Nickel. *Physical Review* **1927**, *30*, 705.

[2] Abrami, A.; Barnaba, M.; Battistello, L.; Bianco, A.; Brena, B.; Cautero, G.; Chen, Q.; Cocco, D.; Comelli, G.; Contrino, S.; DeBona, F.; Di Fonzo, S.; Fava, C.; Finetti, P.; Furlan, P.; Galimberti, A.; Gambitta, A.; Giuressi, D.; Godnig, R.; Jark, W.; Lizzit, S.; Mazzolini, F.; Melpignano, P.; Olivi, L.; Paolucci, G.; Pugliese, R.; Qian, S.; Rosei, R.; Sandrin, G.; Savoia, A.; Sergo, R.; Sostero, G.; Tommasini, R.; Tudor, M.; Vivoda, D.; Wei, F.; Zanini, F. Super ESCA: First beamline operating at ELETTRA. *Review of Scientific Instruments* **1995**, *66*, 1618.

[3] Jark, W. Soft x-ray monochromator configurations for the ELETTRA undulators: A stigmatic SX700. *Review of Scientific Instruments* **1992**, *63*, 1241.

[4] Lizzit, S.; Baraldi, A. High-resolution fast X-ray photoelectron spectroscopy study of ethylene interaction with Ir(1 1 1): From chemisorption to dissociation and graphene formation. *Catalysis Today* **2010**, *154*, 68.

[5] Einstein, A. Concerning an heuristic point of view toward the emission and transformation of light. *American Journal of Physics* **1965**, *33*, 367.

[6] Siegbahn, K. Electron spectroscopy for atoms, molecules, and condensed matter. *Science* **1982**, *217*.

[7] Wells, T.; El-Gomati, M. The energy spread of a LaB_6 cathode operated in the virtual source mode. *Journal of Physics: Conference Series* **2014**, *522*, 012054.

[8] Wolf, B. *Handbook of ion sources*; CRC press, 1995; pp 27.

[9] Doniach, S.; Šunjić, M. Many-electron singularity in X-ray photoemission and X-ray line spectra from metals. *Journal of Physics C: Solid State Physics* **1970**, *3*, 285.

[10] Shirley, D. A. High-Resolution X-Ray Photoemission Spectrum of the Valence Bands of Gold. *Physical Review B* **1972**, *5*, 4709.

Chapter 3

Ethylene thermal decomposition on the Ir(1 1 1) surface

Temperature Programmed Growth (TPG) of graphene on the Ir(1 1 1) surface by using ethylene as a precursor molecule is known to give an exceptional quality graphene single layer [1–4]. This process, where the precursor molecules are adsorbed at room temperature and subsequently heated to promote dissociation and graphene nucleation for several times in adsorption-dissociation-growth cycles, is often preferred to growth at a fixed temperature for high quality graphene monolayers on transition metal surfaces [1, 5, 6]. In the case of TPG on Ir(1 1 1) using ethylene as the precursor, ethylene is efficiently converted to graphene, and Smoluchowski ripening of graphene clusters originating at step edges [2] gives an almost complete graphene layer itself with a single orientation and with a very low density of defects. For this reason, we decided to study the initial steps of this process, where the ethylene molecules undergo several chemical reaction steps that will eventually generate carbon atoms, the building blocks necessary for graphene growth. We employed high-resolution X-ray Photoelectron Spectroscopy (XPS) and Temperature Programmed XPS (TP-XPS [7]), along with calculations of core level binding energies, to identify the surface species and their evolution as the surface temperature is increased from 90 K to 1050 K, where graphene formation is spectroscopically observed. This approach, where XPS spectra are compared to DFT calculation for the corresponding core levels, can greatly aid in giving further insight to measurements performed without such knowledge [8], but is not always straightforward, as some chemical species may have core level binding energies that overlap or are closely spaced. If the high spectral resolution of synchrotron based XPS is not sufficient to unequivocally assign all spectral components, calculations for the vibrational spectra can, in some cases, be performed for the unambiguous spectral identification of chemical species containing, for example, C-H bonds

that generate vibrational replicas in the photoemission spectra. In this experiment, a collaboration was undertaken with Prof. Lev Kantorovich's group at King's College London. They performed numerical calculations for the adsorption energies of all possible C_2H_4 dissociation products, C 1*s* core level binding energies, and dissociation barriers for all these species, and vibrational energies for the core-excited states of relevant molecules.

3.1 Photoemission experimental results

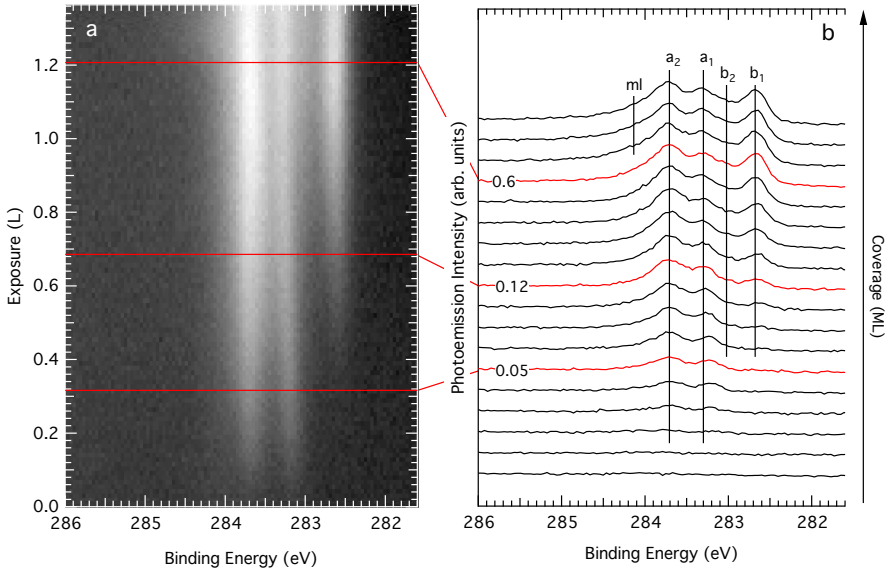

Figure 3.1: (a) Time Resolved XPS series for C 1*s* core levels during ethylene uptake at 90 K. (b) The same data, but displayed as a waterfall plot with only 1 in 7 spectra shown. The three spectra highlighted in red correspond to the three coverages used throughout the experiment. The labels designate the components as identified in the text.

The procedure used for cleaning the Ir(1 1 1) surface is described in Ch. 2, and all XPS spectra have been acquired with 400 eV photon energy at normal emission. In all our experiments, the Ir(1 1 1) surface was exposed to ethylene (partial pressure between 1×10^{-9} and 2×10^{-9} mbar) at 90 K. The sample was then heated with a temperature ramp of 1.5 K/s. In the first part of our investigations, we measured coverage and temperature dependent C 1*s* XPS spectra to follow the evolution of the system as a function of coverage and temperature, thus providing a first qualitative insight into the chemical environment at each step of the adsorption and dissociation processes and the role

of the ethylene surface coverage. In a second stage we measured high resolution C 1*s* core level spectra after annealing the system to specific temperatures, selected on the basis of the TP-XPS results. Such high resolution, high statistics measurements have been necessary because of the multitude of relevant chemical species that, in principle, could be found on the surface in the dissociation process. Most of the reaction products, due to the nature of the experiment, are expected to be somewhat similar to each other, as only small changes are made to the molecules at each step of the reaction. In many cases, the chemical environment seen by each individual carbon atom is only slightly perturbed.

The C surface concentration for the three coverages studied were estimated by comparing the C 1*s* core level intensity to the same spectrum acquired for monolayer graphene on Ir(1 1 1) [9], so that 1 monolayer (ML) is equivalent to a C atom surface density of $1.57 \times 10^{15}\,\mathrm{cm}^{-2}$. Fig. 3.1(a) shows a time resolved series of C 1*s* core level spectra acquired during ethylene exposure at 90 K. At the beginning of the uptake we observe two components at binding energies (BE) of 283.3 eV (a_1) and 283.8 eV (a_2) (see Fig. 3.1(b)). Their intensity increases coherently with increasing exposure, preserving a constant intensity ratio and BE difference. This behavior can be interpreted in terms of the presence of a single adsorbed molecular species with two non-equivalent C atoms, suggesting that the C-C bond is preserved after adsorption. By observing the time resolved XPS spectral series during ethylene adsorption, we were able to detect, above 0.06 ML, the appearance of a new doublet at lower BE due to a different C_2H_m species. While the peak at 282.7 eV (b_1) can be easily distinguished, the second peak (b_2) is partially hidden by the $a_{1,2}$ components, and results in a spectral shoulder slightly above 283 eV. With a further increase in the C_2H_4 exposure, at 0.6 ML, a new broad feature can be observed at BEs higher than 284 eV (*ml*). The observation that in the absence of ethylene flux its intensity rapidly decreases is consistent with the presence of ethylene multilayers. This behavior is expected for weakly interacting species at the condition of surface adsorption-desorption equilibrium [10]. In light of the uptake kinetics, we carried out TP-XPS experiments for three different initial ethylene exposures (highlighted in red in Fig. 3.1), corresponding, from the bottom to the top, to the presence of just the first $a_{1,2}$ spectral doublet (0.05 ML), to a mix of the two doublets (0.12 ML), and to the saturated surface, before the multilayer growth (0.60 ML), respectively.

In Fig. 3.2(a-c) we report the 2D plots corresponding to the TP-XPS C 1*s* spectral series acquired during annealing from low to high temperature. The chemical evolution occurring at the surface is reflected in strong BE shifts and modifications of the C 1*s* core level line shape. In particular, we observe sharp transitions at about 250 K, 380 K and 500 K (high coverage series), while at high temperature ($T = 800$ K) the C 1*s* spectrum smoothly becomes narrower and moves to a higher BE, displaying a line shape which is compatible with the presence of carbon nanodomes [9]. At the highest temperatures, above 900 K,

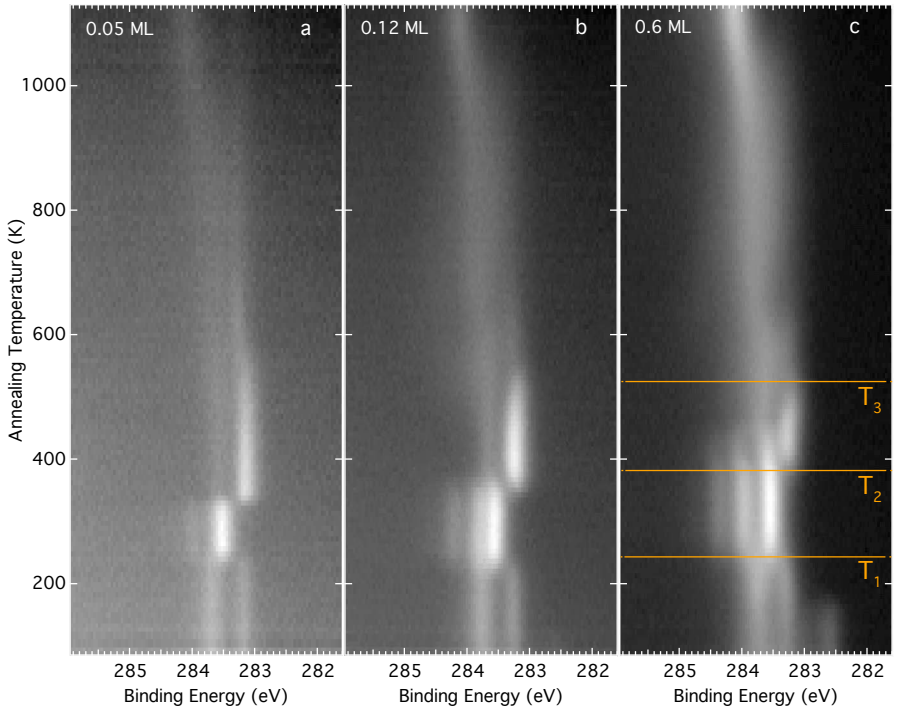

Figure 3.2: Plots of the TP-XPS measurements performed for ethylene adsorbed on the Ir(1 1 1) surface. In these 2D plots, each horizontal line is an XPS spectrum acquired at a different temperature. The three plots shown correspond to the three different coverages considered in this experiment: in (a) the lowest coverage with 0.05 ML of carbon, in (b) an intermediate coverage with 0.12 ML, and in (c) the highest coverage, with 0.6 ML.

the appearance of a spectral component at a BE of 284.1 eV is observed, which is the fingerprint of the initial nucleation of graphene islands on Ir(1 1 1) [8, 9]. Most importantly, the C 1*s* core level evolution is only slightly influenced by the initial C coverage. In fact, the qualitative behavior is similar for the three selected coverages; only the temperature range of each transition is slightly modified, especially for the lower coverage.
The most important spectral change in the low temperature range T_1 (Fig. 3.2(c)) is the decrease of the $b_{1,2}$ components, which transform into $a_{1,2}$. This suggests that, at $T = 90$ K, the lower BE doublet can originate from ethylene species that adsorb without dissociation on the empty sites of the surface initially covered with dissociated C_nH_m species, and that complete depletion of C_2H_4 takes place only above 200 K. The TP-XPS spectra are more complicated to interpret in the temperature ranges T_2 and T_3 (Fig. 3.2(c)) because of the overlap of spectral features originating from non-equivalent C atoms of different C_nH_m species with other components due to vibrational splitting.

Indeed, it is known that, when measured with high resolution, the C 1*s* core level spectra of small hydrocarbon molecules can display vibrational fine structure due to the excitation of C-H vibrational motion in the final state [11, 12]. For this reason, we performed low temperature, high statistics and high resolution C 1*s* photoemission experiments after annealing the high coverage ethylene structure at increasing selected temperatures. The results, when combined with DFT calculated C 1*s* core level shifts for different chemical species, enabled us to make an accurate interpretation of the different spectral components and their evolution with temperature (see Fig. 3.3(a)). Also, by comparing the high resolution spectra acquired before and after annealing, no significant decrease in C 1*s* total area was detected. This signifies, in agreement with existing Temperature Programmed Desorption (TPD) measurements [13], that no C containing fragments desorb from the surface, and that the major peak detected by the mass spectrometer, corresponding to H_2, accounts for most of the desorption products. In fact the C-containing fragments are expected to be tenaciously held by the Ir(1 1 1) surface [13]. This is also in agreement with the relevant dissociation products adsorption energies calculated in the present study, all of which were found to be greater than 2.9 eV, suggesting none of the intermediate species we observe should desorb. This behavior is clearly different from what is observed in a similar experiment on Pt(1 1 1), where many of the dissociated hydrocarbon fragments have been detected also in TPD experiments [14].

To assess the geometrical structure of our system, we also performed low-energy electron diffraction (LEED) measurements. Fig. 3.4(a) shows a LEED pattern acquired after ethylene deposition at 90 K up to saturation, followed by annealing at 340 K. Besides the diffraction spots originating from the Ir(1 1 1) substrate (black), we observe an additional set of spots related to the superstructure formed by the adsorbed molecules (red, cyan and yellow). The diffraction

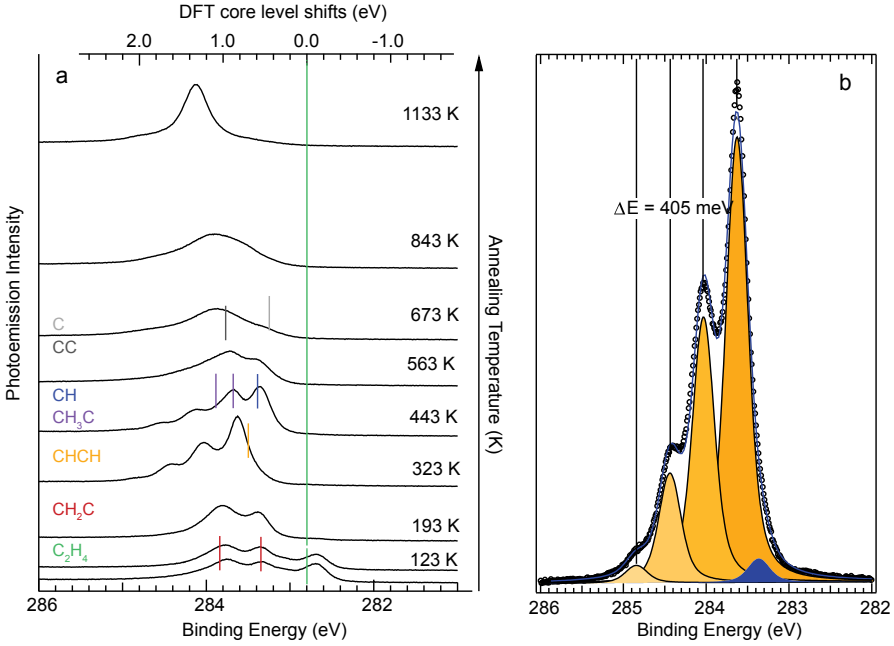

Figure 3.3: High-resolution and high-statistics XPS spectra acquired after annealing the ethylene covered substrate to selected temperatures. In (a), from the bottom upwards, spectra acquired after exposure at 90 K, and after annealing at increasing temperatures. The DFT calculated BEs for the species (shown on the left with different colors) found to be present on the surface have been marked with the same color ticks. In (b), a fit of the spectrum acquired after annealing the system to 323 K is shown. This spectrum shows, besides the main adiabatic peak, a series of vibrational replicas, whose splitting was found to be 405 meV. A small amount of CH (blue peak) is also detected.

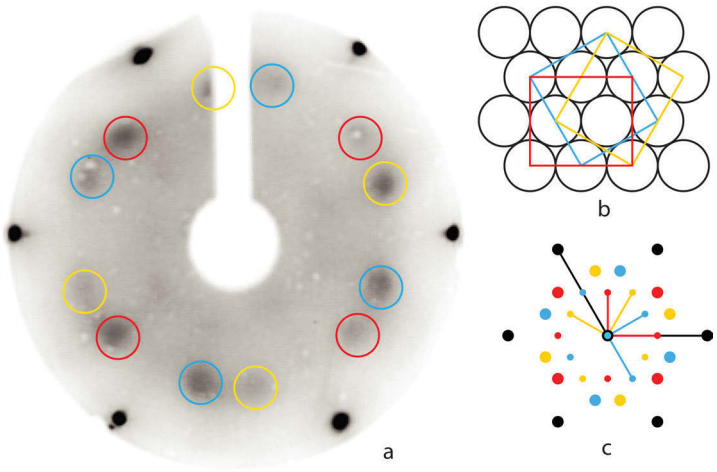

Figure 3.4: (a) LEED pattern acquired at 55 eV after ethylene deposition (0.61 ML) and annealing to 340 K, (b) real space model and (c) simulated diffraction pattern for a c(4 × 2) superstructure with three rotated domains.

pattern is interpreted in terms of a c(4 × 2) structure, with three differently oriented domains, as shown in Fig. 3.4(b, c).

3.2 Interpretation of C 1s core level spectra

In order to give a detailed interpretation of the many components observable in the C 1*s* spectra during the annealing ramps, and hence to be able to deduce the ethylene to carbon conversion mechanism, we relied on DFT calculations made for the C 1*s* core level BEs for all the possible C_nH_m species (see Table 4.1), including final state effects due to the core-hole screening. The results in Fig. 4 show the relative core level shifts, reported with respect to molecular ethylene adsorbed on Ir. Although these chemical shifts can be as large as 1.2 eV, it is often the case that they are much more closely spaced. Correspondingly, high-resolution and high-statistics C 1*s* core level spectra have been acquired after annealing to selected temperatures (see Fig. 3.3(a)). The temperatures have been chosen from the TP-XPS data to be representative of the temperature ranges shown in Fig. 3.2(c). Furthermore, Nudged Elastic Band (NEB) [15–17] calculations were performed between the most stable molecular species and all possible reaction products, so that direct and reverse reaction barriers were found (see Table 3.2 and Fig. 3.5), allowing the experimental data to be critically interpreted.

Note that, due to the nature of the method used for calculating the core levels [18], only relative BEs are of significance; hence an alignment of the DFT

Ethylene fragment	Chemical Shift (eV)
CH_2	0
CH_2CH	0.03, 0.30
CH_3CH	0.62, 0.32
CH_3C	1.08, 0.88
CH_3CH_2	0.41, -0.14
CH_2C	0.55, 1.04
CHCH	0.69
CHC	1.16, 1.27
CC	0.96
CH_3	-0.41
CH_2	0.01
CH	0.59
C	0.45

Table 3.1: Theoretical chemical shifts for the C 1*s* core levels of all relevant dissociation products of ethylene

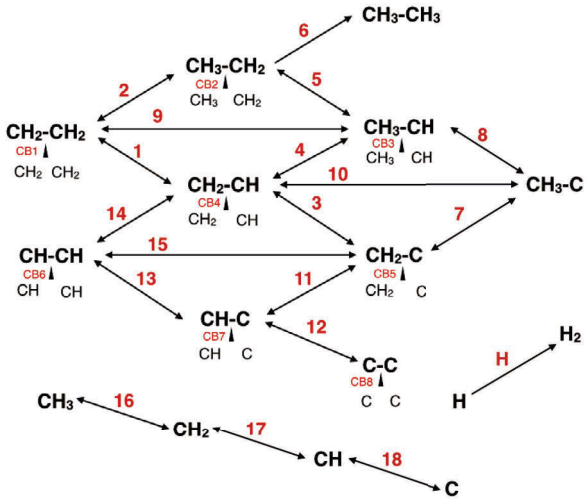

Figure 3.5: Possible reaction steps considered for the conversion of ethylene into atomic C. Upward and downward diagonal arrows represent hydrogenation and dehydrogenation reactions, respectively, while the horizontal arrows show isomerization processes. C-C breaking reactions (labelled as CB) are indicated beneath each species with small vertical arrows.

	Reaction	E_f	E_b
1	$CH_2CH_2 \longrightarrow CH_2CH + H$	0.39	0.58
2	$CH_2CH_2 + H \longrightarrow CH_3CH_2$	0.70	0.35
3	$CH_2CH \longrightarrow CH_2C + H$	0.34	0.59
4	$CH_2CH + H \longrightarrow CH_3CH$	0.64	0.27
5	$CH_3CH_2 \longrightarrow CH_3CH + H$	0.33	0.49
6	$CH_3CH_2 + H \longrightarrow CH_3CH_3$	2.16	–
7	$CH_2C + H \longrightarrow CH_3C$	0.84	0.99
8	$CH_3CH \longrightarrow CH_3C + H$	0.46	1.48
9	$CH_2CH_2 \longrightarrow CH_3CH$	1.39	1.20
10	$CH_2CH \longrightarrow CH_3C$	1.37	2.01
11	$CHC + H \longrightarrow CH_2C$	0.54	1.17
12	$CHC \longrightarrow C{-}C + H$	1.23	0.65
13	$CHCH \longrightarrow CHC + H$	1.23	0.58
14	$CHCH + H \longrightarrow CH_2CH$	1.8	0.55
15	$CHCH \longrightarrow CH_2C$	2.44	2.52
16	$CH_3 \longrightarrow CH_2 + H$	0.5	0.58
17	$CH_2 \longrightarrow CH + H$	0.09	0.83
18	$CH \longrightarrow C + H$	1.11	0.66
CB1	$CH_2CH_2 \longrightarrow CH_2 + CH_2$	1.45	0.61
CB2	$CH_3CH_2 \longrightarrow CH_3 + CH_2$	1.56	1.47
CB3	$CH_3CH \longrightarrow CH_3 + CH$	0.89	1.31
CB4	$CH_2CH \longrightarrow CH_2 + CH$	1.07	1.44
CB5	$CH_2C \longrightarrow CH_2 + C$	1.29	0.21
CB6	$CHCH \longrightarrow CH + CH$	0.82	1.15
CB7	$CHC \longrightarrow CH + C$	0.73	1.29
CB8	$CC \longrightarrow C + C$	1.18	1.29
H	$H + H \longrightarrow H_2$	1.25	–

Table 3.2: Energy barriers for all the reactions considered. E_f is the energy barrier associated with the forward direction of the arrow, whereas E_b is the backward reaction barrier.

calculated core level shifts with the experimental BE scale was performed. This has been achieved by matching the binding energies between the calculated BE for the C 1*s* core levels for CH_2C and experimental values obtained by fitting the main spectral feature in the low temperature high-resolution spectrum with Doniach-Šunjić (D-S) line shape [19] convoluted with a Gaussian. This particular species has been selected over ethylene because, by choosing intact C_2H_4, all the following reaction products' calculated BEs would be located at higher BE values than any of the observed peaks, including carbon species. The only reasonable explanation is that ethylene is already partly dissociated at 90 K. The next most likely species to be found at lower temperatures is CH_2C. In fact, the system is most likely progress by following reactions (1) and (3) to form CH_2C, which has a large dissociation barrier and is therefore expected to be quite stable. This species has two non-equivalent C atoms and can account for two core level components, as seen in the lowest curve in Fig. 3.3(a). Nevertheless, the low BE feature detected at low temperature for coverages greater than 0.06 ML, is assigned to molecular ethylene, which is also present on the surface, although only as a minor component for lower coverages, as confirmed by the corresponding DFT calculated BE value falling close to its position. Observed deviations of DFT calculated BEs from experimental values can be accounted for by considering the presence of a dense layer, with non-negligible lateral interactions, which can cause the C atoms within the molecules to be in slightly different local chemical environments.

Once the alignment has been performed, the observed peaks can be assigned to specific species on the basis of the DFT calculated BE shifts, as reported in Fig. 3.3(a). For one chemical species a core level vibrational splitting of the core-hole excited C atom (denoted C*) is observed (Fig. 3.3(b)) in the energy range compatible with the vibration of the C*-H stretching mode for hydrocarbons. This split is characteristic of each chemical bond, and can be used as a fingerprint to determine the origin of a particular feature in the spectra. A fit of this spectrum, shown in Fig. 3.3(a), has been performed with all the D-S line shape parameters constrained so that the vibrational replicas have the same line shape as the adiabatic peak itself. The splitting between the replicas has also been constrained so that all the replicas appear at equal energy intervals. This procedure gives a best fitting value for the vibrational excitation energy of 405 meV, which is in good agreement with the DFT calculated C*-H vibrational energy of 380 meV for CHCH with core-hole excited C atom; C*-H vibrational energies for other hydrocarbon species were found to be 40 meV lower. This unequivocally identifies the chemical species in the orange spectrum of Fig. 3.3(a) as CHCH, as the calculated BE for CHCH is the closest single component C 1*s* core level to that of the main (adiabatic) peak from the fit of the spectrum in Fig. 3.3(b). It further allows us to determine that for the spectrum at 450 K CH is present together with CHCH (the calculated BE of CH being the closest to the observed peak), and that at higher temperatures carbon clusters appear, as confirmed by the calculated BEs for carbon monomers and dimers, which

coincide with observed peaks for the spectra acquired at 550 K.

3.3 Final data analysis: the dissociation path

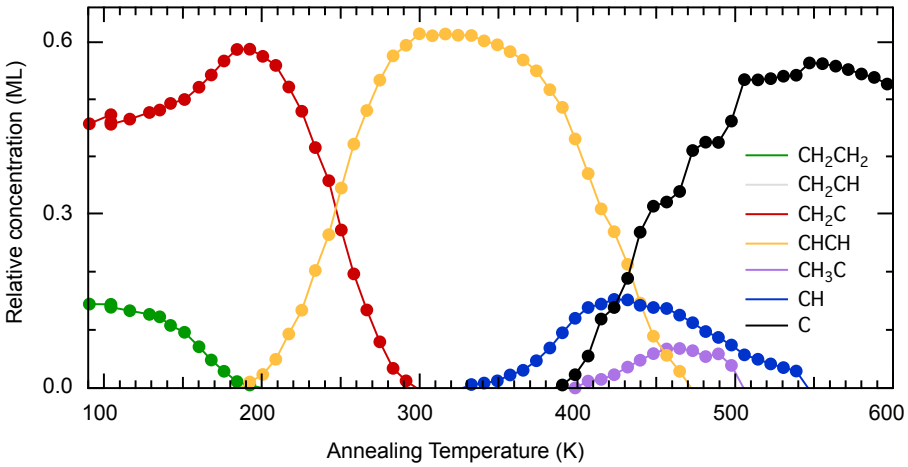

Figure 3.6: The deduced concentration of the principal species on the surface as a function of temperature (which is ramped up linearly with time at a rate of 1.5 K/s) starting from an ethylene coverage of 0.6 ML. CHCH and CH concentrations have been multiplied by a factor 0.66 to correct for photoelectron diffraction effects.

In Fig. 3.6 the integral intensities due to each chemical species, and therefore the relative abundances on the surface, are plotted as a function of temperature. To obtain this plot, in the first part of the analysis, the high resolution data (Fig. 3.3) have been fitted by D-S functions in order to extract the spectral line shape characteristic of each chemical species. Each chemical species is represented by one or two peaks associated to the number of non-equivalent C atoms, and the peak positions are characterized by the calculated BEs. The only exceptions are CHCH, for which vibrational replicas also exist (all the replicas have the same line shape and identical BE splitting), and the various C_n species present at higher temperatures, that have been treated as a single species. In the latter case, also the integral intensity was evaluated cumulatively for all the carbon-only species and is denoted as C in the graph in Fig. 3.6. In the second step, the time-resolved data have been individually fitted with a sum of the spectra obtained as described above. The area of the fitting function for each chemical species was normalized to 1, so that when each spectrum is multiplied by a factor in order to obtain the best fit to the data, this factor is, in fact, proportional to the relative amount of the species on the surface. The spectral shape was kept fixed, while the binding energy of each species' spectrum as a whole was allowed to vary, with respect to the value found for the high

resolution spectra, within a small energy range (0.1 eV) in order to account for lateral interactions between different species. In the case of atoms (oxygen [20]) and light molecules (carbon monoxide [21]) it was found that core electron binding energies display a slight change as a function of adsorbate coverage due to mutual interaction that can be of the order of 100 meV (110 meV for O on Rh(1 1 1) [20], 180 meV for CO on Pd(1 1 1) [21]), even when the adsorption site is unchanged. Some unexpected positive variations in the total integral intensity of the C 1*s* peak were observed, especially in the temperature intervals where CHCH and CH are present and long range order is observed in LEED, leading to a slight increase in the overall C signal, which cannot be due to an increase of the C surface density (see Fig. 3.7, black curve). We interpret this increase in intensity as due to photoelectron diffraction effects when local ordering of the species is improved. To correct the effects of photoelectron diffraction on the dissociation path plots, a multiplication constant of 0.66 was used for the signal of CH and CHCH (see Fig. 3.7, green curve). Concentrations obtained in this way are plotted as a function of annealing temperature in Fig. 3.6 and finally give the thermal dissociation path for ethylene on the Ir(1 1 1) surface.

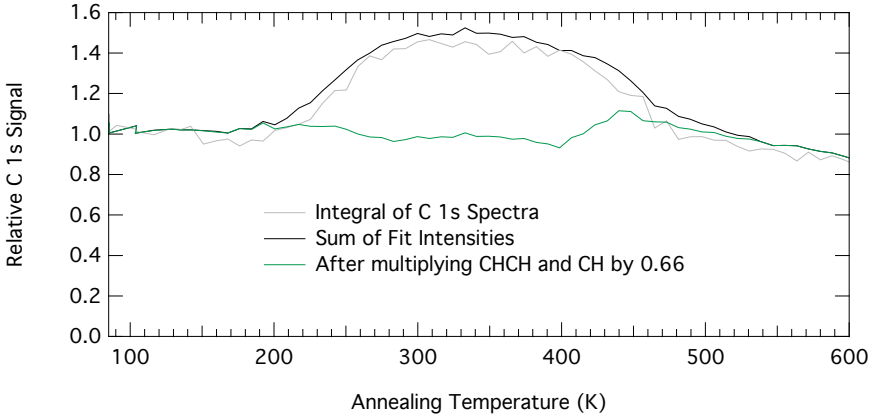

Figure 3.7: Total C signal, as obtained from the TP-XPS spectral series for the 0.6 ML coverage experiment. The gray curve is obtained by integrating the background-subtracted spectra, while the black and the green curves are obtained by summing the relative intensities (see Fig. 3.6) for all the dissociation products. For the green curve, the CH and CHCH intensities have been multiplied by 0.66.

The data suggests the following reaction mechanism. First, CH_2C is formed already at 90 K (molecular ethylene being observed only at higher coverages), which converts completely into CHCH; in turn, CHCH dissociates to CH monomers, which dehydrogenate to produce atomic C and hydrogen. We found that, above 400 K, a small amount of CH_3C is formed from rehydrogenation of CHCH, which reacts with atomic H species found on the surface that are

created in close proximity to the CHCH species, and that reside on the surface long enough to react. It is worth mentioning that the formation of CH_3C from ethylene on Ir(1 1 1) had been previously suggested by Marinova *et al.* [22] The derived reaction path during the temperature ramp, based entirely on core level photoemission spectra and DFT calculated BEs and vibrational frequencies, can be compared to the one deduced following the direction of the reactions with the lowest DFT energy barriers (Table 1). Specifically, since our experiments begin from a relatively low temperature, initially the system will likely progress by following reactions (1) and (3) to form CH_2C corresponding to low dehydrogenation reaction barriers. This fully agrees with the CH_2C concentration evolution shown in Fig. 3.6. With an increase of temperature, five possible pathways become available for CH_2C: it can hydrogenate to either CH_2CH or CH_3C, dehydrogenate to CHC, isomerize to CHCH or undergo C-C breaking to form CH_2 and C. The hydrogenation reactions (3)-reversed and (7) have the lowest barriers of these (0.66 eV and 0.82 eV respectively), and will therefore act as the main competing pathways out of CH_2C. If reaction (7) were followed, CH_3C, which is not observed experimentally at temperatures where CH_2C is present, would have been produced and remained stable for some considerable range of temperatures as the lowest barrier out of this species is the reverse reaction back to CH_2C, which is still high (0.99 eV). If reaction (3) is followed, then CH_2CH is formed. As the barrier back to CH_2C is very small it is likely that this species will immediately dehydrogenate backwards to CH_2C, resulting in a short lifetime to these species and explaining why CH_2CH is not observed experimentally. There is in any case a possibility that some portion of the CH_2C species should follow reaction (14) instead, leading to CHCH. The species evolution curves presented in Fig. 3.6 show that the latter route (CH_2C - CH_2CH - CHCH) appears to be preferable of the two. We next see in Fig. 3.6 that as the concentration of CHCH starts decreasing, CH appears. This is explained by the fact that the reaction with the lowest barrier starting from CHCH is the C-C breaking reaction, CB6, leading to CH species. At even higher temperatures, the formation of carbon clusters C_n is detected as shown in Fig. 3.6. Now the surface is free from hydrocarbon species, and, at slightly higher temperatures, the C adatoms are free to diffuse on the surface and eventually nucleate to form graphene, or more frequently, attach to preexisting graphene islands and contribute to graphene growth.

3.4 Conclusions

At this point, it is possible to say that a comprehensive approach based on XPS experiments and DFT calculations has been applied to acquire a detailed understanding of the mechanism of ethylene thermal decomposition on the Ir(1 1 1) surface. TPG experiments are widely used for growing graphene on transition metal surfaces, and we were able to determine the details for the process that generates the building blocks for graphene growth on Ir(1 1 1).

Furthermore, the combined approach presented here, which has been applied to study a relatively simple, although real-life scenario, showcases the potential of a method which has been employed throughout this thesis, where DFT calculations complement synchrotron-based XPS experiments, which, in turn, provide feedback for additional, targeted calculations in a virtuous cycle.

This approach has allowed to clearly identify the intermediate species that are formed on Ir(1 1 1) following ethylene's thermal decomposition. It should be noted that a previous study [8] had interpreted similar data by exploiting knowledge from related systems, giving however different results. Information provided by the DFT calculations, which were unavailable in the previous work, made it possible to give a rigorous interpretation to the observed photoemission spectra. In our case, the results presented suggest the following pathway, ultimately yielding carbon monomer species:

$$\mathrm{CH_2CH_2} \longrightarrow \mathrm{CH_2CH} + \mathrm{H}$$

$$\mathrm{CH_2CH} \rightleftharpoons \mathrm{CH_2C} + \mathrm{H}$$

$$\mathrm{CH_2CH} \longrightarrow \mathrm{CHCH} + \mathrm{H}$$

$$\mathrm{CHCH} \longrightarrow \mathrm{CH} + \mathrm{CH}$$

$$\mathrm{CH} \longrightarrow \mathrm{C} + \mathrm{H}.$$

In the proposed reaction pathway we find that hydrogenation, dehydrogenation and C-C breaking reactions are required in order to produce carbon on the Ir(1 1 1) surface available for graphene growth. Interestingly, we find the dissociation product CH_3-C, which is thought to be a rate limiting product on other Pt-group (1 1 1) surfaces like Pt(1 1 1) and Pd(1 1 1) [23]. However, in our case, we find it forms only in minor quantities later in the dissociation process, and in competition with CH. This leads to an important feature of this pathway, which is that the C-C bond is broken in order to form carbon monomers and this happens before the molecule is fully dehydrogenated. Breaking of the C-C bond allows for the possibility that graphene is formed from carbon clusters that are predominantly built from C monomers and not dimers, similar to what has been found to happen on Ru(0 0 0 1) [24].

References

[1] Hattab, H.; N'Diaye, A. T.; Wall, D.; Jnawali, G.; Coraux, J.; Busse, C.; van Gastel, R.; Poelsema, B.; Michely, T.; Meyer zu Heringdorf, F.-J.; Horn-von Hoegen, M. Growth temperature dependent graphene alignment on Ir(1 1 1). *Applied Physics Letters* **2011**, *98*.

[2] Coraux, J.; N'Diaye, A. T.; Engler, M.; Busse, C.; Wall, D.; Buckanie, N.; zu Heringdorf, F.-J. M.; van Gastel, R.; Poelsema, B.; Michely, T. Growth of graphene on Ir(1 1 1). *New Journal of Physics* **2009**, *11*, 023006.

[3] Wang, B.; Ma, X.; Caffio, M.; Schaub, R.; Li, W.-X. Size-Selective Carbon Nanoclusters as Precursors to the Growth of Epitaxial Graphene. *Nano Letters* **2011**, *11*, 424.

[4] Miniussi, E.; Pozzo, M.; Baraldi, A.; Vesselli, E.; Zhan, R. R.; Comelli, G.; Menteş, T. O.; Niño, M. A.; Locatelli, A.; Lizzit, S.; Alfè, D. Thermal Stability of Corrugated Epitaxial Graphene Grown on Re(0 0 0 1). *Physical Review Letters* **2011**, *106*, 216101.

[5] Loginova, E.; Bartelt, N. C.; Feibelman, P. J.; McCarty, K. F. Evidence for graphene growth by C cluster attachment. *New Journal of Physics* **2008**, *10*, 093026.

[6] Gao, J.; Yip, J.; Zhao, J.; Yakobson, B. I.; Ding, F. Graphene Nucleation on Transition Metal Surface: Structure Transformation and Role of the Metal Step Edge. *Journal of the American Chemical Society* **2011**, *133*, 5009.

[7] Baraldi, A.; Comelli, G.; Lizzit, S.; Cocco, D.; Paolucci, G.; Rosei, R. Temperature programmed X-ray photoelectron spectroscopy: a new technique for the study of surface kinetics. *Surface Science* **1996**, *367*, L67.

[8] Lizzit, S.; Baraldi, A. High-resolution fast X-ray photoelectron spectroscopy study of ethylene interaction with Ir(1 1 1): From chemisorption to dissociation and graphene formation. *Catalysis Today* **2010**, *154*, 68.

[9] Lacovig, P.; Pozzo, M.; Alfè, D.; Vilmercati, P.; Baraldi, A.; Lizzit, S. Growth of Dome-Shaped Carbon Nanoislands on Ir(1 1 1): The Intermediate between Carbidic Clusters and Quasi-Free-Standing Graphene. *Physical Review Letters* **2009**, *103*, 166101.

[10] Hugenschmidt, M. B.; Dolle, P.; Jupille, J.; Cassuto, A. Ethylene π species on bare and cesiated Pt(1 1 1) surfaces. *Journal of Vacuum Science & Technology A* **1989**, *7*, 3312.

[11] Andersen, J.; Beutler, A.; Sorensen, S.; Nyholm, R.; Setlik, B.; Heskett, D. Vibrational fine structure in the C 1s core level photoemission of

chemisorbed molecules: ethylene and ethylidyne on Rh(1 1 1). *Chemical Physics Letters* **1997**, *269*, 371.

[12] Steinrück, H.-P.; Fuhrmann, T.; Papp, C.; Tränkenschuh, B.; Denecke, R. A detailed analysis of vibrational excitations in x-ray photoelectron spectra of adsorbed small hydrocarbons. *The Journal of Chemical Physics* **2006**, *125*, 204706.

[13] Nieuwenhuys, B.; Hagen, D.; Rovida, G.; Somorjai, G. LEED, AES and thermal desorption studies of chemisorbed Hydrogen and hydrocarbons (C_2H_2, C_2H_4, C_6H_6, C_6H_{12}) on the (1 1 1) and stepped [6(1 1 1) × (1 0 0)] iridium crystal surfaces; comparison with platinum. *Surface Science* **1976**, *59*, 155.

[14] Zaera, F.; Bernstein, N. On the Mechanism for the Conversion of Ethylene to Ethylidyne on Metal Surfaces: Vinyl Iodide on Pt(1 1 1). *Journal of the American Chemical Society* **1994**, *116*, 4881.

[15] Mills, G.; Jónsson, H.; Schenter, G. K. Reversible work transition state theory: application to dissociative adsorption of hydrogen. *Surface Science* **1995**, *324*, 305.

[16] Henkelman, G.; Uberuaga, B. P.; Jónsson, H. A climbing image nudged elastic band method for finding saddle points and minimum energy paths. *The Journal of Chemical Physics* **2000**, *113*, 9901.

[17] Henkelman, G.; Jónsson, H. Improved tangent estimate in the nudged elastic band method for finding minimum energy paths and saddle points. *The Journal of Chemical Physics* **2000**, *113*, 9978.

[18] Köhler, L.; Kresse, G. Density functional study of CO on Rh(1 1 1). *Physical Review B* **2004**, *70*, 165405.

[19] Doniach, S.; Sunjic, M. Many-electron singularity in X-ray photoemission and X-ray line spectra from metals. *Journal of Physics C: Solid State Physics* **1970**, *3*, 285.

[20] Ganduglia-Pirovano, M. V.; Scheffler, M.; Baraldi, A.; Lizzit, S.; Comelli, G.; Paolucci, G.; Rosei, R. Oxygen-induced Rh $3d_{5/2}$ surface core-level shifts on Rh(1 1 1). *Physical Review B* **2001**, *63*, 205415.

[21] Surnev, S.; Sock, M.; Ramsey, M.; Netzer, F.; Wiklund, M.; Borg, M.; Andersen, J. CO adsorption on Pd(1 1 1): a high-resolution core level photoemission and electron energy loss spectroscopy study. *Surface Science* **2000**, *470*, 171.

[22] Marinova, T.; Chakarov, D. Adsorption of ethylene on Ir(1 1 1). *Surface Science* **1987**, *192*, 275.

[23] Aleksandrov, H. A.; Moskaleva, L. V.; Zhao, Z.-J.; Basaran, D.; Chen, Z.-X.; Mei, D.; Rösch, N. Ethylene conversion to ethylidyne on Pd(1 1 1) and Pt(1 1 1): A first-principles-based kinetic Monte Carlo study. *Journal of Catalysis* **2012**, *285*, 187.

[24] Barteau, M. A.; Broughton, J. Q.; Menzel, D. Vibrational spectroscopy of hydrocarbon intermediates on Ru(0 0 1). *Applications of Surface Science* **1984**, *19*, 92.

Chapter 4

Intercalated ultra-thin metal layers: unravelling the roles of surface chemistry and geometry

The next step that was undertaken towards more complex graphene-based nanostructures is a study of one of the simplest imaginable of such nanostructures: ultra-thin intercalated metal layers at graphene-metal interfaces. Intercalation of transition metals is a commonly employed technique used to tune graphene properties, since the properties of pristine graphene layers are strongly influenced by the presence and nature of the substrate. The two most noticeable effects of changing the substrate are a different geometrical structure of the graphene layer so that patterns and waves emerge in the single-atom-thick carbon layer, and deep changes to the band structure. These can be profound to the point that the Dirac cones, one of the most distinct electronic features of graphene, can be completely absent, and the opening of a band gap at the Fermi level can be observed [1]. Clearly, these effects depend on the metallic surfaces, which can be classified depending on the degree of interaction they establish with graphene [2, 3]. Some generally show a weak, van der Waals-like coupling and are characterized by a graphene-surface separation close to the interlayer distance of graphite (around 3 Å), such as Ir(1 1 1) [4] and Pt(1 1 1) [5]. Others display a much stronger interaction, such as Ru(0 0 0 1) [6–8] and Re(0 0 0 1) [9, 10]: in these cases, the graphene-surface distance is reduced, the nearest carbon atoms lying at approximately 2 Å from the metallic surface. The effects on the structural geometry are exemplified in an often found feature in metal-supported graphene: a moiré structure that arises as a result of slightly different lattice parameters. This is a similar phenomenon to aliasing, where one might try to display a fine grid on a pixel-based display, or take a

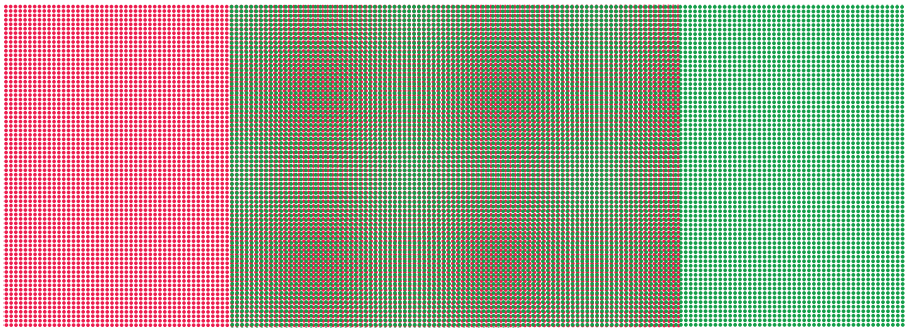

Figure 4.1: An example of a moiré pattern formed by two square lattices with a slightly different lattice parameter. In this specific case, the red lattice is 0.974 times the size of the green lattice. The moiré superlattice in the middle contains about 40×40 red dots and 39×39 green dots.

picture of repeating patterns with a pixel-based sensor, and is a direct consequence of the Nyquist-Shannon sampling theorem [11, 12]. A simple example is shown in Fig 4.1, where two square lattices with slightly different lattice parameter overlap to form a square superlattice. As an example for graphene, if the layer is grown on a hexagonal symmetry surface, and its lattice differs from the substrate lattice only by a scale factor, let's say a 9 to 10 size ratio, a hexagonal superstructure that is 10 times as large as the unit cell will form. These structures are commonly a few nm in size, and are usually somewhat wavy, like a hexagonal egg carton. Actually, the substrate interaction is what determines the shape of these waves, from almost flat in the case of very small interaction, to much more wrinkly in the case of stronger interaction, where each carbon atom sits in a slightly different position over the substrate atoms directly beneath it, to flat again (but with large internal strain) in the case of extreme interaction and closer matching in the lattices, like for graphene on Ni(1 1 1) [13] or Co(0 0 0 1) [14, 15]. Inside the supercell, the individual C atoms will have a variable degree of interaction with the substrate due to the differing positions, especially in the case of transition metals where the *d*-orbitals are quite directional, so that, on average, the graphene layer properties can be affected by the geometry of the moiré super lattice. So of course, the chemical properties of the substrate and their mutual influence on the moiré will play a fundamental role in determining the properties of the graphene overlayer.

Specifically, regarding the chemistry, it is currently known that the interaction of graphene with metal surfaces causes modifications to those properties that make it unique, mainly because of charge transfer processes, rehybridization, and changes to its band structure [16–18]. On the other hand, graphene-metal interaction can preserve the electronic and spin structure of the substrate even when considering surface electronic states, if the interaction is weak enough, as in the case of graphene on Ir(1 1 1) [19]. This allows for the exploitation,

for example, of giant Rashba-type splitting [20] that is present only when such delicate surface properties of metals are intact. This could lead to real-life applications, where even exposure to air does not damage the surface states as would normally happen, thanks to graphene's incredible properties.

As an example of a nanostructure that strongly relies on the control of both these factors, is functionalization by ad-species adsorption over an epitaxial graphene layer. In fact, due to a delicate equilibrium between many factors that strongly depend on the graphene-substrate interaction and the moiré superstructure, it is possible to engineer a bandgap in graphene by adsorbing in specific sites of the moiré for example hydrogen [21] or metal nanoclusters [22, 23].

On the other hand, one can quantify the interaction by extending the Hammer and Nørskov model for the chemisorption of molecules on transition and noble metal surfaces [24] also to graphene/metal systems [6, 25]. This model explains the chemical bonding between molecules and surfaces with a coupling between the valence orbitals of the adsorbates and the metal d-bands. The coupling is maximum when the orbitals of the molecule lie close in energy to the metal d-band center, and it has been shown that all surfaces which exhibit the strongest interaction with graphene have a d-band center lying around 1 eV below the Fermi level, whereas the interaction weakens as the barycenter moves further away from it [3]. Also the spin polarization of graphene on magnetic surfaces such as Ni(1 1 1) can be described in terms of the hybridization between the metal's d-band and graphene's p states [26].

As the current knowledge stood, a better understanding of the interactions occurring at interfaces between graphene and supporting metals was crucial when considering the development of new nanostructures, whether they are based on adsorbed functionalization species, or directly affecting the graphene layer properties, or just exploiting graphene as a capping layer (which requires the properties of the substrate to be left intact). An important part of this understanding relies on the ability to predict the degree of interaction of graphene with the substrate, and in many cases there is still debate as to what determines the interaction strength between graphene and its metal substrate [1, 3].

It is usually the case that both the geometry and the chemical composition of the substrate are changed at once when choosing a different substrate for graphene growth. We therefore designed an experiment to systematically decouple the two tuning parameters, so that the graphene layer was already grown, its geometry fixed, and an epitaxial transition metal single layer was grown beneath it by intercalating the evaporated metal following the scheme shown in Fig. 4.2. Intercalation of metallic species at graphene-metal interfaces [27] is a method that has proved effective, as a glaring example, in almost completely decoupling a graphene layer from the very strongly interacting Ni(1 1 1) surface following the intercalation of a gold layer [28]. The intercalation process modifies the chemical composition of the first surface layer while generally preserving the symmetry and the lattice constant of the substrate, provided the intercalated layer is of monoatomic thickness. In the case of graphene on

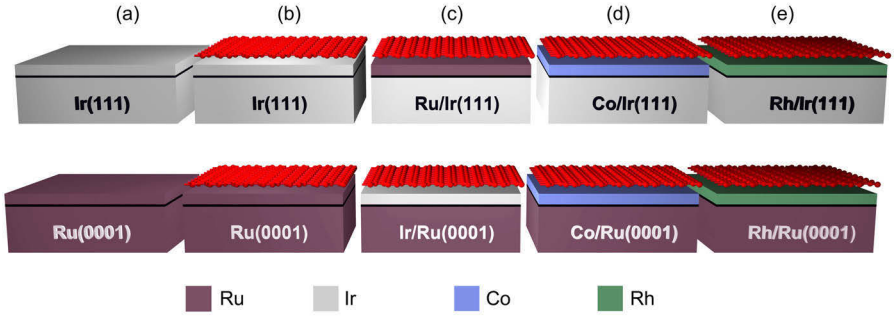

Figure 4.2: Schematic outline of the experimental procedure that was followed. Pristine single-crystal Ir(1 1 1) (top row) and Ru(0 0 0 1) (bottom row) surfaces (a) have been used for epitaxial graphene growth (b). Intercalation of different metallic species at the graphene/metal interface followed (c-e).

Ni(1 1 1) with a following gold intercalation, the system progresses from a flat, strongly interacting graphene layer, where the electronic structure is strongly affected by the Ni substrate, to a quasi-free-standing layer following gold intercalation, that displays Dirac cones in the electronic band structure and even develops a moiré superstructure.

Following the systematic intercalations, we combined our results with numerical calculations performed by Prof. Dario Alfè's group at University College London, and it became possible to separate the contributions to the interaction strength between epitaxial graphene and transition metal surfaces arising from the geometrical and chemical properties of the supporting surfaces. Furthermore, calculations for the valence band of the transition metal substrates allowed for additional insight on the mechanism of the interactions at the graphene/substrate interfaces.

4.1 Description of the experiment

The primary aim of our combined experimental and theoretical investigation was therefore to distinguish the contributions arising from the geometrical (lattice mismatch) and chemical (elemental composition of the substrate) properties of the surface on the interaction between graphene and the substrate metals, and to verify whether C 1*s* core level shifts are directly linked to changes in the surface chemical reactivity of the supporting metal substrates.

In order to make an extensive comparison in controlled and reproducible conditions on model systems, different single-crystal close-packed metallic surfaces were used, one which interacts strongly with graphene (Ru(0 0 0 1), with a lattice constant of 2.71 Å) and one which interacts weakly with it (Ir(1 1 1), with a lattice constant of 2.72 Å). Both substrates have a lattice parameter which

is larger than that of graphene, which has a lattice constant of 2.46 Å. The intercalated species were also chosen in such a way that each of them displays a different degree of interaction with graphene when the latter is grown on their hexagonal close-packed surface: besides Ru and Ir, we employed Rh (which has an intermediate interaction strength with graphene) and Co (which is more strongly interacting than Ru).

To understand the changes in graphene's electronic structure induced by the coupling with different substrates, angular resolved photoemission spectroscopy is very often applied [5, 15, 17, 28–33], as well as X-ray absorption (XANES), Raman, and electron energy loss spectroscopies [18, 29, 34]. However, one of the limits of these powerful approaches is that they do not allow to distinguish carbon atoms in non-equivalent local configurations of the moiré structures which are typically formed by graphene on top of the metal surfaces.

Even cutting edge synchrotron-based high-resolution XPS has its intrinsic limits, given by the finite lifetimes of the core-hole excited final states, and the spectra in this case do not have enough resolution to always be able to distinguish between all the different carbon atoms in the supercell, just because adjacent carbon atoms are so similar to each other. But when coupled to DFT calculations for the core levels, which can be precisely calculated for each individual carbon atom, the distribution of all the different C 1*s* core levels is used to accurately describe the observed XPS line shape [9]. It is this different approach that was now chosen to probe the systems of interest to the experiment.

4.2 Experimental Methods

All experiments were performed in Ultra High Vacuum (UHV) conditions, with base pressure never exceeding 2×10^{-10} mbar, at the SuperESCA beamline [35] and at the Surface Science Laboratory of the Elettra synchrotron radiation facility. All photoemission spectra were measured at the beamline in normal emission conditions. The C 1*s* spectra were measured using a photon energy of 385 eV with an overall experimental resolution of 40 meV. Graphene was grown on Ir(1 1 1) and Ru(0 0 0 1) surfaces using well established procedures [10, 36]. Its quality was verified by measuring in situ the C 1*s* core level spectra and the LEED patterns.

The synthesis of graphene on Ir(1 1 1) was performed using a Temperature Programmed Growth (TPG) technique, consisting of repeated cycles of annealing up to 1400 K in 5×10^{-8} mbar of C_2H_4. SPA-LEED patterns acquired after graphene synthesis (Fig. 4.3(a)) show the superposition of two sharp hexagonal patterns arising from the substrate (inner hexagon) and from graphene (outer hexagon), as well as satellites around all diffraction spots of Ir(1 1 1) generated by the moiré pattern, with the same orientation as the substrate. This indicates that both the graphene layer and the moiré structure are aligned to

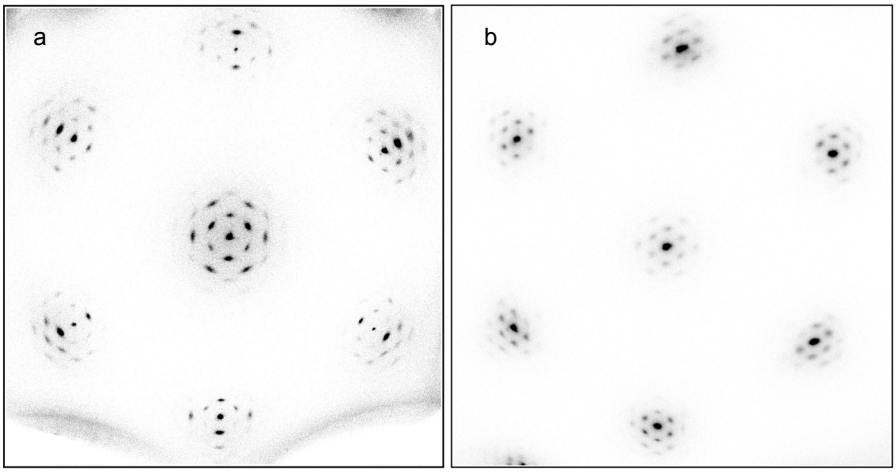

Figure 4.3: SPA-LEED diffraction patterns obtained after graphene growth (a) on Ir(1 1 1) and (b) on Ru(0 0 0 1).

the crystallographic axes of Ir(1 1 1). The FWHM of diffraction spots indicates that graphene forms translational moiré domains having an average size of 270 Å. The angular separation from the zero-order diffraction spot of those generated by the moiré indicates a periodicity of the latter between 9 and 10 Ir(1 1 1) unit cells, in agreement with the incommensurate value of 9.31 found in literature [36].

Graphene was grown on Ru(0 0 0 1) by means of high temperature (1100 K) Chemical Vapor Deposition (CVD) with increasing C_2H_4 pressure up to 5×10^{-7} mbar [8]. This strategy was tuned in order to allow carbon atoms to migrate on the surface to form graphene nucleation islands, but not to diffuse into the bulk. In fact, carbon bulk dissolution can lead, upon cooling of the sample, to the formation of a second layer of graphene [37]. The SPA-LEED diffraction pattern (Fig. 4.3(b)) is qualitatively similar to the one obtained for graphene on Ir(1 1 1), thus indicating that the orientation of graphene was again aligned the substrate. The FWHM of the diffraction spots indicates an average domain diameter of 150 Å. The periodicity of the moiré is compatible with the superposition of a (25×25) superstructure of graphene over (23×23) unit cells of Ru(0 0 0 1) [38].

The intercalation of each metal was obtained by evaporation while keeping the sample surface at 700 K. This temperature was chosen because it allows metal atoms to have enough mobility to diffuse over graphene, until they reach a suitable site for intercalation (mainly grain boundaries) and diffuse below the surface. Conversely, it has been demonstrated that metallic species deposited at ambient temperature usually tend to cluster on top of graphene, without intercalating [22, 39–41].

After each deposition, we verified that the deposited metals had indeed intercalated by monitoring the Ir $4f_{7/2}$ or Ru $3d_{5/2}$ core levels' line-shape. We also compared the C $1s$ spectra before and after the metal deposition. In fact, a completely intercalated metal layer causes an attenuation only in the photoemission signal generated by the substrate, the photoemission intensity of graphene remaining more or less constant. When, on the other hand, a portion of the metal atoms sits above graphene the photoemission intensity of graphene is attenuated as well.

The high energy resolution for the XPS core level spectra allows to resolve the signal generated by surface atoms from that of the underlying layers of each metal, thanks to the fact that the core levels have a different BE depending on the atomic coordination (Surface Core Level Shift). When substrate atoms are covered by the intercalated layer, the coordination of the topmost substrate atoms increases and their core levels become more similar to those of bulk atoms. The intensity of the photoemission component generated by the surface atoms of the substrate I_S can be thus related to the coverage θ. In particular, neglecting edge effects (which are only relevant at lower coverages), the ratio between the area of this component after and before the intercalation is equal to the amount of surface not yet covered:

$$1 - \theta = \frac{I_S(\theta)}{I_S(0)} \tag{4.1}$$

A more accurate estimation of coverage is based on the intensity of the photoelectron signal of the intercalated species I_I, which is proportional to the number of its atoms and therefore linearly increases with coverage, as long as only a single layer is forming. This method however does not allow to directly obtain an absolute value for the coverage, since the proportionality constant between photoemission signal and coverage depends on far too many factors to be estimated *a priori*, and therefore relies on the previous method for calibration. We therefore first analyzed the behavior of I_S as a function of I_I. We then extrapolated the proportionality constant through a linear fit of this function, and finally obtained the coverage by dividing I_I by the proportionality constant thus obtained. The combined analysis of the XPS spectra of graphene, the substrate and the intercalated metals showed that in most cases the intercalation of metals was complete and growth was layer-by-layer.

Still, a small reduction of the graphene photoelectron intensity was observed after the deposition of Rh, indicating that a small part of the deposited rhodium remained above graphene. In this case, in order to calculate the coverage θ, all spectra were normalized by the total C $1s$ signal, since the attenuation effect was the same for all measured levels (being the kinetic energy of photoelectrons almost the same in all our measurements). LEED measurements confirmed that the lattice parameters were not modified by the intercalation, *i.e.* the intercalated layer was epitaxial and pseudomorphic. About 1 ML of metal was deposited for each system, in steps of approximately 0.1 ML.

The evolution of the chemical, structural and electronic properties was followed by acquiring the core-level spectra of graphene (C 1s), and the photoemission spectra of the metallic substrate (either Ir $4f_{7/2}$ or Ru $3d_{5/2}$) and of the intercalated species (Ir $4f_{7/2}$, Ru $3d_{5/2}$, Co $3p_{3/2}$ and Rh $3d_{5/2}$) were, of course, also acquired.

After each intercalation step, the surface was cleaned by means of repeated cycles of sputtering and annealing. The surface cleanliness was again verified through photoemission measurements before regrowing graphene using the same procedures. All photoemission spectra were fitted to a sum of Doniach-Šunjić (DS) lineshapes [42], convoluted with a Gaussian distribution. The inelastic contribution was modeled using a Shirley background [43, 44].

4.3 Numerical Methods

The calculations that backed our experiments were performed using Density Functional Theory [45, 46], and the structures used for the calculations were obtained by overlaying a graphene sheet over a (12×12) and a (9×9) supercell for Ru(0 0 0 1) and Ir(1 1 1) respectively, using a $3 \times 3 \times 1$ grid to sample the surface Brillouin zone. The metal surfaces were modeled using a slab with a thickness of 5 layers, with the atoms of the 2 bottom layers kept fixed at their bulk positions, while all the other atoms were allowed to relax. By modifying the chemical species of the topmost metallic layer it was possible to model the systems obtained from the intercalation of metals below graphene. A vacuum interspace of at least 15 Å (between metallic layers, excluding graphene) was used to minimize the interaction between periodic images of the slab along the direction perpendicular to the surface, resulting in a super-cell of 24 Å along the z axis. 1s Core-level BEs for C atoms have been estimated in the so-called final-state approximation. Also in this case, although the core level energies themselves are not directly accessible because of the frozen core approximation, differences of core level energies are accurately reproduced [47]. The positions of the d-band center E_d with respect to the Fermi energy E_F for the different graphene-free metal surfaces has been calculated as

$$E_d = \int_{-\infty}^{E_0} dE(E - E_F)pd(E) \tag{4.2}$$

where $pd(E)$ is the electronic density of states obtained by projecting the Kohn-Sham orbitals onto spherical harmonics of type d centered on the metal atoms, and E_0 is a cut-off energy that was chosen to be 7 eV above the Fermi energy.

4.4 XPS Data Analysis

All photoemission components of the C 1s core level which appear in all of the systems we analyzed are reported in Table 4.1, together with their BEs.

The analysis of the C 1s spectra of graphene on Ru(0 0 0 1) (Fig. 4.4) was complicated by the overlap of the 1s core level of carbon and the $3d_{3/2}$ core level of Ru. It was therefore necessary, in the analysis of the C 1s spectrum, to include the Ru $3d_{3/2}$ core level, determining its line shape from the $3d_{5/2}$ component. In order to do so accurately, we exploited the fact that the ratio

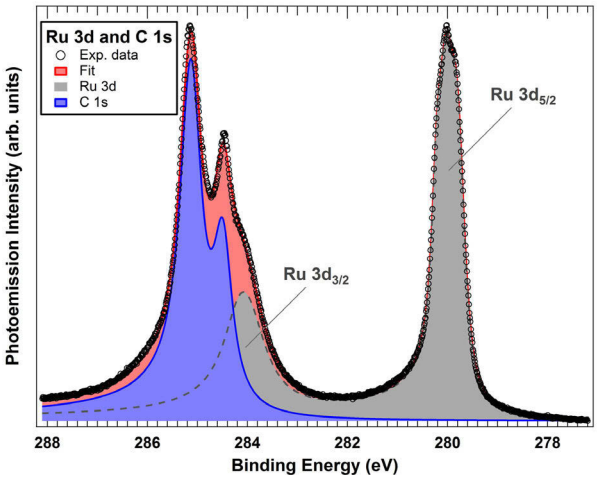

Figure 4.4: Ru 3d and C 1s high resolution photoemission spectrum acquired after Gr growth on Ru(0 0 0 1) ($h\nu$ =385 eV). Experimental data (grey dots) are displayed along with the best fit result (black line). The blue deconvolution component represents the C 1s spectrum for Gr, while the gray deconvolution component corresponds to the Ru 3d levels.

between the intensities of the $3d_{3/2}$ and $3d_{5/2}$ levels depends on spin degeneracy and must therefore be independent of the chemical environment. The line shape is, however, clearly different between the two levels, the former being much broader than the latter, due to different core-hole lifetime and screening processes. As previously observed [48], for each level three different photoemission components could be resolved, due to the non-equivalent Ru geometrical configuration of the first and second layer with respect to the bulk. Furthermore, the BE separation between the three components was different for the clean and graphene-covered Ru(0 0 0 1), and varied during intercalation. It was therefore necessary to establish a procedure to accurately reconstruct the spectrum of the $3d_{3/2}$ level of Ru in order to be able to correctly determine the C 1s spectrum in the subsequent analysis.

So, first of all, the photoemission spectrum of clean Ru(0 0 0 1) was analyzed, starting from the $3d_{5/2}$ level. It was found that the asymmetry parameter was equal for all components, and that the line shape of the component generated by second layer atoms was the same as the one of bulk atoms. The following procedure allowed us to obtain the $3d_{3/2}$ level parameters from those of the $3d_{5/2}$ level and guarantees the best agreement with the experimental results:

- The Gaussian FWHM parameter of each component was equal to the one obtained for the corresponding component of the $3d_{5/2}$ level;
- The asymmetry parameter was the same for all components;
- The BE separation of each component from the one generated by bulk atoms was 0.8 times the value found for the $3d_{5/2}$ level. This might sound surprising, but it is well known that core level shifts can be different for different core levels (as, for example, in the case of Ni and NiO, where the $2p_{1/2}$ to $2p_{3/2}$ splitting can change by up to 1 eV [49])
- The sum of the areas of all components was constrained to 2/3 of the corresponding value obtained for the $3d_{5/2}$ level.

The spectra acquired after the graphene growth (Fig. 4.4) and after the intercalation experiments were therefore analyzed in two steps: first of all the $3d_{5/2}$ level of Ru was analyzed alone. Then the $3d_{3/2}$ level of Ru was fitted together with the $1s$ level of C using the results of the first step. The same procedure has been adopted for the analysis of all spectra acquired during the intercalation of each metal on the Ru(0 0 0 1) surface, as well as for the intercalation of Ru on Ir(1 1 1): in order to accurately analyze the data, we first obtained the line shape parameters from the spectra acquired at the highest coverage of the intercalated species. It was then assumed that the line shape of each component was constant, except for the Gaussian parameter that was allowed to change in order to describe possible contributions due to structural inhomogeneities.

4.5 XPS Results

After analyzing the spectra, it was possible to determine that the C $1s$ spectrum of epitaxial graphene on Ru(0 0 0 1) (Fig. 4.6(a)) shows two distinct components, a weaker one (S3) at 284.47 eV and a narrower and more intense one (S1) at 285.13 eV. The presence of two components is widely recognized as a sign of the corrugation of graphene on Ru(0 0 0 1) [2, 6–8]. They arise from a continuous distribution of non-equivalent atomic configurations where the component at lower BE is mainly generated by the atoms in the higher portion of the corrugation, and the one at higher BE is generated by atoms closer to the substrate, thus showing a more pronounced interaction with the metal underneath [2, 8, 50]. In contrast, the C $1s$ spectrum of graphene grown on Ir(1 1 1) (shown in Fig. 4.5(a)) is dominated by a single very narrow component (W) at a BE of 284.12 eV, which is a fingerprint of quasi free-standing graphene on Ir(1 1 1) [2, 51].

In the series of spectra acquired during each intercalation experiment, it is clear that the C $1s$ spectrum (Fig. 4.5(b-d) and Fig. 4.6(b-d)) changes dramatically as the substrate is covered by the intercalated species.

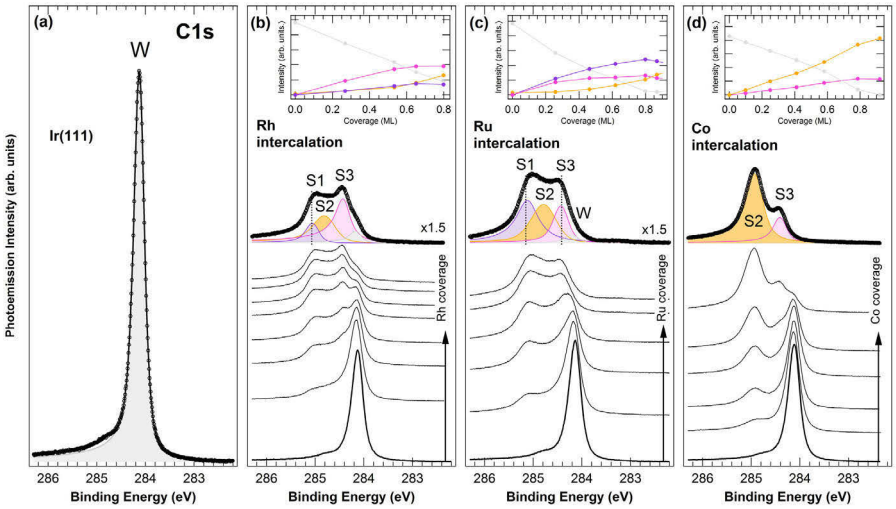

Figure 4.5: C 1*s* core level spectra of graphene/Ir(1 1 1) during intercalation ($h\nu = 385\,\text{eV}$). (a) Graphene/Ir(1 1 1), showing a single component (W). (b-d) Evolution of the C 1*s* spectrum during intercalation of (b) Rh, (c) Ru and (d) Co. Top graphs show the evolution of the area of all C 1*s* photoemission components corresponding to non-equivalent C populations at increasing intercalating metal coverages.

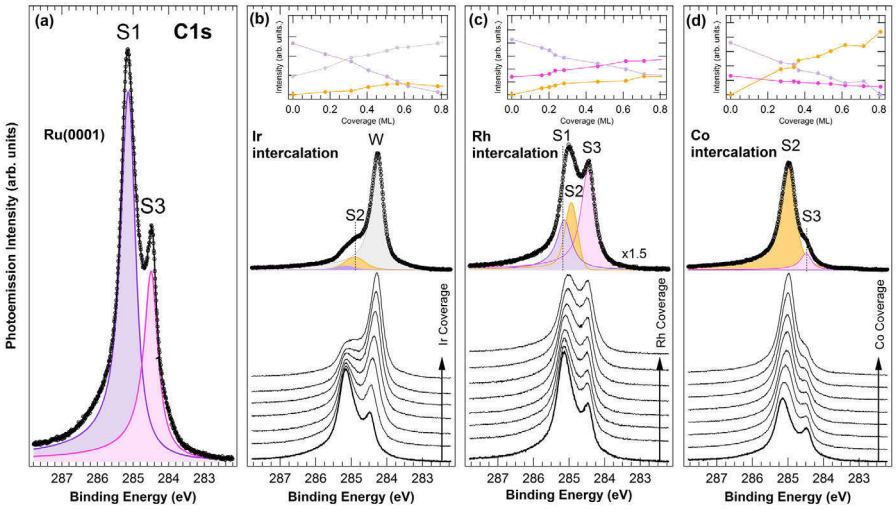

Figure 4.6: Background subtracted C 1*s* core level spectra of graphene/Ru(0 0 0 1) during intercalation ($h\nu = 385\,\text{eV}$). (a) Graphene/Ru(0 0 0 1), with components S1 and S3 corresponding to strongly and weakly interacting carbon atoms respectively. (b-d) Evolution of the C 1*s* spectrum during intercalation of (b) Ir, (c) Rh and (d) Co. Top graphs show the evolution of the area of all C 1*s* photoemission components corresponding to non-equivalent C populations at increasing intercalating metal coverages.

System	S1 (eV)	S2 (eV)	S3 (eV)	W (eV)
Gr/Ir(1 1 1)	-	-	-	**284.12**
Gr/Ru/Ir(1 1 1)	**285.10**	284.75	284.41	-
Gr/Rh/Ir(1 1 1)	285.05	284.83	**284.42**	-
Gr/Co/Ir(1 1 1)	-	**284.93**	284.40	-
Gr/Ru(0 0 0 1)	**285.13**	-	284.47	-
Gr/Ir/Ru(0 0 0 1)	-	284.89	-	**284.23**
Gr/Rh/Ru(0 0 0 1)	285.13	284.91	**284.47**	-
Gr/Co/Ru(0 0 0 1)	-	**284.97**	284.47	-

Table 4.1: Binding energy for each component of the C 1*s* core level photoemission spectrum in the considered systems. The main component in the spectrum of each system is reported in bold. For a description of components S1, S2, S3, and W see Fig. 4.6, Fig. 4.5, and the text.

4.5.1 Intercalation with Ir(1 1 1) substrate

For all of the graphene/metal/Ir(1 1 1) systems (Fig. 4.5(b-d)) we observe that the W component loses intensity upon intercalation, almost completely vanishing for the highest coverage. On the other hand, several components appear at a higher BE, indicating a stronger degree of interaction between graphene and the substrate. The BE of these components does not depend on the coverage, only the relative intensities being modified throughout the experiment.

Specifically, after Rh intercalation (Fig. 4.5(b)) we see a main component at 284.42 eV (S3) and two additional components, with lower intensities, at higher BEs (S1, S2) (Table 4.1). It can be noticed that the BE of the S3 peak is quite similar for this system and for the low BE component of graphene grown on Rh(1 1 1), thus suggesting that this component could arise from areas of the moiré supercell where carbon atoms are further away from the surface. Component S1, on the other hand, is close in BE to the high BE component of graphene on Rh(1 1 1), and is most likely related to carbon atoms strongly interacting with the substrate [52–54]. Component S2, lying in between, most probably arises from atoms in an intermediate configuration between the two.

A similar behavior is observed for the intercalation of Ru on Ir(1 1 1) (Fig. 4.5(c)): also in this case, three components (S1, S2, S3) are detected (Table 4.1), lying between 284.41 and 285.10 eV. These components have BEs close to those found for the Rh intercalation. Their relative intensities, however, are different from the previous case, as the component at higher BE (S1) has a larger (almost double) spectral weight than the low BE one (S3): this could indicate, on average, a stronger interaction with the Ru layer than for the Rh layer. Besides the presence of the S2 component, the spectral distribution is quite similar to the one of graphene directly grown on Ru(0 0 0 1) (Fig. 4.6(a)).

Finally, for the Co evaporation on graphene on Ir(1 1 1), we obtained a large component (S2) at 284.93 eV, and a weaker one (S3) at lower BE (Table 4.1), indicating a generally strong interaction with the Co layer.

By comparing the intercalation experiments on Ir(1 1 1), we notice that the C 1*s* core electrons of graphene (and therefore also its interaction with the substrate) show significant changes depending on the chemical composition of the substrate. In particular, the interaction increases when passing from Ir to Rh, Ru and finally Co, which has, on average, the strongest interaction with graphene among the systems studied.

4.5.2 Intercalation with Ru(0 0 0 1) substrate

Also for the experiments performed on Ru(0 0 0 1) we observe a very different behavior depending on the element being intercalated.

In the case of Ir intercalation (Fig. 4.6(b)) we notice a weakening of component S1, which almost completely disappears, while another weak component is present at lower BE (S2). The intensity of component S3, however, increases until it becomes dominant, while its BE moves linearly towards lower values, reaching 284.23 eV at a coverage of 0.8 ML (Table 4.1). At this point, the spectrum strongly resembles that of graphene grown on Ir(1 1 1) and the dominant component is similar to component W of the latter system. This change in BE can be attributed to a smooth modification of the properties of graphene, from small creases involving few atoms above Ru(0 0 0 1), to a completely raised, weakly interacting graphene above the Ir layer. The presence of the weak component S2 could be attributed to the formation of local defects and to inhomogeneities in the distribution of the Ir atoms.

Also the intercalation of Rh on Ru(0 0 0 1) (Fig. 4.6(c)) leads to an increase in the low BE component (S3). In addition, there are two weaker components (S1, S2) at higher BE (Table 4.1). In this case, though, there are no changes in the BE of any component, indicating that the modifications are limited to a change in populations of weakly and strongly interacting atoms.

Finally, after the intercalation of Co on Ru(0 0 0 1) (Fig. 4.6(d)) the high BE component (S1) is replaced by a new one (S2), at a slightly lower BE (Table 4.1). These two components are always distinct and their BEs remain constant with increasing Co coverage. On the other hand, the low-BE component (S3) decreases: in general the spectral weight moves towards higher BE, indicating a slightly stronger interaction of graphene with Co than with Ru.

In conclusion, we observe a very similar trend to the experiments on Ir(1 1 1), in which the spectrum greatly varies depending on the chemical composition of the topmost layer of the substrate, with which graphene interacts. Also in this case, we found that the interaction with Ir is the weakest, followed by Rh and Ru. Only Co has an interaction with graphene stronger than Ru.

4.6 Numerical results

The DFT data was analyzed and several important pieces of information could be extracted from the relaxed structures and from the correlations between

the calculated core level binding energies for the graphene C atoms and their position within the moiré unit cell.

4.6.1 Corrugation of the graphene layer

Fig. 4.7 (intercalated layer on graphene/Ir(1 1 1)) and Fig. 4.8 (intercalated layer on graphene/Ru(0 0 0 1)) show the theoretically simulated minimum-energy geometric configuration for all the systems studied in this experiment. The color scale indicates the vertical distance (z) of each carbon atom from the surface plane of the metallic substrate. The metallic substrate itself is actually corrugated when it strongly interacts with graphene. This corrugation, however, is an order of magnitude lower than that of graphene. For this reason, the vertical distance has been referred to the mean vertical position of all atoms composing the metallic surface. For all systems, graphene's properties strongly depend on the chemical composition of the topmost layer of the substrate. In particular, where the topmost layer consists of Ir (Fig. 4.7(a) and 4.8(a)), the distance between graphene and the substrate is larger than 4 Å and the former has a very small corrugation. This is in contrast with all other systems, where the distribution is much wider, with the nearest atoms closer than 2 Å to the surface and the farthest between 3.4 and 3.9 Å. For all systems, the unit cells of graphene whose atoms are farthest from the surface are those where the center of the honeycomb lies in an on-top site of the substrate, and therefore both atoms lie in hollow sites. On the other hand, the cells closest to the substrate are those where the centre of the honeycomb lies in bridge sites, and both C atoms lie above a metallic atom.

The distribution along z of the atoms of graphene above a Co layer (Fig. 4.7(d) and 4.8(d)) has a very sharp peak at low z values (between 1.9 and 2.1 Å), with only a small number of atoms located at more than 2.1 Å from the surface (and up to 3.5 Å), 25% of all C atoms on Ir(1 1 1) and 13% on Ru(0 0 0 1).

In the case of graphene on Ru, most of the C atoms lie at a small distance from the substrate (between 2.1 and 2.3 Å). The others, which are more than 25% in the case of graphene/Ru(0 0 0 1) and almost 50% for graphene/Ru/Ir(1 1 1), lie at a larger distance, reaching up to 3.7 Å on the former substrate (Fig. 4.8(c)) and up to 3.9 Å above the latter (Fig. 4.7(c)). The number of weakly interacting C atoms and the range of the C atoms' z values for Ru are larger than for Co, indicating a slightly weaker average interaction.

Finally, the distance of graphene from the Rh layer has a quite uniform distribution which ranges from 2.1 to 3.7 Å for Ru(0 0 0 1) (Fig. 4.8(b)), and from 2.1 to 3.9 Å for Ir(1 1 1) (Fig. 4.7(b)), thus suggesting a smoother corrugation and a weaker interaction of graphene with Rh than with Co or Ru, but still stronger than with Ir.

The calculated distance between graphene and Ru(0 0 0 1) is in good agreement with experimental values found in literature [55]. This is also the case of

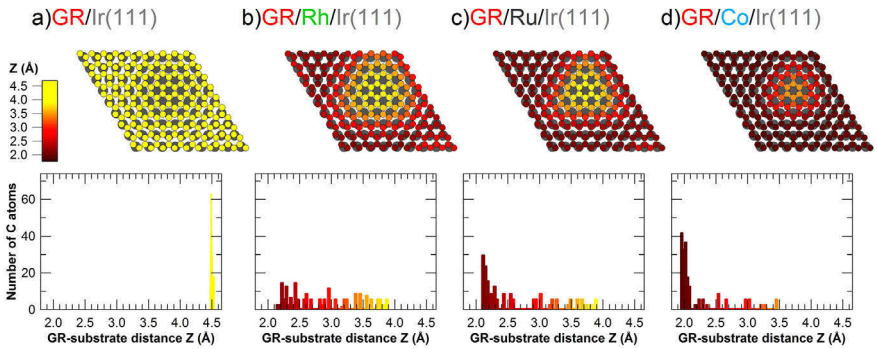

Figure 4.7: Numerical results for different graphene/metal/Ru(0 0 0 1) interfaces. Top panels: geometric configuration of the topmost metallic atoms (large, gray circles) and of the carbon atoms (smaller, colored circles) inside the (13×13) moiré supercell. The C atom color scale indicates the C to substrate distance z. Bottom panels: distribution of all C-metal substrate distance z in the moiré unit cell.

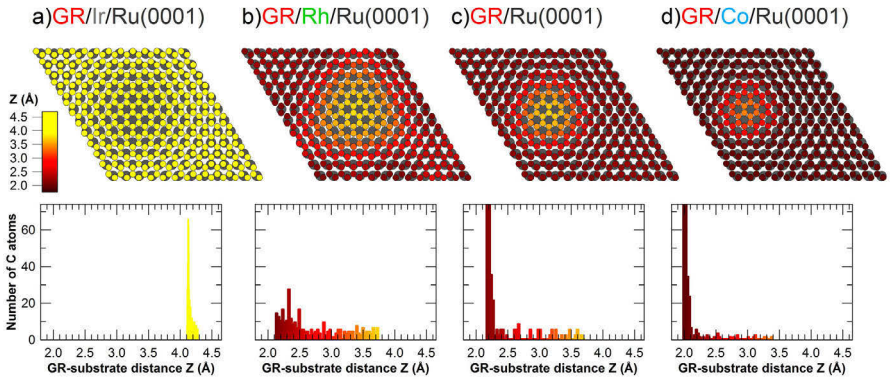

Figure 4.8: Numerical results for different graphene/metal/Ir(1 1 1) interfaces. Top panels: geometric configuration of the topmost metallic atoms (large, gray circles) and of the graphene atoms (smaller, colored circles) inside the (9×9) moiré supercell. The C atom color scale indicates the C to substrate distance z. Bottom panels: distribution of all C-metal substrate distance z in the moiré unit cell.

the separation between graphene and intercalated Co on Ir(1 1 1), which is in very good agreement with previous experiments on the same system [56]. Moreover, the z value of about 2 Å found for the majority of atoms in both systems corresponds to the height found for all atoms of graphene above Co(0 0 0 1), where graphene matches the lattice of the surface forming a 1×1 commensurate structure [3, 14]. The two systems where graphene lies above an intercalated Rh layer have the same corrugation as graphene on Rh(1 1 1) [3, 57]. The separation of graphene from Ir(1 1 1) appears to be overestimated, being by more than 1 Å larger than the interlayer distance of graphite [4]. This can be attributed to the presence of dispersive forces which are not included in the present calculations [25, 58] and which are not negligible in this case.

4.6.2 Core level binding energies of the graphene layer

The DFT calculations were also used to calculate the core level BEs of all C atoms, but since such theoretical methods only provide the relative positions of the C 1*s* BEs for non equivalent atoms, we first had to rigidly shift the energy scale to align its reference to that of the measured data. To this purpose we first aligned the centre of the calculated BE distribution for the Ir(1 1 1) system to the actual experimental data, and then shifted the BE scale for all systems by the same offset. The graphene/Ir(1 1 1) system was chosen because it displayed both the narrowest experimental spectrum and theoretical BE distribution, thus minimizing the error in the calibration. The 1*s* BE distributions of the C atoms inside the moiré supercell for each of our systems are reported in Fig. 4.9 and Fig. 4.10. A different behavior of the C 1*s* BEs distribution can be observed for different chemical compositions of the substrate's topmost layer, regardless of its geometry. Graphene lying above Ir has a very narrow distribution of C 1*s* BEs, centered around 284.20 eV for graphene on Ir(1 1 1) (Fig. 4.9(a)), and between 284.25 and 284.28 eV for graphene on Ir intercalated on Ru(0 0 0 1) (Fig. 4.10(a)).

On the other hand, the distribution is much wider for graphene sitting on Rh, Ru and Co (Fig. 4.9(b-d) and Fig. 4.10(b-d)). Most of the computed C 1*s* BEs, in fact, fall in the range between 284.50 and 285.35 eV and in some systems, such as Ru on Ir(1 1 1) (Fig. 4.9(c)), can reach up to 285.5 eV. What differs among these corrugated systems, however, is the shape of the distribution, which is different depending on the topmost metallic layer. Around 50% of the C atoms lying above Rh have closely spaced C 1*s* BEs ranging between 284.5 and 284.7 eV, while the others are evenly distributed at higher BEs. Most atoms of graphene above Ru have a C 1*s* BE between 285.1 and 285.3 eV, while only around 13% of the atoms above Ru(0 0 0 1) and 25% of those above Ru on Ir(1 1 1) are concentrated at low BE. Finally, C atoms belonging to graphene lying above Co have a sharp peak in their C 1*s* BE distribution centered at around 285.20 eV, with only around 15% of the C atoms having a 1*s* BE lower than 284.7 eV. As can be observed in the bottom graphs in Fig. 4.9 and Fig. 4.10, there is usually a correlation between the distance of each carbon atom from

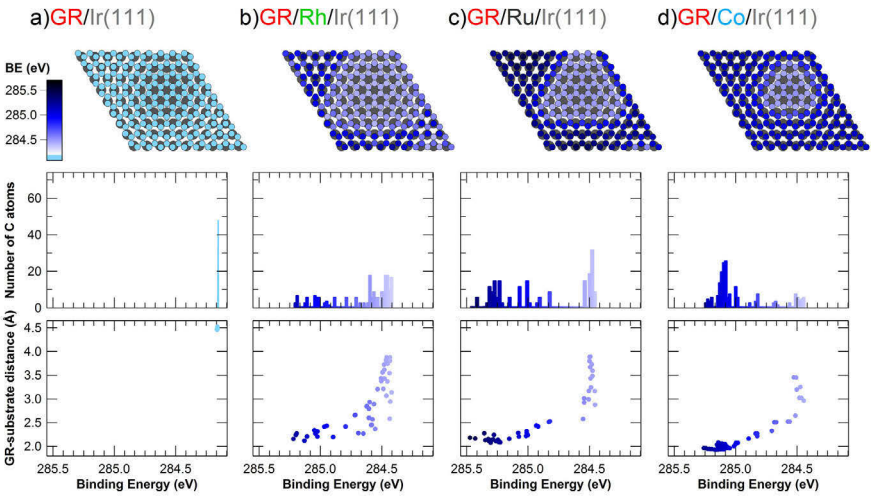

Figure 4.9: Numerical results for graphene/metal/Ir(1 1 1) systems. Top panels: the C 1*s* core level BE is represented for each C atom (small dots) in the moiré cell using a color scale. The larger, gray circles represent the underlying metallic atoms. Middle panels: Distribution of BEs for all C atoms. Bottom panels: correlation between C 1*s* BE and separation of each atom from the topmost metallic layer.

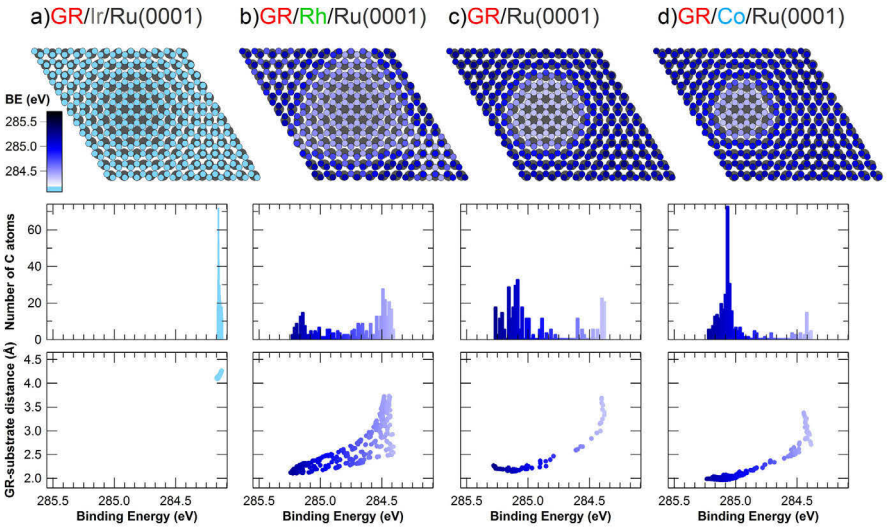

Figure 4.10: Numerical results for graphene/metal/Ru(0 0 0 1) systems. Top panels: the C 1*s* core level BE is represented for each C atom (small dots) in the moiré supercell using a color scale. The larger, gray circles represent the underlying metallic atoms. Middle panels: Distribution for BEs of all C atoms. Bottom panels: correlation between C 1*s* BE and separation of each atom from the topmost metallic layer.

the underlying surface and its C 1*s* BE, with the latter decreasing as the former increases. The situation is more complicated for the case of graphene on Rh (Fig. 4.9(b) and Fig. 4.10(b)), where some adjacent atoms, despite being at the same distance from the substrate (about 2.5 Å), show a large difference (up to 500 meV) in the C 1*s* BE. In this case, in fact, the value of the energy for each atom is related to the site it occupies on the surface: in particular, the BE is maximum for atoms occupying on-top or bridge sites and minimum for threefold hollow sites. This particular behavior has already been observed for epitaxial graphene on Rh(1 1 1) and has been explained in terms of the hybridization of the π states of graphene not only with the d_{z^2} but also with the d_{zx} and d_{zy} bands of Rh [59]. This dependence of the BE on the site is not observed for atoms either too close to the surface (around 2 Å) or too far (above 3 Å).

4.6.3 Strain in the graphene layer

The theoretical simulations also allowed us to compute the average distance of each C atom from its three nearest neighbors. Fig. 4.11 and Fig. 4.12 show the distribution of the distance of each carbon atom from its three nearest neighbors, as obtained by our DFT calculations. This is one of the parameters influenced by geometry: since the moiré unit cell is preserved in the intercalation process, the average separation between C atoms is larger (by around 0.02 Å) in systems having the moiré unit cell of graphene/Ru(0 0 0 1) than in systems having the moiré unit cell of graphene/Ir(1 1 1).

For the systems modeled on the geometry of Ir(1 1 1), the interatomic distances of graphene on Rh have a uniform distribution ranging between 1.41 Å and 1.45 Å (Fig. 4.11(b)). Their distribution above Ru ranges from 1.39 to 1.45 Å with a small peak towards higher values (Fig. 4.11(c)). Finally, the distribution of interatomic distances of graphene above Co (Fig. 4.11(d)) has a sharp peak around 1.43 Å and a tail reaching 1.38 Å. The shape of the distributions, therefore, mostly depends on the chemistry of the topmost layer, whereas the different geometry of the two systems causes a roughly rigid shift of the ranges.

For systems modeled on the geometry of Ru(0 0 0 1), when the topmost layer is composed of Rh (Fig. 4.12(b)), the values of interatomic distance are uniformly distributed between 1.43 and 1.48 Å. When the topmost layer is composed of Ru (Fig. 4.12(c)) this distribution covers the range between 1.42 and 1.47 Å, with a peak towards higher values; finally for graphene above a Co layer on Ru(0 0 0 1) (Fig. 4.12(d)) the distribution has a sharp peak around 1.46 Å and a tail stretching towards lower values reaching 1.41 Å.

By studying the behavior of the C-C separation with respect to the position inside the moiré cell (Fig. 4.11 and Fig. 4.12) and to the separation between graphene and the substrate (Fig. 4.7 and Fig. 4.8), it can be noticed that the distance is usually minimum on the edges of the hills, whereas it is larger in the flat areas both on top of them and at the bottom of the valleys.

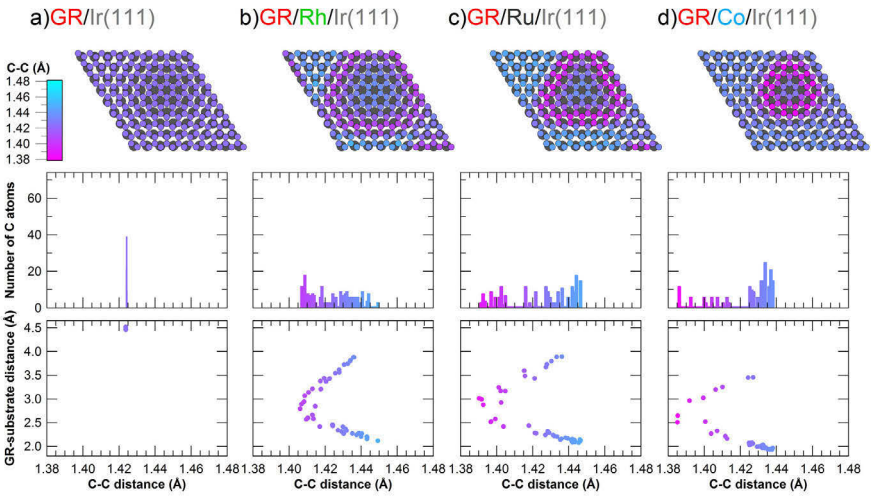

Figure 4.11: Numerical results for graphene/Ir(1 1 1) before and after intercalation. Above: geometric configuration of the topmost metallic atoms (large, gray dots) and of the graphene atoms (smaller, colored dots) inside the moiré supercell: the color scale of the latter indicates the average distance of each C atom from its three nearest neighbors. Middle: Distribution of C-C distances of all C atoms. Below: correlation between C-C distance and separation of each atom from the topmost metallic layer.

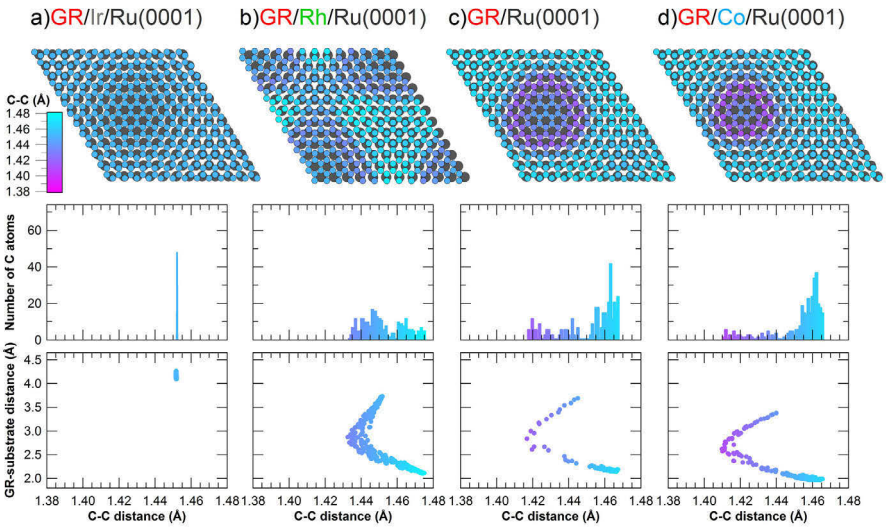

Figure 4.12: Numerical results for graphene/Ru(0 0 0 1) before and after intercalation. Above: geometric configuration of the topmost metallic atoms (large, gray dots) and of the graphene atoms (smaller, colored dots) inside the moiré supercell: the color scale of the latter indicates the average distance of each C atom from its three nearest neighbors. Middle: Distribution of C-C distances of all C atoms. Below: correlation between C-C distance and separation of each atom from the topmost metallic layer.

4.7 Discussion

The similarity between the histograms representing the C 1*s* BE distribution as obtained from the numerical calculations and the measured XPS spectra for each of the systems studied in this work underlines the accuracy and validity of the calculations. In order to further confirm their agreement, we have compared the barycenter of each calculated distribution with that of the corresponding experimental spectrum. To do this with the best possible accuracy, we calculated it for all the coverages up to a monolayer, and then used the value obtained through a linear fit. In most systems, the experimental values agree with the calculated ones, within an uncertainty of 40 meV. The only cases where we found a slightly worse agreement were both systems obtained from Rh intercalation and the one obtained by intercalating Ru at the graphene/Ir(1 1 1) interface. All these systems were characterized by a higher disorder, indicating that these experimental systems were in part different from those simulated in the calculations. In particular, in the first two cases, the reason can be ascribed to the fact that a small portion of Rh atoms were not completely intercalated but also formed clusters on the graphene surface, a behavior previously observed for the low temperature Rh deposition on graphene/Ir(1 1 1) [22].

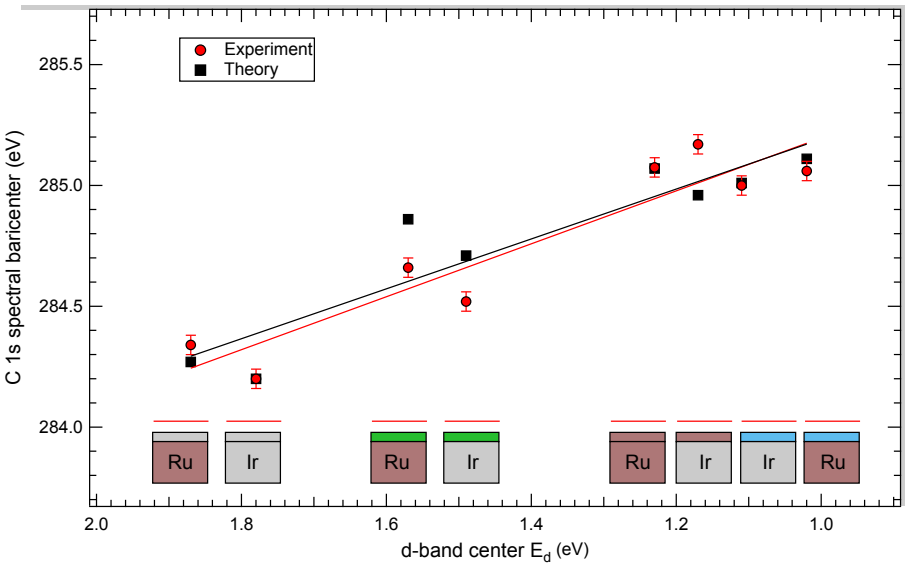

Figure 4.13: Theoretical (black squares) and experimental (red circles) values of the C 1*s* core-level BE distribution's barycenter of all C atoms in the moiré unit cell versus the calculated *d*-band center of the underlying clean metal surface.

From the comparison of the data obtained in the different intercalation experiments, it is clear that there are major differences in the geometric and electronic properties of the graphene layer among systems with a

different chemical species at the interface. For example, the intercalation of Ir on graphene/Ru(0 0 0 1) leads to a very weakly interacting graphene layer, as for graphene/Ir(1 1 1), while intercalation of other metallic species on graphene/Ir(1 1 1) leads to stronger interaction with the substrate, resulting in a buckling of the graphene layer. On the other hand, interfaces having the same chemical species show very similar properties regardless of the difference in the lattice parameter of the supporting substrate and of the resulting moiré superstructure.

These results suggest that the key role in determining the strength of interaction is played by the chemical composition of the substrate. Geometry, on the other hand, mainly determines the periodicity of the moiré, which is preserved after intercalation. This is particularly obvious if we consider the case of graphene interacting with Co: it is flat and commensurate on Co(0 0 0 1) [3], while it is buckled in the case of the Co intercalation. A further proof of the important effects of the electronic structure and the composition of the substrate on its interaction with graphene comes from the correlation between the position of C atoms with respect to the surface sites and their C 1*s* BE. As has been already mentioned, the BE – and therefore the interaction – is maximum for C atoms in on-top configuration and minimum for those in hollow sites, even among atoms located at the same distance from the substrate. This effect demonstrates that the interaction between graphene and metal surfaces depends on the hybridization between the p_z orbitals of C atoms in graphene and the *d*-band of the substrate [24]. In order to find the relationship between the C 1*s* core levels and the chemical properties of the supporting substrates we plotted (in Fig. 4.13) the experimental and theoretical C 1*s* spectral barycenters versus the calculated *d*-band center of the topmost metallic layers. Indeed, as firstly pointed out by Wang *et al.* [7], and more recently extensively described by Toyoda *et al.* [25], *d*-band metals greatly influence the potential-energy surface of graphene on transition-metal surfaces and are largely responsible for the adsorption properties of graphene. Besides the very good agreement between experimental (round markers) and theoretical (square markers) values, we found a strong linear relationship between C 1*s* spectral center of mass and calculated *d*-band centers for the substrate metals. Although core level BEs are certainly affected by final-state effects which are intrinsic to the photoemission process, their contribution does not obscure this linear relationship. This offers a further proof that core level spectroscopy can be considered a useful experimental descriptor of the interaction strength of these graphene-based nanostructures.

4.8 Conclusions

To sum up what has been concluded in this experiment, we have demonstrated that the chemical species of the topmost layer of the substrate plays a major role in determining the strength of interaction between graphene and its substrate. This has been achieved by studying systems in which graphene is supported on

single-crystal transition metal surfaces constrained to the periodicity of Ir(1 1 1) and Ru(0 0 0 1), both from a numerical and experimental point of view. We have further verified that the C 1*s* spectral barycenter has a linear relationship with the underlying transition metal's *d*-band center position, which is recognized to strongly influence the coupling between graphene and the metal surface. As a concluding remark, the approach we newly applied, where a constant feedback was present between the experimental and the theoretical results data analysis, was again very fruitful and allowed for an unprecedented insight in some important aspects necessary for a better control when creating graphene-based nanostructures, in this case ultra-thin intercalated transition metal layers at the graphene/substrate interface.

References

[1] Wintterlin, J.; Bocquet, M.-L. Graphene on metal surfaces. *Surface Science* **2009**, *603*, 1841, Special Issue of Surface Science dedicated to Prof. Dr. Dr. h.c. mult. Gerhard Ertl, Nobel-Laureate in Chemistry 2007.

[2] Preobrajenski, A. B.; Ng, M. L.; Vinogradov, A. S.; Mårtensson, N. Controlling graphene corrugation on lattice-mismatched substrates. *Physical Review B* **2008**, *78*, 073401.

[3] Batzill, M. The surface science of graphene: Metal interfaces, CVD synthesis, nanoribbons, chemical modifications, and defects. *Surface Science Reports* **2012**, *67*, 83.

[4] Busse, C.; Lazić, P.; Djemour, R.; Coraux, J.; Gerber, T.; Atodiresei, N.; Caciuc, V.; Brako, R.; N'Diaye, A. T.; Blügel, S.; Zegenhagen, J.; Michely, T. Graphene on Ir(1 1 1): Physisorption with Chemical Modulation. *Physical Review Letters* **2011**, *107*, 036101.

[5] Sutter, P.; Sadowski, J. T.; Sutter, E. Graphene on Pt(1 1 1): Growth and substrate interaction. *Physical Review B* **2009**, *80*, 245411.

[6] Marchini, S.; Günther, S.; Wintterlin, J. Scanning tunneling microscopy of graphene on Ru(0 0 0 1). *Physical Review B* **2007**, *76*, 075429.

[7] Wang, B.; Bocquet, M.-L.; Marchini, S.; Günther, S.; Wintterlin, J. Chemical origin of a graphene moiré overlayer on Ru(0 0 0 1). *Physical Chemistry Chemical Physics* **2008**, *10*, 3530.

[8] Alfè, D.; Pozzo, M.; Miniussi, E.; Günther, S.; Lacovig, P.; Lizzit, S.; Larciprete, R.; Burgos, B. S.; Menteş, T. O.; Locatelli, A.; Baraldi, A. Fine tuning of graphene-metal adhesion by surface alloying. *Scientific Reports* **2013**, *3*, 2430.

[9] Miniussi, E.; Pozzo, M.; Menteş, T.; Niño, M.; Locatelli, A.; Vesselli, E.; Comelli, G.; Lizzit, S.; Alfè, D.; Baraldi, A. The competition for graphene formation on Re(0 0 0 1): A complex interplay between carbon segregation, dissolution and carburisation. *Carbon* **2014**, *73*, 389.

[10] Miniussi, E.; Pozzo, M.; Baraldi, A.; Vesselli, E.; Zhan, R. R.; Comelli, G.; Menteş, T. O.; Niño, M. A.; Locatelli, A.; Lizzit, S.; Alfè, D. Thermal Stability of Corrugated Epitaxial Graphene Grown on Re(0 0 0 1). *Physical Review Letters* **2011**, *106*, 216101.

[11] Nyquist, H. Certain Topics in Telegraph Transmission Theory. *Transactions of the American Institute of Electrical Engineers* **1928**, *47*, 617.

[12] Shannon, C. E. Communication in the Presence of Noise. *Proceedings of the IRE* **1949**, *37*, 10.

[13] Rosei, R.; De Crescenzi, M.; Sette, F.; Quaresima, C.; Savoia, A.; Perfetti, P. Structure of graphitic carbon on Ni(1 1 1): A surface extended-energy-loss fine-structure study. *Physical Review B* **1983**, *28*, 1161.

[14] Eom, D.; Prezzi, D.; Rim, K. T.; Zhou, H.; Lefenfeld, M.; Xiao, S.; Nuckolls, C.; Hybertsen, M. S.; Heinz, T. F.; Flynn, G. W. Structure and Electronic Properties of Graphene Nanoislands on Co(0 0 0 1). *Nano Letters* **2009**, *9*, 2844.

[15] Varykhalov, A.; Rader, O. Graphene grown on Co(0 0 0 1) films and islands: Electronic structure and its precise magnetization dependence. *Physical Review B* **2009**, *80*, 035437.

[16] Giovannetti, G.; Khomyakov, P. A.; Brocks, G.; Karpan, V. M.; van den Brink, J.; Kelly, P. J. Doping Graphene with Metal Contacts. *Physical Review Letters* **2008**, *101*, 026803.

[17] Varykhalov, A.; Scholz, M. R.; Kim, T. K.; Rader, O. Effect of noble-metal contacts on doping and band gap of graphene. *Physical Review B* **2010**, *82*, 121101.

[18] Schultz, B. J.; Jaye, C.; Lysaght, P. S.; Fischer, D. A.; Prendergast, D.; Banerjee, S. On chemical bonding and electronic structure of graphene-metal contacts. *Chemical Science* **2013**, *4*, 494.

[19] Varykhalov, A.; Marchenko, D.; Scholz, M. R.; Rienks, E. D. L.; Kim, T. K.; Bihlmayer, G.; Sánchez-Barriga, J.; Rader, O. Ir(1 1 1) Surface State with Giant Rashba Splitting Persists under Graphene in Air. *Physical Review Letters* **2012**, *108*, 066804.

[20] Rashba, E. Properties of semiconductors with an extremum loop. 1. Cyclotron and combinational resonance in a magnetic field perpendicular to the plane of the loop. *Soviet physics, Solid state* **1960**, *2*, 1109.

[21] Jørgensen, J. H.; Čabo, A. G.; Balog, R.; Kyhl, L.; Groves, M. N.; Cassidy, A. M.; Bruix, A.; Bianchi, M.; Dendzik, M.; Arman, M. A.; Lammich, L.; Pascual, J.; Knudsen, J.; Hammer, B.; Hofmann, P.; Hornekaer, L. Symmetry-Driven Band Gap Engineering in Hydrogen Functionalized Graphene. *ACS Nano* **2016**, *10*, 10798.

[22] Cavallin, A.; Pozzo, M.; Africh, C.; Baraldi, A.; Vesselli, E.; Dri, C.; Comelli, G.; Larciprete, R.; Lacovig, P.; Lizzit, S.; Alfè, D. Local Electronic Structure and Density of Edge and Facet Atoms at Rh Nanoclusters Self-Assembled on a Graphene Template. *ACS Nano* **2012**, *6*, 3034.

[23] Knudsen, J.; Feibelman, P. J.; Gerber, T.; Grånäs, E.; Schulte, K.; Stratmann, P.; Andersen, J. N.; Michely, T. Clusters binding to the graphene moiré on Ir(1 1 1): X-ray photoemission compared to density functional calculations. *Physical Review B* **2012**, *85*, 035407.

[24] Hammer, B.; Nørskov, J. *Impact of Surface Science on Catalysis*; Advances in Catalysis; Academic Press, 2000; Vol. 45; pp 71.

[25] Toyoda, K.; Nozawa, K.; Matsukawa, N.; Yoshii, S. Density Functional Theoretical Study of Graphene on Transition-Metal Surfaces: The Role of Metal d-Band in the Potential-Energy Surface. *The Journal of Physical Chemistry C* **2013**, *117*, 8156.

[26] Entani, S.; Kurahashi, M.; Sun, X.; Yamauchi, Y. Spin polarization of single-layer graphene epitaxially grown on Ni(1 1 1) thin film. *Carbon* **2013**, *61*, 134.

[27] Dedkov, Y. S.; Shikin, A. M.; Adamchuk, V. K.; Molodtsov, S. L.; Laubschat, C.; Bauer, A.; Kaindl, G. Intercalation of copper underneath a monolayer of graphite on Ni(1 1 1). *Physical Review B* **2001**, *64*, 035405.

[28] Varykhalov, A.; Sánchez-Barriga, J.; Shikin, A. M.; Biswas, C.; Vescovo, E.; Rybkin, A.; Marchenko, D.; Rader, O. Electronic and Magnetic Properties of Quasifreestanding Graphene on Ni. *Physical Review Letters* **2008**, *101*, 157601.

[29] Schultz, B. J.; Dennis, R. V.; Lee, V.; Banerjee, S. An electronic structure perspective of graphene interfaces. *Nanoscale* **2014**, *6*, 3444.

[30] Kralj, M.; Pletikosić, I.; Petrović, M.; Pervan, P.; Milun, M.; N'Diaye, A. T.; Busse, C.; Michely, T.; Fujii, J.; Vobornik, I. Graphene on Ir(1 1 1) characterized by angle-resolved photoemission. *Physical Review B* **2011**, *84*, 075427.

[31] Brugger, T.; Günther, S.; Wang, B.; Dil, J. H.; Bocquet, M.-L.; Osterwalder, J.; Wintterlin, J.; Greber, T. Comparison of electronic structure and template function of single-layer graphene and a hexagonal boron nitride nanomesh on Ru(0 0 0 1). *Physical Review B* **2009**, *79*, 045407.

[32] Pletikosić, I.; Kralj, M.; Pervan, P.; Brako, R.; Coraux, J.; N'Diaye, A. T.; Busse, C.; Michely, T. Dirac Cones and Minigaps for Graphene on Ir(1 1 1). *Physical Review Letters* **2009**, *102*, 056808.

[33] Enderlein, C.; Kim, Y. S.; Bostwick, A.; Rotenberg, E.; Horn, K. The formation of an energy gap in graphene on ruthenium by controlling the interface. *New Journal of Physics* **2010**, *12*, 033014.

[34] Generalov, A.; Dedkov, Y. EELS study of the epitaxial graphene/Ni(1 1 1) and graphene/Au/Ni(1 1 1) systems. *Carbon* **2012**, *50*, 183.

[35] Abrami, A.; Barnaba, M.; Battistello, L.; Bianco, A.; Brena, B.; Cautero, G.; Chen, Q. H.; Cocco, D.; Comelli, G.; Contrino, S.; DeBona, F.; Di Fonzo, S.; Fava, C.; Finetti, P.; Furlan, P.; Galimberti, A.; Gambitta, A.; Giuressi, D.; Godnig, R.; Jark, W.; Lizzit, S.; Mazzolini, F.; Melpignano, P.;

Olivi, L.; Paolucci, G.; Pugliese, R.; Qian, S. N.; Rosei, R.; Sandrin, G.; Savoia, A.; Sergo, R.; Sostero, G.; Tommasini, R.; Tudor, M.; Vivoda, D.; Wei, F.; Zanini, F. Super ESCA: First beamline operating at ELETTRA. *Review of Scientific Instruments* **1995**, *66*, 1618.

[36] N'Diaye, A. T.; Coraux, J.; Plasa, T. N.; Busse, C.; Michely, T. Structure of epitaxial graphene on Ir(1 1 1). *New Journal of Physics* **2008**, *10*, 043033.

[37] Cui, Y.; Fu, Q.; Bao, X. Dynamic observation of layer-by-layer growth and removal of graphene on Ru(0 0 0 1). *Physical Chemistry Chemical Physics* **2010**, *12*, 5053.

[38] Martoccia, D.; Willmott, P. R.; Brugger, T.; Björck, M.; Günther, S.; Schlepütz, C. M.; Cervellino, A.; Pauli, S. A.; Patterson, B. D.; Marchini, S.; Wintterlin, J.; Moritz, W.; Greber, T. Graphene on Ru(0 0 0 1): A 25 × 25 Supercell. *Physical Review Letters* **2008**, *101*, 126102.

[39] Vo-Van, C.; Schumacher, S.; Coraux, J.; Sessi, V.; Fruchart, O.; Brookes, N. B.; Ohresser, P.; Michely, T. Magnetism of cobalt nanoclusters on graphene on iridium. *Applied Physics Letters* **2011**, *99*, 142504.

[40] Zhou, Z.; Habenicht, B. F.; Guo, Q.; Yan, Z.; Xu, Y.; Liu, L.; Goodman, D. W. Graphene moiré structure grown on a pseudomorphic metal overlayer supported on Ru(0 0 0 1). *Surface Science* **2013**, *611*, 67.

[41] Vlaic, S.; Kimouche, A.; Coraux, J.; Santos, B.; Locatelli, A.; Rougemaille, N. Cobalt intercalation at the graphene/Ir(1 1 1) interface: Influence of rotational domains, wrinkles, and atomic steps. *Applied Physics Letters* **2014**, *104*, 101602.

[42] Doniach, S.; Sunjic, M. Many-electron singularity in X-ray photoemission and X-ray line spectra from metals. *Journal of Physics C: Solid State Physics* **1970**, *3*, 285.

[43] Shirley, D. A. High-Resolution X-Ray Photoemission Spectrum of the Valence Bands of Gold. *Physical Review B* **1972**, *5*, 4709.

[44] Végh, J. The analytical form of the Shirley-type background. *Journal of Electron Spectroscopy and Related Phenomena* **1988**, *46*, 411.

[45] Hohenberg, P.; Kohn, W. Inhomogeneous Electron Gas. *Physical Review* **1964**, *136*, B864.

[46] Kohn, W.; Sham, L. J. Self-Consistent Equations Including Exchange and Correlation Effects. *Physical Review* **1965**, *140*, A1133.

[47] Köhler, L.; Kresse, G. Density functional study of CO on Rh(1 1 1). *Physical Review B* **2004**, *70*, 165405.

[48] Lizzit, S.; Baraldi, A.; Groso, A.; Reuter, K.; Ganduglia-Pirovano, M. V.; Stampfl, C.; Scheffler, M.; Stichler, M.; Keller, C.; Wurth, W.; Menzel, D. Surface core-level shifts of clean and oxygen-covered Ru(0 0 0 1). *Physical Review B* **2001**, *63*, 205419.

[49] Moulder, J.; Chastain, J. *Handbook of X-ray Photoelectron Spectroscopy: A Reference Book of Standard Spectra for Identification and Interpretation of XPS Data*; Physical Electronics Division, Perkin-Elmer Corporation, 1992.

[50] Lizzit, S.; Larciprete, R.; Lacovig, P.; Dalmiglio, M.; Orlando, F.; Baraldi, A.; Gammelgaard, L.; Barreto, L.; Bianchi, M.; Perkins, E.; Hofmann, P. Transfer-Free Electrical Insulation of Epitaxial Graphene from its Metal Substrate. *Nano Letters* **2012**, *12*, 4503.

[51] Lacovig, P.; Pozzo, M.; Alfè, D.; Vilmercati, P.; Baraldi, A.; Lizzit, S. Growth of Dome-Shaped Carbon Nanoislands on Ir(1 1 1): The Intermediate between Carbidic Clusters and Quasi-Free-Standing Graphene. *Physical Review Letters* **2009**, *103*, 166101.

[52] Casarin, B.; Cian, A.; Feng, Z.; Monachino, E.; Randi, F.; Zamborlini, G.; Zonno, M.; Miniussi, E.; Lacovig, P.; Lizzit, S.; Baraldi, A. The Thinnest Carpet on the Smallest Staircase: The Growth of Graphene on Rh(5 3 3). *The Journal of Physical Chemistry C* **2014**, *118*, 6242.

[53] Gotterbarm, K.; Zhao, W.; Hofert, O.; Gleichweit, C.; Papp, C.; Steinruck, H.-P. Growth and oxidation of graphene on Rh(1 1 1). *Physical Chemistry Chemical Physics* **2013**, *15*, 19625.

[54] Gotterbarm, K.; Steiner, C.; Bronnbauer, C.; Bauer, U.; Steinrück, H.-P.; Maier, S.; Papp, C. Graphene-Templated Growth of Pd Nanoclusters. *The Journal of Physical Chemistry C* **2014**, *118*, 15934.

[55] Moritz, W.; Wang, B.; Bocquet, M.-L.; Brugger, T.; Greber, T.; Wintterlin, J.; Günther, S. Structure Determination of the Coincidence Phase of Graphene on Ru(0 0 0 1). *Physical Review Letters* **2010**, *104*, 136102.

[56] Pacilé, D.; Lisi, S.; Di Bernardo, I.; Papagno, M.; Ferrari, L.; Pisarra, M.; Caputo, M.; Mahatha, S. K.; Sheverdyaeva, P. M.; Moras, P.; Lacovig, P.; Lizzit, S.; Baraldi, A.; Betti, M. G.; Carbone, C. Electronic structure of graphene/Co interfaces. *Physical Review B* **2014**, *90*, 195446.

[57] Voloshina, E.; Dedkov, Y. Graphene on metallic surfaces: problems and perspectives. *Physical Chemistry Chemical Physics* **2012**, *14*, 13502.

[58] Hamada, I.; Otani, M. Comparative van der Waals density-functional study of graphene on metal surfaces. *Physical Review B* **2010**, *82*, 153412.

[59] Wang, B.; Caffio, M.; Bromley, C.; Früchtl, H.; Schaub, R. Coupling Epitaxy, Chemical Bonding, and Work Function at the Local Scale in Transition Metal-Supported Graphene. *ACS Nano* **2010**, *4*, 5773.

Chapter 5

Growth of graphene on Ru(1 0 $\bar{1}$ 0) and related nanostructures

In the previous chapter, it was demonstrated that, for graphene/metal interfaces, the geometry of the substrate only plays a secondary role in determining the interaction strength. However, it is still quite possible for the substrate's geometry to significantly influence the growth dynamics and topographic features, especially when considering substrates with symmetries other than hexagonal [1–5]. For example, when exploiting anisotropies of the surface, the formation of specifically oriented structures is possible like in the case of graphene grown on Fe(1 1 0) [6] or graphene grown on a vicinal Rh(5 3 3) surface [7]. Strongly anisotropic surfaces have been exploited to create moiré patterns in the graphene/substrate system with unusual 2-fold symmetries, which have characteristic one dimensional features, all with a well determined orientation, as a direct result of substrate anisotropy.

There are interesting technological applications in these nanopatterned surfaces: graphene moiré periodic ripples are known to drive self organization of nanoclusters by exploiting a templating effect [8], so that it becomes possible to form clusters that are well ordered in the troughs of the moiré superstructure. By exploiting one dimensional moiré patterns on an anisotropic Ru surface, we believe that it might become possible to develop novel methods for the fabrication of metal nanowires, with a well defined size and orientation.

Indeed, after a careful review of several adequate transition metal substrates, it was found that Ru(1 0 $\bar{1}$ 0) (see Fig. 5.1 for an image of this termination of an hcp lattice) has a lattice parameter along the [0 0 0 1] direction that closely matches free standing graphene's periodicity along the [1 1 0] direction, to about 1%. Such a close matching is quite unique, and due to a 11:10 commensurate matching along the [0 0 1 0] substrate direction, it was reasonable to expect a degenerate one dimensional moiré superstructure with one-dimensional waves

that are all aligned in a single direction as a direct result of the substrate's anisotropy. In principle, the peculiarity of this matching could allow for an extremely flat graphene layer along the $[0\,0\,0\,1]$ direction, as opposed to other one-dimensional graphene superstructures.

Considering the degree of interaction, graphene/Ru interfaces display an intermediate intensity when compared to some other transition metals, like Au, Pt, or Ir as weakly interacting examples, or Ni and Co for strongly interacting ones. The graphene/Ru interface is therefore in a unique regime, and there is a subtle interplay between C-C and C-Ru interactions. As an example, there exist specific growth conditions where graphene does not energetically favor growth over atomic steps on Ru$(0\,0\,0\,1)$, neither uphill nor downhill, in a process known as single terrace growth mode [9]. The growing graphene layer, however, will not stop once the step edges are reached. The free Ru step downhill of the graphene growth front is actually etched, while the terrace directly beneath the forming graphene layer is expanded, as a result of the uphill migration of the Ru atoms.

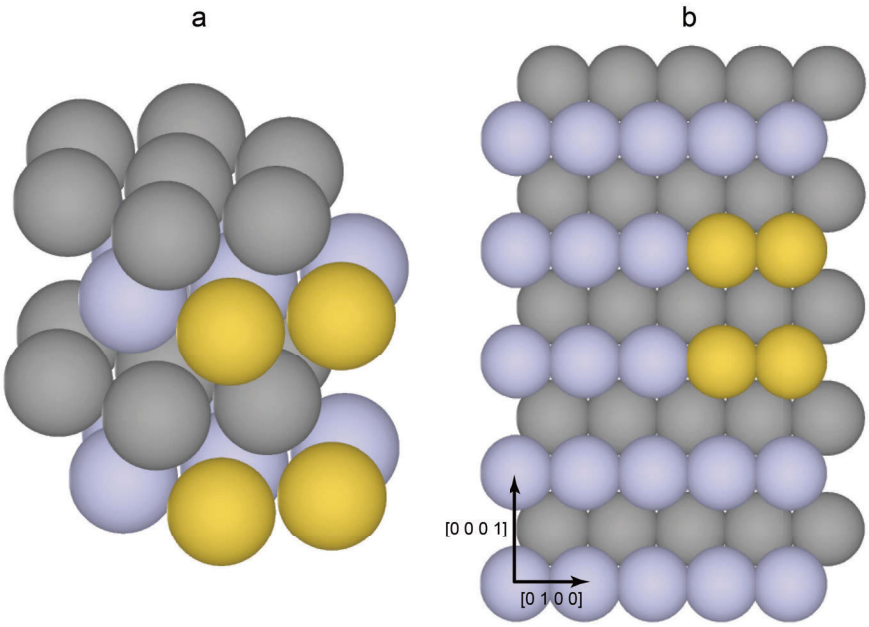

Figure 5.1: Sphere model of a Ru crystal. In (a), the *ABAB* stacking is indicated by blue and gray color. The yellow spheres represent the $(1\,0\,\bar{1}\,0)$ surface termination. In (b), a top view of the $(1\,0\,\bar{1}\,0)$ surface is shown, with the same yellow atoms that were marked in (a).

Following all these observations, we attempted graphene growth on Ru$(1\,0\,\bar{1}\,0)$. The graphene/Ru$(1\,0\,\bar{1}\,0)$ system, however, proved to be much richer than ex-

pected, and many unpredicted phenomena were observed during growth and during temperature changes.

In the first part of this work we tested several CVD growth conditions using ethylene as a precursor, varying the pressure of the C_2H_4 gas and the temperature of the substrate. From the observation of LEED patterns, it was possible to determine the formation of several rotational domains for graphene, including randomly rotated ones. Two commensurate domains (R0 and R30 rotations) give rise to a moiré superlattice with periodicity (1×10) and $c(4 \times 8)$. To test other more complicated growth conditions, such as TPG growth cycles, and to gain information about the domains' morphology and their interaction with the metal, we measured the C 1*s* core level with synchrotron-based HR-XPS. A detailed interpretation was possible thanks to DFT simulations that have been performed by Prof. Dario Alfè from the University College of London, UK. From the simulations it was also possible to determine the morphology of these structures.

In a subsequent set of experiments, we performed a microscopic study of the surface using a Spectroscopic PhotoEmission and Low Energy Electron Microscope (SPE-LEEM) instrument, by which we were able to follow the growth of graphene on Ru$(1\,0\,\bar{1}\,0)$ in real time. It was determined that nucleation of graphene islands during fixed temperature CVD and TPG growth starts near the surface steps, and that our growth procedure results in a full graphene layer that however is in a mixed phase of small (1×10) and $c(4 \times 8)$ domains. The layer was found to be stable up to a temperature of 1200 K, when the carbon atoms start to migrate into the bulk and, at even higher temperatures, the islands quickly dissolve. At this point, by cooling the sample just before all the graphene layer is dissolved, carbon segregates back to the surface and we observed the formation of large graphene single crystalline flakes. The real time imaging capabilities allowed to detect two interesting phenomena: the spontaneous formation of graphene nanoribbons during graphene growth, and a reversible phase transition which depends only on temperature and involves the (1×10) domains.

STM measurements complete the characterization of the stable phases found for graphene grown on Ru$(1\,0\,\bar{1}\,0)$.

5.1 Methods

In order to properly characterize this system, several experimental and computational techniques were applied to study graphene on Ru$(1\,0\,\bar{1}\,0)$. For graphene growth, the Ru$(1\,0\,\bar{1}\,0)$ single crystal was cleaned *in situ* using established procedures for all the experiments [10]. All experiments were performed in Ultra High Vacuum (UHV) conditions.

HR-XPS and LEED measurements were performed at the SuperESCA beamline. All photoemission spectra were measured at the beamline in normal emission conditions. The C 1*s*, Ru $3d_{3/2}$, and Ru $3d_{5/2}$ spectra were measured

together, in a single spectrum, using a photon energy of 385 eV with an overall experimental resolution of 40 meV as for the work on intercalation of Ch. 4. LEED measurements were carried out *in situ* using the available LEED system. All the systems investigated were reproduced in the Surface Science Laboratory UHV chamber, where LEED images have also been acquired. The base pressure was better than 1×10^{-10} mbar in both chambers.

LEEM, μ-LEED, and μ-ARPES (Micro Angle Resolved PhotoEmission Spectroscopy) measurements were carried out at the Nanospectroscopy beamline of Elettra. LEEM experiments were performed with a commercial Elmitec LEEM III system installed at the beamline, and equipped with an imaging electron energy analyzer enabling operation as a SPE-LEEM [11]. This allows for *in situ* microscopy either by employing low energy electrons from an integrated electron gun or by using photoelectrons emitted from the sample, which are excited by the incident synchrotron radiation. The energy range for incident electrons is about 20 eV to 200 eV using the LaB_6 electron gun. When using photons generated by Elettra, the photon energy range is 20 eV to 1000 eV. It is therefore possible to perform μ-ARPES, μ-XPS, and PEEM (PhotoElectron Emission Microscopy) measurements, where the image contrast is given by the photoemission intensity at a given kinetic energy. The base pressure was better than 1×10^{-10} mbar.

STM measurements were carried out at the STM-lab of the Physical Chemistry with Focus on Catalysis Department of the Technische Universität München. The camber was equipped with a newly developed high-temperature STM based on the SPECS STM 150 Aarhus HT, similar to [9]. It achieves very low thermal drift by a special geometry of the sample holder, a highly stable radiative heater, and a large mass serving as heat sink, and can operate at temperatures of up to 1300 K. The base pressure was of 5×10^{-10} mbar.

Density functional theory calculations have been carried out using the VASP code. The Projector Augmented Wave (PAW) method was used to account for the core electrons, with the $6s$ and $5d$ electrons of Ru and the $2s$ and $2p$ electrons of C explicitly included in the valence. Single particle orbitals were expanded in plane-waves using a kinetic energy cut-off of 400 eV. Surfaces were modeled with the usual slab geometry, using either a (4×8) or a (4×10) supercell with 4 layers, of which the bottom two were kept frozen at the bulk interatomic distances. The vacuum was about 10.5 Å. In principle, $(1\,0\,\bar{1}\,0)$ surfaces posses two possible terminations: a long termination, where the distance between the first and second layer is $\sqrt{3}/2a$ (with a the lattice parameter), and a short termination,where the first interlayer distance is $\sqrt{3}/2a$. The relaxed substrate, both graphene covered or not, displays a lower overall energy if a short termination is used. Core level binding energies have been estimated within the final state approximation, where the screening from valence electrons is included, thus providing an accurate estimate of its effects on the core level binding energies. The method used in our work calculates the core level shifts with an accuracy better than 50 meV [12].

5.2 Finding the best growth conditions: HR-XPS and LEED

Several different CVD growth procedures were tested with the aim of obtaining large, single-crystal graphene domains on Ru(1 0 $\bar{1}$ 0). All different growth procedures have been characterized by LEED at the Surface Science Laboratory and by XPS at the SuperESCA beamline.

The growth procedure for graphene on Ru(0 0 0 1) [13] applied in Ch. 4 has been used as a starting point, because of the expected similarities involved in the surface reactivity when using C_2H_4 as a precursor, considering nonetheless that a different termination might give different results. Therefore, growth at a fixed temperature was tested: C_2H_4 was dosed at T =1020 K with a pressure of 2×10^{-8} mbar for 480 s, and then with a pressure of 5×10^{-8} mbar for and additional 480 s. In our case, LEED patterns obtained after growth

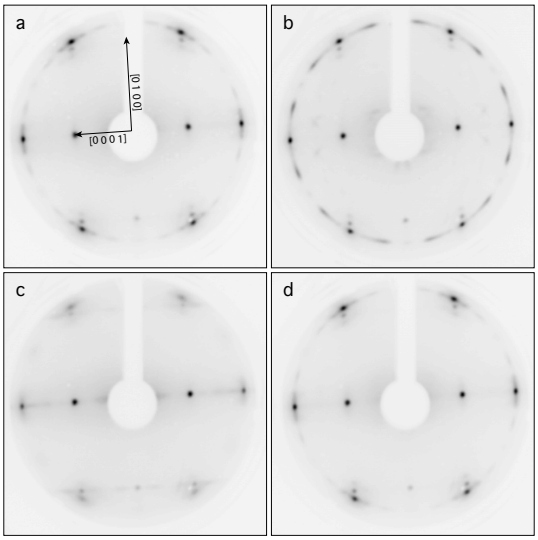

Figure 5.2: LEED images acquired at 75 eV after CVD growth at fixed temperatures. Several rotated graphene domains are visible for all growth conditions. (a) growth at $T = 1020$ K, initial pressure 2×10^{-8} mbar, (b) growth at $T = 1070$ K, initial pressure 2×10^{-8} mbar, (c) growth at $T = 970$ K, initial pressure 2×10^{-8} mbar, (d) growth at $T = 1020$ K, initial pressure 2×10^{-9} mbar

were compatible with the presence of graphene (see Fig. 5.2(a)). The main spots associated to graphene, referred to as R0, have one of the graphene reciprocal lattice vectors aligned with the [0 0 0 1] direction. However, no spots related to a moiré superstructure have been detected, and several satellite rotational domains are present, which indicate a large number of domains with a random rotation around the main R0 alignment. Growth at higher

temperatures ($T = 1070\,\mathrm{K}$, see Fig. 5.2(b)) gives increasingly higher intensity for the randomly rotated domains, while growth at lower temperature ($T = 970\,\mathrm{K}$, see Fig. 5.2(c)) does not improve the rotational domains, but gives much broader LEED spots, implying smaller graphene domains have been created. Growth at lower pressures ($P = 2 \times 10^{-9}$, see Fig. 5.2(d)) for longer times, with the same exposure of 30 L as in the previous cases, gives results very similar to growth following the procedure whose results are shown in Fig. 5.2(a).

The next approach that was tested was TPG growth, where ethylene is adsorbed at room temperature ($T = 300\,\mathrm{K}$, $P = 2 \times 10^{-9}\,\mathrm{mbar}$, up to saturation) on the sample that is subsequently annealed to 1020 K. The procedure is repeated in several cycles, while monitoring *in situ* the C 1*s* core level spectra exploiting the real time XPS capabilities of the SuperESCA experimental setup. In this way, information about the amount of C on the surface could be used to adjust the C_2H_4 pressure during the adsorption stage of each cycle in order to compensate for the decrease in free surface area that can catalyze the thermal decomposition of ethylene (maximum $P = 5 \times 10^{-8}\,\mathrm{mbar}$). To finalize the growth, and finish covering the surface with a full graphene layer, a final growth step is performed at fixed temperature by dosing ethylene at $T = 1200\,\mathrm{K}$, $P = 3 \times 10^{-7}\,\mathrm{mbar}$. Higher temperatures ($T = 1220\,\mathrm{K}$) resulted in a lowering of the C 1*s* signal from graphene, implying diffusion in the bulk. TPG growth was found to give a full graphene layer, that was the result of 5 growth cycles. This growth procedure consistently gives comparable results, independently of the annealing temperatures for the cycles following the first one, which were tested up to 1200 K.

The procedure necessary for the extraction of the C 1*s* spectrum is similar to the one in Ch. 4. In a first step, the clean surface Ru 3*d* spectrum is analyzed. Like for Ru$(0\,0\,0\,1)$, it is possible to discern 3 components in the Ru $3d_{5/2}$ spectrum: a bulk component, a surface component, and a second layer component (see Fig. 5.3(a)). The surface core level shifts were found to be compatible with values found in literature [14], and were $(-500 \pm 20)\,\mathrm{meV}$ for first layer atoms, $(-230 \pm 20)\,\mathrm{meV}$ for second layer atoms. It is crucial for this analysis that there is no oxygen contamination on the surface, since the surface components are extremely sensitive to the presence of oxygen [15]. The cleanliness is confirmed by a LEED pattern with no superlattice spots and with a low background (see Fig. 5.3(b)). As in Ch. 4, the C 1*s* spectrum is obtained after subtracting the Ru $3d_{3/2}$ peaks calculated after fitting the Ru $3d_{5/2}$ peaks. XPS spectra of the C 1*s* obtained in this way show 2 relatively wide components for all growth procedures (see Fig. 5.4(a)). As before, for an accurate description these C 1*s* spectra need DFT calculations for the core levels, but it is still possible to distinguish two separate C populations: a strongly interacting one with a peak at 284.8 eV, and a more weakly interacting one with a peak at 284.4 eV. From LEED, it is possible to determine that the only rotational domains are the R0 and the R30, which however have weak, large, and moiré free spots (see Fig. 5.4(b)). This implies domains with average size smaller that 150 Å are being created, although only with R0 and R30

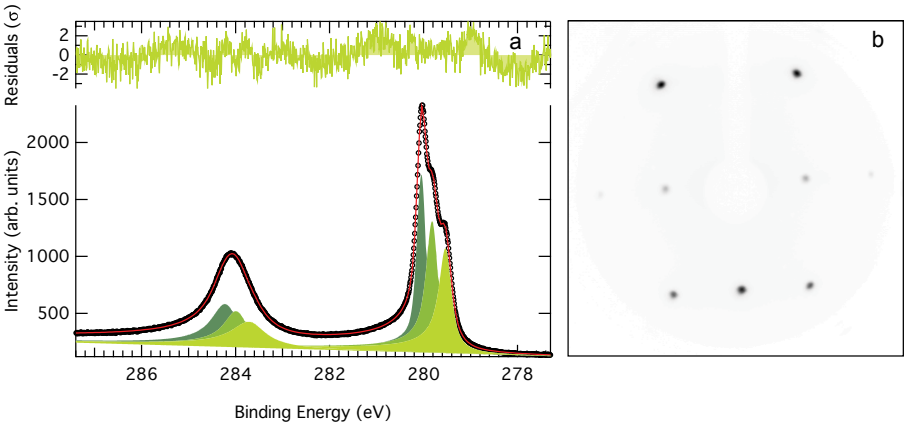

Figure 5.3: Characterization of the clean Ru(1 0 $\bar{1}$ 0) surface by HR-XPS (a) and LEED at 85 eV(b). The Ru $3d_{5/2}$ (lower BE) and Ru $3d_{3/2}$ (higher BE) spectra (black markers) are acquired simultaneously and fitted (blue line) as described in the text. The individual components have been plotted and are coded with different colors, according to [14]: the lightest green is assigned to the first layer atoms, the medium green to the second layer atoms, the darkest green to the bulk Ru. The normalized fitting residuals are plotted above.

orientation.

Finally, we tested annealing the graphene-covered surface to 1320 K for 30 s, at a temperature that is 100 K higher that the temperature where we observed C diffusing in the bulk. This final step induced changes detectable both in XPS and in LEED. The component generated by the less interacting atoms in the C 1*s* spectrum (see Fig. 5.4(c)) shows a higher relative intensity, as evidenced by the minimum which is now visible between the two peaks, and the integrated intensity is around half of that before the high temperature annealing. The LEED pattern again shows only R0 and R30 graphene rotational domains, but the size is now limited by the instrumental resolution. Spots associated to moiré superlattices are now evident, both for the R0 and for the R30, showing respectively (1×10) and c(4×8) periodicity in LEED (see Fig. 5.4(d), and Fig. 5.5(a,b)). This data implies that the heating process induces a partial dissolution of graphene in the Ru bulk, and cooling allows the C to segregate back to the surface, allowing the surviving domains to grow and undergo a ripening process.

In order to interpret the XPS spectra, DFT calculations have been performed for graphene on Ru(1 0 $\bar{1}$ 0) in the two main orientations: R0, with a (1×10) periodicity, and R30 with a c(4×8) periodicity. For both rotations, several adsorption sites have been tested, and the adsorption energies have been calculated. For the c(4×8) structure, all the tested adsorption sites relax to a bridge-top equivalent (where two carbon atoms are bridged on top of a

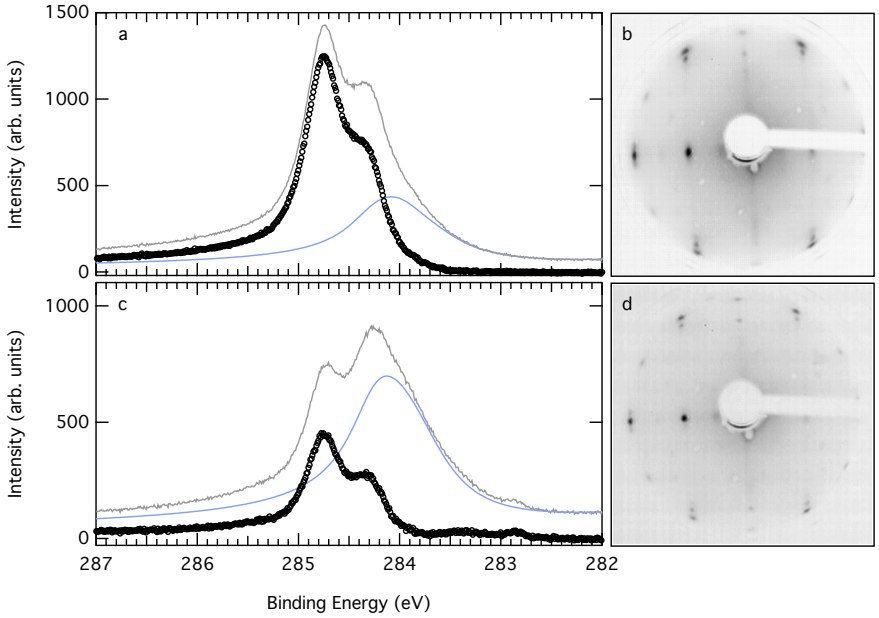

Figure 5.4: High resolution XPS spectra and LEED images for C 1*s* after TPG graphene growth (a,b) and after annealing to 1320 K for 30 s (c,d). The gray curves are the raw data, while the blue curves are the Ru $3d_{3/2}$ spectra inferred from the Ru $3d_{5/2}$ as described in the text. The black markers represent the C 1*s* spectra. LEED images are acquired at 79 eV at the SuperESCA beamline.

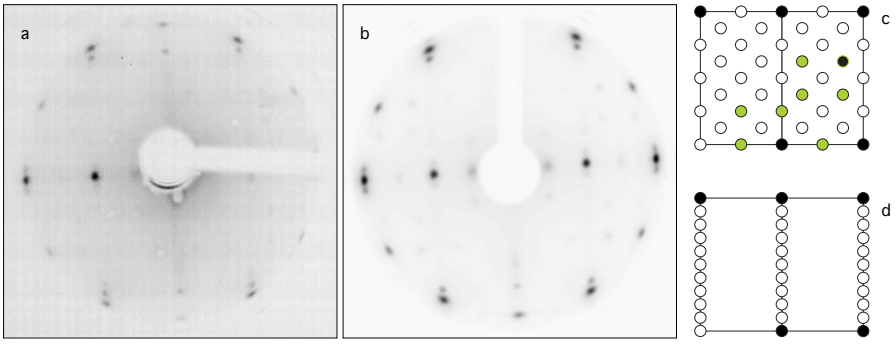

Figure 5.5: LEED images acquired for graphene grown by using the TPG technique, after annealing to 1320 K (a) at the SuperESCA beamline, (b) at the Surface Science Laboratory. In (b), it is possible to discern spots from the c(4×8) structure (green spots in (c)) and the (1×10) structure (d).

substrate atom in the center of the unit cell). In the case of the (1×10), it was found that two stable adsorption sites exist, that are almost degenerate in energy: a bridge-top (abbreviated $(1 \times 10)br$), where a carbon bridge is on top of a substrate atom on the border of the unit cell, and a hex-top (abbreviated $(1 \times 10)hex$), where a graphene hexagon is on top of a substrate atom on the border of the unit cell.

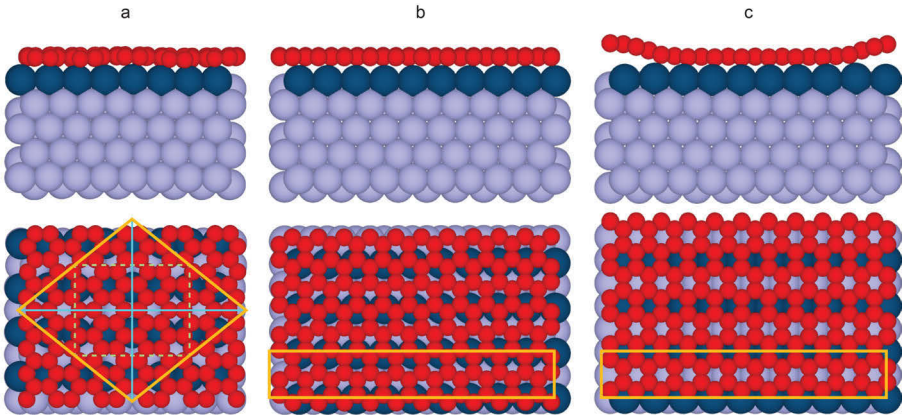

Figure 5.6: Relaxed supercells for the 3 stable structures as found by the DFT calculations. In (a), the c(4×8) structure. The $c2mm$ primitive unit cell is marked in yellow, with reflection lines marked in light blue and glide lines in dashed green. In (b) the true $(1 \times 10)br$ and in (c) the $(1 \times 10)hex$ have been simulated by including 4 substrate unit cells, one of which is marked with yellow rectangles.

The 3 relaxed structures are shown in Fig 5.6. The c(4×8) structure is two-fold symmetric, displays 2 orthogonal mirror symmetries and two orthogonal glide lines: it has a $c2mm$ symmetry. Regarding the (1×10) structures, one of them is wavy (see Fig. 5.6(c)), displaying a (1×10) moiré and a large one dimensional corrugation along the [0 0 0 1] direction (along the wide edges of the substrate rectangles). The other (1×10) structure does not display such a waviness (see Fig. 5.6(b)), even though the supercell has the same shape.

Calculations for the C 1s BEs have also been performed, allowing the characterization of the different growths by using the familiar combined XPS and DFT approach. However, things are complicated in this system by the fact that, for all growth procedures tested, there is always a mixture of at least two different structures. The most relevant data is that obtained after TPG growth and annealing to 1270 K, so that only R0 and R30 are present in large, well ordered domains.

We performed fits of the C 1s spectra for the TPG growth before (Fig. 5.7(a)) and after (Fig. 5.7(b)) annealing to high temperature. This was performed by using a weighed sum of the spectral distributions given by two of the stable structures found by DFT: the $(1 \times 10)hex$ and the c(4×8). The $(1 \times 10)br$ has a spectral distribution that does not agree with the data, and any efforts of

including it in the fit procedure result in no intensity for this structure. The

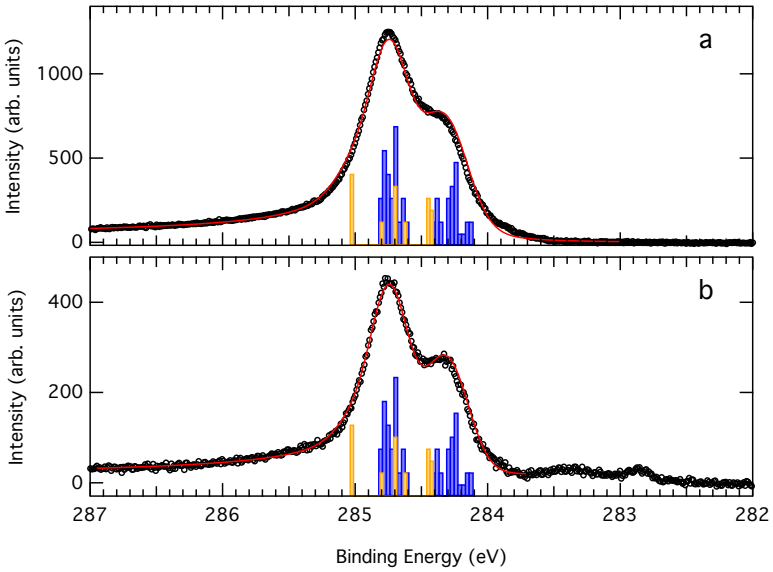

Figure 5.7: C 1*s* spectra (black markers) obtained with the procedure described in the text, fitted (red lines) with the DFT calculated C 1*s* BE distributions for the $(1 \times 10)hex$ structure (orange histogram) and the c(4×8) structure (blue histogram). In (a), after TPG growth, in (b), after annealing to 1320 K for 30 s.

absence of $(1 \times 10)br$ is plausible since the LEED pattern shows strong (1×10) diffraction spots, which are expected to be enhanced in the case of a wavy topology. The waves should enhance diffraction from the (1×10) supercell, as opposed to the sum of diffraction intensity from the separate lattices of graphene and the substrate. Furthermore, even though they are almost degenerate, the DFT calculations show that the $(1 \times 10)hex$ structure has a slightly better adsorption energy by 7 meV per C atom when compared to $(1 \times 10)br$.

The results of the fits show that, after TPG growth and before heating to high temperature, graphene is about 37% $(1 \times 10)hex$, 63% c(4×8). Following the annealing to 1270 K, graphene is about 18% $(1 \times 10)hex$, 82% c(4×8). The fits give good results for all individual TPG growths followed by annealing, although some variability in the relative amounts of the two structures after annealing to 1270 K indicates that there is some random component in the growth conditions when annealing to high temperature. For this reason, the dynamics of the growth were expected to play an important role.

5.3 LEEM and μ-LEED experiments

The anisotropy of the surface was expected to encourage some interesting growth dynamics for graphene. For this reason, LEEM measurements were carried out to gain a better understand the TPG growth process, with subsequent annealing. So, while following the growth procedure described in section 5.2, we performed bright-field LEEM measurements, where the contrast of the image is given by the intensity of the (0,0) spot.

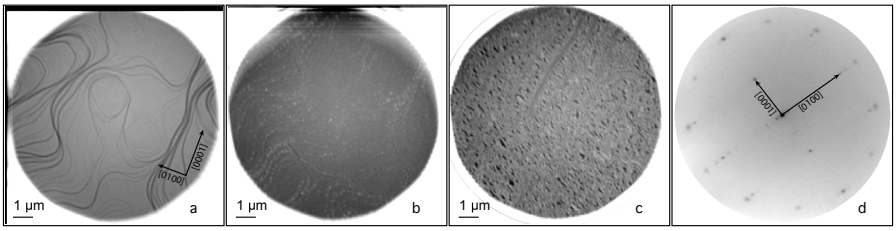

Figure 5.8: TPG growth as observed by LEEM at 5 eV. In (a) the clean Ru surface shows large single terraces, with most of the steps being localized in step bunches. In (b), the result of the first TPG cycle shows small graphene nucleation sites mostly at step edges. In (c), the final graphene covered surface after 5 TPG cycles, with corresponding LEED pattern at 41 eV(d). In (a) and (d), the lattice directions are shown for reference.

The results show that, during the first cycle of TPG growth (Fig. 5.8(b)), nucleation starts at step edges, and after 5 cycles the surface is almost completely covered by a full graphene layer (Fig. 5.8(c)), leaving about 7% of the Ru surface free. LEED images show that the R0 and R30 graphene rotations are the only ones present after the TPG procedure. However, the domains are very small, averaging around 85 Å as determined by LEED spot widths.

Next, we studied the second part of the TPG growth procedure that was optimized using XPS and LEED: we heated the sample to 1270 K. The LEEM movies show that, between 1220 K and 1290 K, the graphene layer starts disappearing as a result of diffusion of C in the bulk of the Ru crystal, starting from graphene at step edges (Fig. 5.9(a,b)). Holes appear in the graphene layer, and quickly grow to leave only small graphene islands. Some flakes, however, display moderate growth during this phase. At even hotter temperatures, just 25 K higher (Fig. 5.9(c)), the graphene layer quickly dissolves in the Ru bulk. Thanks to the real-time imaging capabilities of the LEEM technique, it was possible to interrupt heating when just a few small islands were left. Upon cooling to 1250 K (Fig. 5.9(d)), carbon segregates back to the surface, rapidly enlarging the small graphene islands that were left. Strongly anisotropic growth was observed, and needle-like structures were observed to develop.

This form of ripening for the small graphene domains gives very large single-crystal graphene flakes, of the order of several μm. Only R30 and R0 are left.

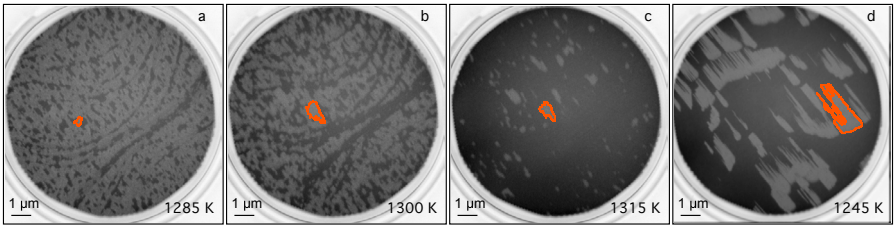

Figure 5.9: LEEM images (20 eV start voltage) of the high temperature annealing of the graphene layer obtained by TPG growth. In (a), at 1285 K, the graphene layer has already started to dissolve in the Ru bulk. In (b), at 1300 K, the process proceeds especially at step bunches. In (d), at 1315 K, the dissolution of C in the Ru crystal is much quicker, and if heating is interrupted when only small islands are left, a ripening process takes place (d) by surface segregation of the C that had previously dissolved in the bulk. Orange edges identify a single large graphene flake that can be seen to grow at first, up to 1300 K, but eventually starts dissolving as well. Upon cooling, it grows to several microns in size.

This type of growth from the bulk has been exploited on the Ru(0 0 0 1) surface, where growth of very high quality, 100 µm wide graphene crystals was observed after saturating the bulk with interstitial C [16]. In our case, we obtained a coverage slightly above 60% after growth from the bulk, with only 2 rotational domains for graphene.

These observations directly confirm the growth mechanism for graphene after annealing to high temperatures. They also explain why there was a some degree of variability in the graphene domains that are found after the annealing, since the percentage would strongly depend on which R0 or R30 domains are left after partial or complete dissolution of graphene in the Ru bulk. In the case of a prolonged 30 s annealing at high temperature, no graphene is expected to be left on the surface when segregation growth begins. If the heating is stopped before complete dissolution, very small differences in annealing time or temperature could lead to a very different statistical distributions for graphene R0 or R30 rotational domains on the surface. Several ripening cycles do not noticeably improve the surface quality, but further ethylene deposition at 1200 K after the high temperature annealing preserves the rotational domains and completely covers the surface in large graphene single crystals of the order of several µm in size. Dark-field LEEM confirms the surface is exclusively covered by R0 and R30 rotational domains of graphene, leaving however a significant portion of the Ru surface uncovered. We performed µ-LEED on the graphene layer obtained in this way, so that it was possible to individually measure the diffraction patterns for both the R0 and the R30 rotational domains, as shown in Fig. 5.10. Most of the surface was found to be covered by R0 graphene, in contrast to the growth performed at the SuperESCA beamline, likely as a result of the different dissolution protocol. The µ-LEED pattern generated by

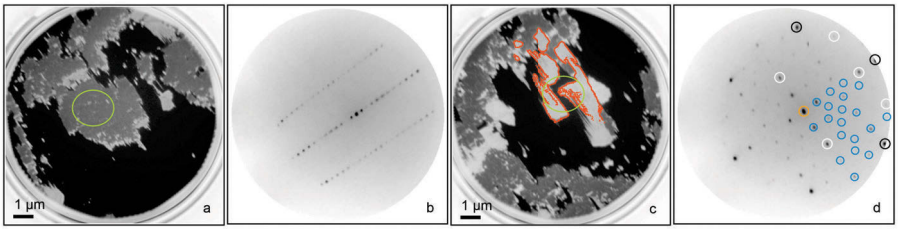

Figure 5.10: µ-LEED images for the R0 and R30 graphene rotational domains. In (a), a region that is exclusively covered by R0 rotated graphene (18 eV start voltage) as determined by dark-filed measurements. Black areas are generated by the bare Ru surface. A 2 µm field limiting aperture (green ellipse in (a)) was used for µ-LEED measurements at 40 eV (b). In (c), a region where some R30 graphene is present (18 eV start voltage). The orange contours outline R30 graphene, as determined from a dark-field image of the same region. The green ellipse marks the boundary of the field limiting aperture. In (d), the LEED at 40 eV from this region shows a structure compatible with the c(4×8) superstructure. White circles mark the substrate diffraction spots, black circles are from graphene, and blue spots are associated to the superstructure.

the R0 domains (Fig. 5.10(a,b)) allowed to unequivocally determine that the superstructure is the predicted (1×10), with all the diffraction orders being well visible. The same was possible for the R30 domains: the superstructure diffraction pattern was found to be compatible with a $c(4 \times 8)$ (Fig. 5.10(c,d)).

5.4 Characterization of the stable structures: STM measurements

In order to directly confirm the results of the DFT calculations, STM experiments were carried out. Graphene on Ru$(1\,0\,\bar{1}\,0)$ was successfully imaged at room temperature with atomic resolution, actually providing a direct proof that the approach used throughout this thesis, where DFT calculations are coupled to spectroscopic and diffraction experiments, is successful in correctly describing existing graphene based nanostructures. All the 3 types of stable domains predicted by DFT for the R0 and R30 graphene rotations were found to exist following the TPG growth procedure described in Section 5.2, followed by a flash annealing to 1300 K to promote ripening of the R0 and R30 domains. From the LEEM experiments, the surface was then expected to exhibit very large graphene single crystals, prevalently $(1 \times 10)hex$ and $c(4 \times 8)$.

Indeed, STM experiments revealed both these domain types, with the predicted structure. The $(1 \times 10)hex$ was found to exhibit one dimensional waves (see Fig. 5.11), and STM profiles indicate that the superstructure exhibits relatively flat troughs with a corrugation along the $[0\,0\,0\,1]$ direction that is about 10% of the corrugation along the $[0\,0\,1\,0]$ direction. This, however, is

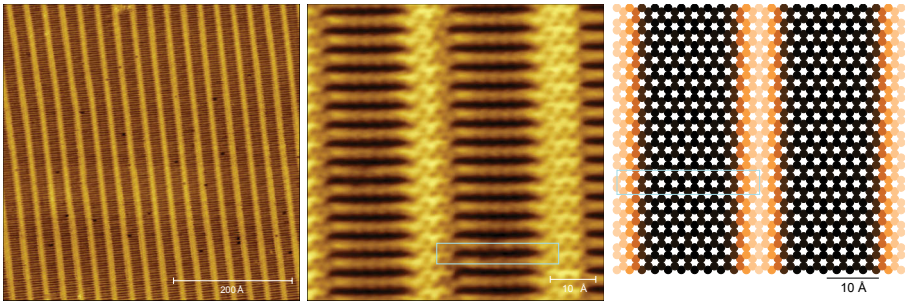

Figure 5.11: A (1×10)*hex* graphene flake imaged by STM. Imaging parameters are $I = 0.79\,\text{nA}$, $V = 57\,\text{mV}$ for the left image, $I = 0.18\,\text{nA}$, $V = 57\,\text{mV}$ for the middle image. On the right, the relaxed (1×10)*hex* graphene structure. The color scale represents the distance of each atom from the first substrate layer, with darker colors being closer. The blue rectangles mark the (1×10) supercell.

not the true topographic corrugation, because of the nature of STM images that always include the electronic density of states as a contribution to the tunneling current modulation. The corrugation ratio is likely closer to 5%, as deduced from the DFT calculations. In Fig. 5.11 (right), the height-color coded top view of the (1×10)*hex* structure obtained from the numerical calculations is shown. The DFT relaxed structures indicate that in the raised portions, C atoms are more than 3 Å away from the surface, and hexagonal features are visible in the crests of the moiré superstructure in the STM image, where an almost free standing graphene is present.

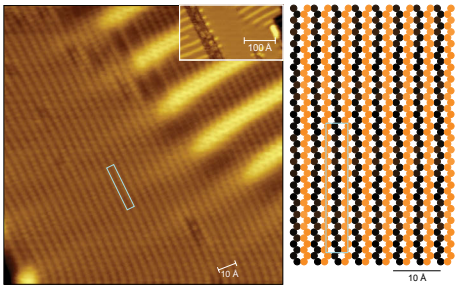

Figure 5.12: STM image of the flat (1×10) structure that can be identified as the (1×10)*br* (left). The inset shows the location of this flake, close to a graphene flake edge. Some patches of (1×10)*hex* and bare Ru surface are also visible in the image. Some defects can be seen at the boundary between (1×10)*br* and (1×10)*hex*. Imaging parameters are $I = 0.71\,\text{nA}$, $V = 51\,\text{mV}$ for the main image, $I = 0.08\,\text{nA}$, $V = 56\,\text{mV}$ for the inset. On the right, the relaxed (1×10)*hex* graphene structure. The color scale represents the distance of each atom from the first substrate layer, with darker colors being closer. The blue rectangles mark the (1×10) supercell.

Small patches of a flat (1×10) were also found (see Fig. 5.12), mainly in proximity of graphene flake edges. This structure was identified as a (1×10) because of the perfect matching between the visible lines in the image with the substrate lattice constant along the [0 0 0 1] direction. Also, a continuous deformation of the graphene lattice when passing from the $(1 \times 10)hex$ to the flat structures (Fig. 5.12, bottom half of the image) confirms this. In the upper half of the image, however, defects can be seen at the boundary between the $(1 \times 10)hex$ and the flat (1×10) structures.

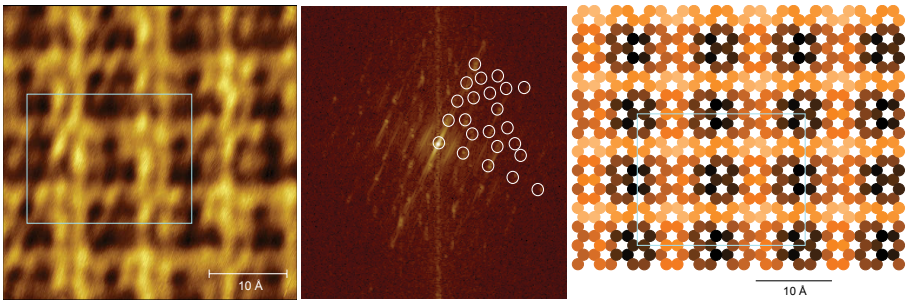

Figure 5.13: STM image of the c(4×8) structure (left). Imaging parameters are $I = 0.41\,\text{nA}$, $V = 56\,\text{mV}$. The Fourier transformed image is shown in the middle, with some spots circled in white, strongly resembling the LEED image in Fig. 5.10(d). On the right, the relaxed c(4×8) graphene structure. The color scale represents the distance of each atom from the first substrate layer, with darker colors being closer. The blue rectangles mark the c(4×8) supercell.

This is compatible with the flat structure being the $(1 \times 10)br$, which is shifted with respect to the $(1 \times 10)hex$ by half a graphene unit cell, and is the only other stable graphene phase found to exist on Ru(1 0 $\bar{1}$ 0) by the DFT calculations. Furthermore, there is a good qualitative agreement between the calculated C atom height above the substrate and the measured STM images (Fig. 5.12, right).

The STM images for the c(4×8) structure (Fig. 5.13, left) were found to have glide lines compatible with a $c2mm$ symmetry, resulting in a Fourier transformed image that matches the observed LEED pattern (Fig. 5.13, middle). Also in the case of the c(4×8) structure, the numerical calculations show a relatively flat arrangement. This time, it is possible to associate some tartan-like protruding features in the predicted topography (see Fig. 5.13, right) to similar features observed in the STM images.

5.5 Analysis of the simulated structures

Some interesting details can be understood by inspecting correlation diagrams of three quantities that can be obtained from the DFT calculations: the C 1s BEs, the average nearest neighbor (n. n.) distance, and the distance from the

surface. The C 1*s* BEs have been obtained from the calculated values and the fitting results of Section 5.2, and the distance of each C atom from the surface has been calculated as the distance from the average plane passing through first layer Ru atoms. The average value of the three n. n. distances for C atoms in graphene is an indicator of strain in the graphene lattice, and should be compared to the value in graphite (1.42 Å [17]), and in suspended free-standing graphene (1.4 Å [18]).

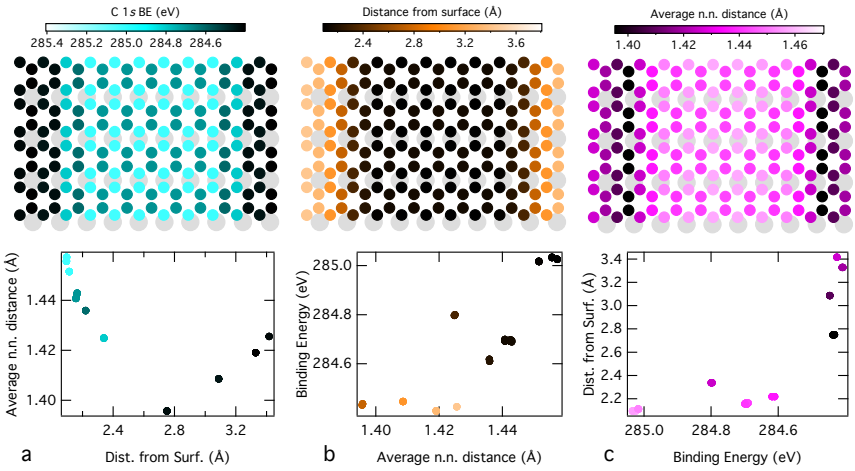

Figure 5.14: Analysis of the (1×10)*hex* structure as obtained from DFT. In (a), the color scale represents the C 1*s* BEs, and on the bottom, a correlation diagram shows the average n. n. distance *vs.* the distance from the surface of each C atom. In (b), the color scale represents the distance from the surface, and on the bottom, a correlation diagram shows the C 1*s* BEs *vs.* the average n. n. distance of each C atom. In (c), the color scale represents the average n. n. distance, and on the bottom, a correlation diagram shows the distance from the surface *vs.* the C 1*s* BEs. Gray circles represent first layer Ru atoms.

Regarding the (1×10)*hex* structure, it is possible to notice that the C 1*s* BEs (Fig. 5.14(a)) on the crest of the moiré waves is quite low, close to the value for decoupled graphene on lowly interacting transition metal surfaces such as Ir(1 1 1) (see Ch. 4). In the troughs, the BE is slightly higher when the C atoms are sitting close to a first layer substrate atom, creating horizontal lines along which the BE is slightly higher. Considering the dependence of the BE *vs.* the distance from the surface (Fig. 5.14(c)), it is possible to notice that, once a distance of 2.8 Å is reached, the BE stops decreasing, having reached a value of 284.4 eV, close to 284.2 eV that has been found for Gr/Ir/Ru(0 0 0 1) in Ch. 4. The average n. n. distance does not correlate well with neither the distance from the surface (Fig. 5.14(a)), nor with the BEs (Fig. 5.14(b)). This is likely due to the accumulation of compressive strain in intermediate-height

portions of the superstructure Fig. 5.14(c), so that the interaction with the substrate is the main factor that determines the properties of the individual C atoms.

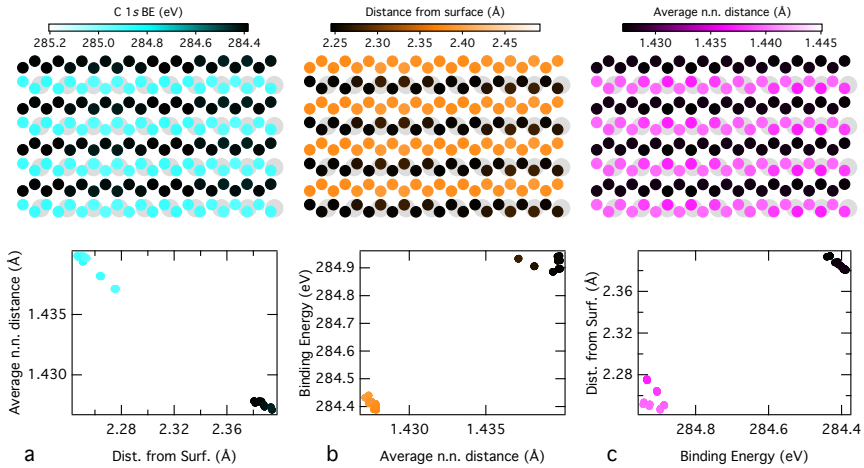

Figure 5.15: Analysis of the $(1 \times 10)br$ structure as obtained from DFT. In (a), the color scale represents the C 1*s* BEs, and on the bottom, a correlation diagram shows the average n. n. distance *vs.* the distance from the surface of each C atom. In (b), the color scale represents the distance from the surface, and on the bottom, a correlation diagram shows the C 1*s* BEs *vs.* the average n. n. distance of each C atom. In (c), the color scale represents the average n. n. distance, and on the bottom, a correlation diagram shows the distance from the surface *vs.* the C 1*s* BEs. Gray circles represent first layer Ru atoms.

Considering the flat $(1 \times 10)br$ structure, it is possible to divide the carbon atoms in 2 families according to the DFT calculations, even though the surface is seemingly flat. The graphene layer, in fact, has two different "zig-zag" lines along the [0 0 1 0] direction: one on top of first layer Ru atoms, another on top of second layer atoms. The correlation diagrams in Fig. 5.15 show a clear splitting of the C atom population, revealing that coincidence with the first layer atoms causes a much stronger interaction (as seen in the BE, Fig. 5.15(a)), and also a slightly smaller (by 0.13 Å) distance from the surface (Fig. 5.15(b)), so that "zig-zag" lines above a second layer Ru atom are slightly protruding. There is also a small amount of compressive strain for those atoms on protruding rows (Fig. 5.15(c)).

We finally consider the c(4×8) structure. The correlation diagrams give some interesting insight regarding the nature of the splitting in BEs that gives rise to two distinct peaks in XPS C 1*s* spectra. In fact, although the surface is almost flat, the plots always show two separate point clouds (Fig. 5.16), indicating two that also in this case there are two distinct families, one with

a C 1*s* BE of 284.9 eV, and one with a BE of 284.4 eV, more typical of free standing graphene. Again, the coincidence with first layer Ru atoms seems to play an important role in the splitting, which is also evident in the case of the average n. n. distance (Fig. 5.16(c)). The distance from the surface, however,

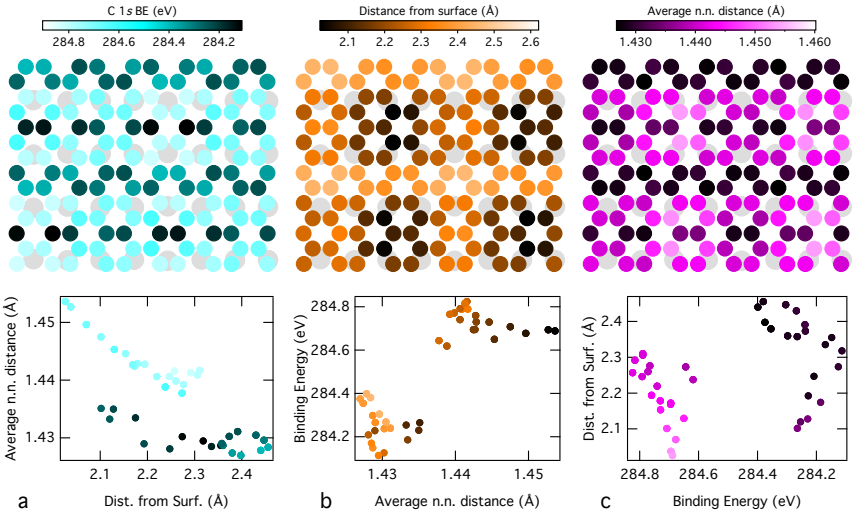

Figure 5.16: Analysis of the c(4×8) structure as obtained from DFT. In (a), the color scale represents the C 1*s* BEs, and on the bottom, a correlation diagram shows the average n. n. distance *vs.* the distance from the surface of each C atom. In (b), the color scale represents the distance from the surface, and on the bottom, a correlation diagram shows the C 1*s* BEs *vs.* the average n. n. distance of each C atom. In (c), the color scale represents the average n. n. distance, and on the bottom, a correlation diagram shows the distance from the surface *vs.* the C 1*s* BEs. Gray circles represent first layer Ru atoms.

does not seem to be correlated with either the C 1*s* BE or with the strain (Fig. 5.16(a,c)), resulting in a topography that does not reveal the first layer Ru atom rows (Fig. 5.16(b)). This is also evident in the STM images of this structure (Fig. 5.13), where lines that might resemble Ru atomic rows, like in Fig. 5.12, are actually in the perpendicular direction.

5.6 Discussion: growth of carbon nanocombs

It was found that, during carbon segregation from the bulk, the anisotropy of the substrate has a profound influence on graphene growth dynamics. Although the ripening of both the R0 and R30 domains was observed to be strongly driven by the substrate direction, the R30 domains exhibited a unique comb-like growth mode. These needle-like structures propagate from the initial flake

across the substrate's atomic steps, like in the case of the rolling-carpet growth mode on Ru(0 0 0 1) [16], and quickly reach µm lengths. They are, in all effect, self assembled graphene nanoribbons. This is a completely new approach for the growth of such nanoribbons, requiring no large molecular precursor, only dissolved carbon from the Ru(1 0 $\bar{1}$ 0) bulk. This growth mode for graphene nanoribbons is completely determined by the substrate anisotropy and by the peculiar dynamics observed.

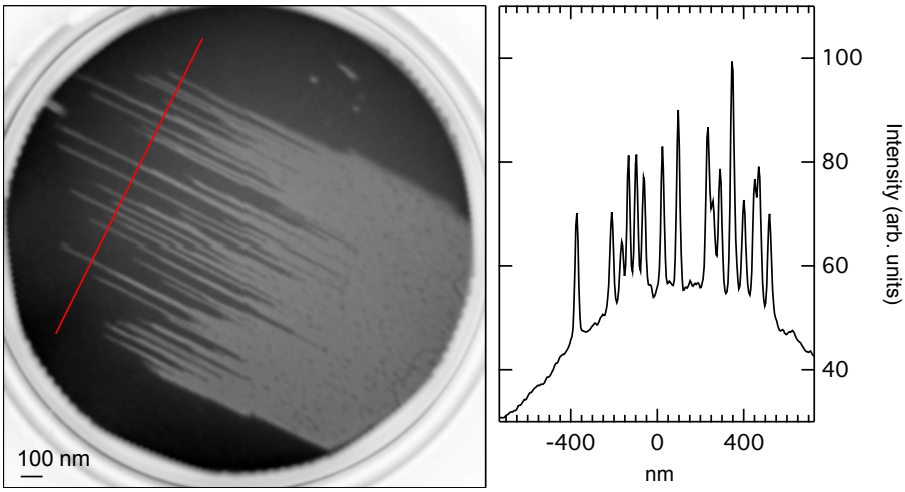

Figure 5.17: A LEEM image (20 eV start voltage) of one of the comb-like structures that grows after annealing the TPG graphene to high temperature (left). On the right, a line profile taken along the [0 0 0 1] direction reveals that the graphene nanoribbons are less than 17 nm wide.

The nanoribbons were observed to have a width of 17 nm (see Fig. 5.17), which is close to the lateral resolution of LEEM. When graphene nanoribbons start becoming this thin, theoretical calculations have predicted that a bandgap in the electronic structure should emerge [19], its value easily tunable by changing the nanoribbon's width or termination. However, it has also been found that edge roughness completely destroys the nanoribbon band structure, so that precise edge terminations are essential for electronic structure integrity. Strangely, the graphene nanoribbon phase has proven to be one of the more stable phases upon heating, despite the large perimeter to area ratio of these digitated structures. This may also mean the graphene nanoribbons obtained in this way possess exceptionally smooth and defect-free edges, which would explain the higher diffusion barrier for carbon atoms from the graphene nanoribbon edges to the Ru bulk: defects tend to lower the diffusion barrier of C atoms from graphene to highly interacting transition metals, as in the case of Re [20]. If defects were present, the diffusion barrier to the bulk would likely be lower than the flat (1×10) and c(4×8) structures. This approach therefore is likely

to yield graphene nanoribbons with a high level of edge perfection.

5.7 Discussion: transition between wavy and flat graphene

Another interesting phenomenon was observed in this rich system: once formed after TPG growth and further annealing to high temperature, the R0 domains appear to change contrast upon cooling. They break up in small patches, and abruptly change from bright to dark when observing the bright-field LEEM images (see Fig. 5.18(a,b)). This was previously observed in LEEM for graphene grown on Ir(0 0 1) [2], where it was demonstrated to be a transition between a wavy and a flat phase. We think this is the case also for this observed transition. In fact, as has been discussed, there are two stable structures for the R0 rotation of graphene, one wavy and one flat, which are almost degenerate in energy (only 7 meV per atom of adsorption energy difference). Furthermore, μ-LEED measurements of the (1×10) structure at high temperature (see Fig. 5.18(c)) show a significantly damped moiré, an indication that the wavy structure is absent. This transition is reversible, with bright patches that first appear when

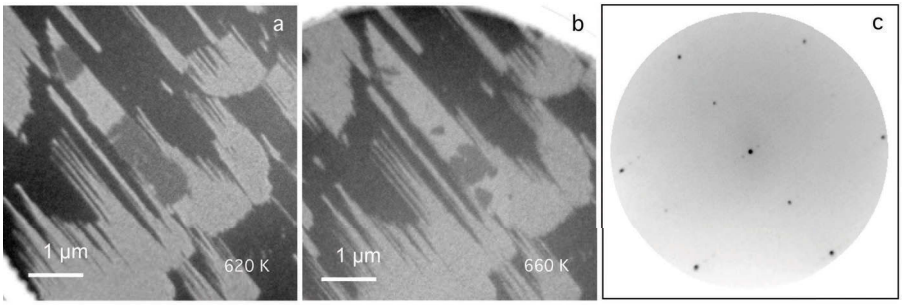

Figure 5.18: LEEM images (18 eV start voltage) of graphene flake undergoes the phase transition upon heating, from (a), where a large (1×10) flake is mostly dark colored at 620 K, to (b), where most of it has undergone the phase transition at 660 K. In (c), a LEED image at 40 eV acquired at 1000 K, with a field limiting aperture centered on a flake that has undergone the phase transition.

heating above 700 K, and almost complete conversion at 900 K. Cycling back and forth gives comparable results. It was found, however, that the patches that undergo the phase transition break up and become smaller at every cycle, with thin boundaries that appear between them. This is consistent with our hypothesis, since in order to go from one adsorption site (hex) to the other (bridge), there has to be a shift of the whole graphene sheet by half a lattice constant. This is energetically very costly, the energy cost rising with area that undergoes the transition. Cracks can form in the graphene crystal rendering less energetically expensive the process. It is possible that this phase transition

is strain driven, as in Ir(0 0 1) [2], since, upon cooling, graphene expands, while the substrate contracts.

5.8 Conclusions

We demonstrated graphene growth on a novel substrate, which resulted in some unpredicted behavior, mainly driven by the growth dynamics of graphene segregating from the bulk on the anisotropic Ru(1 0 $\bar{1}$ 0) surface. The growth conditions were optimized for having the greatest $(1 \times 10)hex$ graphene superstructure density with respect to other domains. It was found that this particular superstructure displays one dimensional waves, all with the same orientation, and with an exceptionally regular trough topology, rendering this the perfect platform for developing new one dimensional metal nanostructures. Furthermore, we observed two novel phenomena: the spontaneous substrate driven growth of graphene nanoribbons, and a reversible temperature-driven phase transition between a wavy and a flat graphene structure.

The nanoribbon growth we observed is of interest for several reasons. In fact, one of the main concerns with graphene has been to induce a band gap in this otherwise degenerate (0-gap) semiconductor, and graphene nanoribbons have attracted attention as a possible means of exploiting graphene in device fabrication and in the semiconductor industry. Graphene nanoribbons are expected to be a very efficient tool for bang gap engineering: as has been demonstrated both theoretically [19] and experimentally [21], by changing the width and specific termination of the graphene nanoribbons it is possible to manipulate their electronic structure and to obtain different band gap energies. This approach has proven itself as a powerful technique for graphene based transistors, raising the prospect of a new class of nanoelectronic devices that may have many advantages over existing technologies, for instance having excellent switching speeds or high carrier mobility even when carrier densities are low [22], and even ballistic transport at relatively high temperatures [23, 24]. Existing techniques for the formation of graphene nanoribbons include exfoliation [21], chemical approaches [25], unzipping of carbon nanotubes [26] and lithographic patterning of graphene sheets [27]. However, edge roughness of the ribbons, which destroys the quantum confinement and edge effects thanks to which graphene nanoribbons display semiconducting properties [23], is a major issue with all these methods. Also, the presence of defects and covalent functionalization can compromise the band structure of graphene nanoribbons [28]. Highly perfect graphene nanoribbons can be grown by using specific molecular precursors and dehalogenation, but the lengths are limited to a few tens of nm [29]. By using CVD with a simple precursor, C_2H_4, on the anisotropic Ru(1 0 $\bar{1}$ 0) surface, we successfully obtained µm long, less than 20 nm wide graphene nanoribbons.

This investigation can therefore be a starting point for several experiments: graphene on Ru(1 0 $\bar{1}$ 0) has proven to be an unexpectedly rich system, and, due to the fortuitous matching with the graphene lattice constant in the [0 0 0 1]

direction, it seems like an ideal candidate for the exploration of new graphene based nanostructures.

References

[1] Nilsson, L.; Andersen, M.; Bjerre, J.; Balog, R.; Hammer, B.; Hornekær, L.; Stensgaard, I. Preservation of the Pt(1 0 0) surface reconstruction after growth of a continuous layer of graphene. *Surface Science* **2012**, *606*, 464.

[2] Locatelli, A.; Wang, C.; Africh, C.; Stojić, N.; Menteş, T. O.; Comelli, G.; Binggeli, N. Temperature-Driven Reversible Rippling and Bonding of a Graphene Superlattice. *ACS Nano* **2013**, *7*, 6955.

[3] Wofford, J. M.; Nie, S.; McCarty, K. F.; Bartelt, N. C.; Dubon, O. D. Graphene Islands on Cu Foils: The Interplay between Shape, Orientation, and Defects. *Nano Letters* **2010**, *10*, 4890.

[4] Walter, A. L.; Nie, S.; Bostwick, A.; Kim, K. S.; Moreschini, L.; Chang, Y. J.; Innocenti, D.; Horn, K.; McCarty, K. F.; Rotenberg, E. Electronic structure of graphene on single-crystal copper substrates. *Physical Review B* **2011**, *84*, 195443.

[5] Rasool, H. I.; Song, E. B.; Mecklenburg, M.; Regan, B. C.; Wang, K. L.; Weiller, B. H.; Gimzewski, J. K. Atomic-Scale Characterization of Graphene Grown on Copper (1 0 0) Single Crystals. *Journal of the American Chemical Society* **2011**, *133*, 12536.

[6] Vinogradov, N. A.; Zakharov, A. A.; Kocevski, V.; Rusz, J.; Simonov, K. A.; Eriksson, O.; Mikkelsen, A.; Lundgren, E.; Vinogradov, A. S.; Mårtensson, N.; Preobrajenski, A. B. Formation and Structure of Graphene Waves on Fe(1 1 0). *Physical Review Letters* **2012**, *109*, 026101.

[7] Casarin, B.; Cian, A.; Feng, Z.; Monachino, E.; Randi, F.; Zamborlini, G.; Zonno, M.; Miniussi, E.; Lacovig, P.; Lizzit, S.; Baraldi, A. The Thinnest Carpet on the Smallest Staircase: The Growth of Graphene on Rh(5 3 3). *The Journal of Physical Chemistry C* **2014**, *118*, 6242.

[8] N'Diaye, A. T.; Gerber, T.; Busse, C.; Mysliveček, J.; Coraux, J.; Michely, T. A versatile fabrication method for cluster superlattices. *New Journal of Physics* **2009**, *11*, 103045.

[9] Günther, S.; Dänhardt, S.; Wang, B.; Bocquet, M.-L.; Schmitt, S.; Wintterlin, J. Single Terrace Growth of Graphene on a Metal Surface. *Nano Letters* **2011**, *11*, 1895.

[10] Over, H.; Bludau, H.; Skottke-Klein, M.; Ertl, G.; Moritz, W.; Campbell, C. T. Coverage dependence of adsorption-site geometry in the Cs/Ru(0 0 0 1) system: A low-energy electron-diffraction analysis. *Physical Review B* **1992**, *45*, 8638.

[11] Schmidt, T.; Heun, S.; Slezak, J.; Diaz, J.; Prince, K. C.; Lilienkamp, G.; Bauer, E. SPELEEM: Combining LEEM and Spectroscopic Imaging. *Surface Review and Letters* **1998**, *05*, 1287.

[12] Köhler, L.; Kresse, G. Density functional study of CO on Rh(1 1 1). *Physical Review B* **2004**, *70*, 165405.

[13] Alfè, D.; Pozzo, M.; Miniussi, E.; Günther, S.; Lacovig, P.; Lizzit, S.; Larciprete, R.; Burgos, B. S.; Menteş, T. O.; Locatelli, A.; Baraldi, A. Fine tuning of graphene-metal adhesion by surface alloying. *Scientific Reports* **2013**, *3*, 2430.

[14] Baraldi, A.; Lizzit, S.; Comelli, G.; Goldoni, A.; Hofmann, P.; Paolucci, G. Core-level subsurface shifted component in a 4*d* transition metal: Ru(1 0 $\bar{1}$ 0). *Physical Review B* **2000**, *61*, 4534.

[15] Baraldi, A.; Lizzit, S.; Paolucci, G. Identification of atomic adsorption site by means of high-resolution photoemission surface core-level shift: oxygen on Ru(1 0 $\bar{1}$ 0). *Surface Science* **2000**, *457*, L354.

[16] Sutter, P. W.; Flege, J.-I.; Sutter, E. A. Epitaxial graphene on ruthenium. *Nature Materials* **2008**, *7*, 406.

[17] Lipson, H.; Stokes, A. R. The Structure of Graphite. *Proceedings of the Royal Society of London A: Mathematical, Physical and Engineering Sciences* **1942**, *181*, 101.

[18] Gass, M. H.; Bangert, U.; Bleloch, A. L.; Wang, P.; Nair, R. R.; K., G. Free-standing graphene at atomic resolution. *Nature Nanotechnology* **2008**, *3*, 676.

[19] Son, Y.-W.; Cohen, M. L.; Louie, S. G. Energy Gaps in Graphene Nanoribbons. *Physical Review Letters* **2006**, *97*, 216803.

[20] Miniussi, E.; Pozzo, M.; Baraldi, A.; Vesselli, E.; Zhan, R. R.; Comelli, G.; Menteş, T. O.; Niño, M. A.; Locatelli, A.; Lizzit, S.; Alfè, D. Thermal Stability of Corrugated Epitaxial Graphene Grown on Re(0 0 0 1). *Physical Review Letters* **2011**, *106*, 216101.

[21] Li, X.; Wang, X.; Zhang, L.; Lee, S.; Dai, H. Chemically Derived, Ultrasmooth Graphene Nanoribbon Semiconductors. *Science* **2008**, *319*, 1229.

[22] Geim, A. K. Graphene: Status and Prospects. *Science* **2009**, *324*, 1530.

[23] Areshkin, D. A.; Gunlycke, D.; White, C. T. Ballistic Transport in Graphene Nanostrips in the Presence of Disorder: Importance of Edge Effects. *Nano Letters* **2007**, *7*, 204.

[24] Liang, G.; Neophytou, N.; Nikonov, D. E.; Lundstrom, M. S. Performance Projections for Ballistic Graphene Nanoribbon Field-Effect Transistors. *IEEE Transactions on Electron Devices* **2007**, *54*, 677.

[25] Yu, A.; Ramesh, P.; Itkis, M. E.; Bekyarova, E.; Haddon, R. C. Graphite Nanoplatelet–Epoxy Composite Thermal Interface Materials. *The Journal of Physical Chemistry C* **2007**, *111*, 7565.

[26] Kosynkin, D. V.; Higginbotham, A. L.; Sinitskii, A.; Lomeda, J. R.; Dimiev, A.; Price, B. K.; Tour, J. M. Longitudinal unzipping of carbon nanotubes to form graphene nanoribbons. *Nature* **2009**, *458*, 872.

[27] Han, M. Y.; Özyilmaz, B.; Zhang, Y.; Kim, P. Energy Band-Gap Engineering of Graphene Nanoribbons. *Physical Review Letters* **2007**, *98*, 206805.

[28] Mucciolo, E. R.; Castro Neto, A. H.; Lewenkopf, C. H. Conductance quantization and transport gaps in disordered graphene nanoribbons. *Physical Review B* **2009**, *79*, 075407.

[29] Cai, J.; Ruffieux, P.; Jaafar, R.; Bieri, M.; Braun, T.; Blankenburg, S.; Muoth, M.; Seitsonen, A. P.; Saleh, M.; Feng, X.; Müllen, K.; Fasel, R. Atomically precise bottom-up fabrication of graphene nanoribbons. *Nature* **2010**, *466*, 470.

Chapter 6

Molecular lifting, twisting, and curling in the path to carbon nanodomes

Once again, our research lead us to the study of graphene-based nanostructures, likely as a result of the versatility that such systems display in their capacity of tuning or changing the properties of the raw graphene material, or even exhibiting completely new and exotic behaviors. Specifically, we finally started considering true nanostructures and their synthesis, in the sense of graphene-based materials that are nanometer-sized in all three dimensions. The electronic properties of graphene, in fact, are completely changed when confined to nanometer-sized objects, where the quantum nature of the Bloch electrons starts "feeling" edges in every direction. At the same time, when sizes become so small, the precision of these structures is vital, as even small changes strongly affect the electronic structure of the system. The band gap problem in graphene can be overcome by exploiting quantum confinement effects, which allow the modification of the band gap by adjusting the width and the type of edge terminations [1–6].

Large polycyclic aromatic hydrocarbons (PAHs) molecules, which are constituted by multiple peri-fused aromatic rings, are an interesting starting point. In fact, they strongly resemble graphene in structure to begin with, and small changes can be made to obtain a wide range of graphene-based nanostructures. For these reasons, the process of surface-assisted cyclodehydrogenation of PAHs has been adopted in the recent years as one of the most effective, versatile, and flexible strategies for the bottom-up synthesis of fullerenes [7], small graphene flakes (nanographene), and nanoribbons [8–10]. The large number of available precursors is the key to tailor the structural properties of low-dimensional car-

bon networks via polymerization reactions and to control their chemical and transport properties, which exhibit promising properties for applications in opto- and molecular-electronics.

However, the pathway of molecular dissociation becomes more complex with increasing molecular extension, number of sequential reaction steps, degrees of freedom for molecular motion, and competition with desorption processes. The initial-state PAH adsorption configuration, which can be influenced by inter-molecular or substrate-mediated interactions, can also strongly affect the dissociation mechanism. For example, the reported thermally induced dehydrogenation of polyphenylene molecules on Cu(1 1 1) [11] proceeds via six intermediate steps of aryl-aryl coupling reactions. For polyphenylene molecules, the partial dehydrogenation of the large hydrocarbons leads to a H terminated nanographene, although in this case, the interaction with the substrate plays only a marginal role, and the partial reaction barriers are similar for the non-catalyzed dehydrogenation. It is clear that detailed knowledge of the chemical, structural, and electronic transformations involved in each cyclodehydrogenation step is a prerogative for finding more efficient routes to fabricate novel nanographene/nanoribbon structures with tailored properties.

In this study we show that thermally assisted cyclodehydrogenation of coronene ($C_{24}H_{12}$) on Ir(1 1 1) takes place through sequential steps that include dramatic changes of the molecule's pristine configuration. For a comprehensive characterization of the reaction process we adopted the familiar combined theoretical and experimental approach where density functional theory (DFT) calculations complemented the experiments performed combining several techniques, namely fast and high-energy resolution X-ray photoelectron spectroscopy (HR-XPS), near-edge X-ray absorption fine structure (NEXAFS), ultraviolet photoelectron spectroscopy (UPS), angle resolved photoemission spectroscopy (ARPES), temperature programmed desorption (TPD), and low energy electron diffraction (LEED). Once again, the approach gave unprecedented insight in a complicated process.

6.1 Methods

The Ir(1 1 1) single crystal used in this experiment was cleaned in ultra high vacuum (UHV) conditions by following the procedures outlined in Ch. 2, which was optimized to ensure a high quality surface, as judged by LEED and XPS. The measurements reported in this work were performed in UHV condition with a base pressure of the order of 1×10^{-10} mbar.

Commercially available (Sigma-Aldrich) coronene powder (99%, purified by sublimation) was used throughout the experiment. Coronene molecules were evaporated in vacuum using a custom evaporator consisting in a Boron Nitride (BN) crucible wrapped with a 1 mm diameter Ta wire used to heat it by resistive dissipation. The crucible was cleaned in vacuum before the experiment by means of a long annealing to increasing temperatures up to 670 K, in order to clean

the evaporation cell from impurities. The temperature inside the crucible was measured trough a type K thermocouple in thermal contact with the coronene powder. Coronene evaporation was achieved by keeping the crucible at a fixed temperature, varying from 400 to 440 K. Before evaporation, coronene was further purified in vacuum by means of repeated short annealing cycles up to 450 K, while monitoring the chamber residual gas composition with a Residual Gas Analyzer system. Calibration of the coronene evaporation rate was achieved by comparing the photoelectron intensity to a reference signal acquired with the same acquisition parameters, after graphene growth on Ir(1 1 1). On the basis of the C(10×10)/Ir(9×9) moiré unit cell, observed for single layer graphene on Ir(1 1 1), the reference coverage was assumed to be 2.47 ML.

High resolution (HR) and temperature programmed (TP) XPS [12] measurements were carried out at the SuperESCA beamline. C 1s spectra were acquired in normal emission geometry with a photon energy of 400 eV, along with a measurement of the Fermi level on the sample, which was used to align the binding energy scale. In order to check for possible X-ray induced molecular break-up we performed several scans along the surface to search for C 1s spectral modifications, without finding appreciable differences.

NEXAFS measurements were performed at the SuperESCA beamline of Elettra. Carbon K-edge absorption spectra were acquired in the Auger Electron Yield configuration, with a photoelectron kinetic energy of 260 eV and a photon energy range between 280 eV and 315 eV. Two different angular configuration were used, corresponding to an incidence angle of 0° and 70° with respect to the surface.

Valence band photoemission spectra were acquired at the BaDElPh beamline of Elettra using a state-of-the-art SPECS PHOIBOS 150 hemispherical analyzer combined with a 2D detector consisting of a phosphor screen coupled with a 2D-CCD commercial detector. The UPS spectra were measured with photon energy equal to 34 eV in a ±13° wide angular region centered in the K point of the reciprocal space. The ARPES maps were also acquired with 34 eV photon energy.

The LEED experiments were carried out at the Surface Science Laboratory at Elettra using a VG rear-view electron optical system. The TPD curves were also acquired at the Surface Science Laboratory at Elettra using an SRS 200 residual gas analyzer. During the experiment the sample was annealed at a fixed rate of 2.5 K/s by means of three hot W filaments placed a few millimeters behind the sample.

The C 1s spectra were analyzed using a sum of 24 Doniach-Šunjić functions [13] convoluted with Gaussians, including a Shirley type background. The relative BE shifts between the components were constrained to the ones predicted by DFT, while a rigid shift was imposed to align the experimental BE scale to the theoretical one. The Lorentzian and Gaussian widths, as well as the asymmetry parameters, were constrained to be the same for all peaks. This implicates the following assumptions: the core electronic states corresponding to the different C atoms in the molecule have the same finite lifetime (resulting

in an equal Lorentzian broadening); all the core level components are affected to the same extent by thermal phonon broadening, experimental, and inhomogeneous broadening (which are reflected in their Gaussian FWHM); the chance of electron-hole pair excitation events is the same for each core level (resulting in an equal asymmetry parameter). The intensities were also constrained to be equal. All experimental data and fitting results have been displayed after subtracting the background found by the fitting operation.

Density functional theory calculations have been carried out using the VASP code. The Projector Augmented Wave (PAW) method was used to account for the core electrons, with the $6s$ and $5d$ electrons of Ir and the $2s$ and $2p$ electrons of C explicitly included in the valence. Single particle orbitals were expanded in plane-waves using a kinetic energy cut-off of 400 eV. Surfaces were modeled with the usual slab geometry, using a (9 x 9) supercell with 4 layers, of which the bottom two were kept frozen at the bulk interatomic distances. The vacuum was ~ 17.5 Å for the clean surface and ~ 15 Å for the system with the coronene molecule adsorbed on the surface. We used the Gamma point only to sample the Brillouin zone. Energy barrier were estimated with the climbing-image Nudged Elastic Band method [14], using up to 11 images. Core level binding energies have been estimated within the final state approximation, where the screening from valence electrons is included, thus providing an accurate estimate of its effects on the core level binding energies. According to previous theoretical studies [15], the method used in our work calculates the core level shifts with an accuracy better than 50 meV.

6.2 Results and Discussion

Coronene was adsorbed on the surface at room temperature ($T = 300$ K). First, we performed NEXAFS measurements to address the issue of intact adsorbed molecule orientation with respect to the surface plane. Figure 6.1(a) reports the C K-edge absorption spectra measured at two different incident angles for sub-monolayer coverage. The most noticeable result is the strongly reduced intensity of the π^* resonance components at 286 eV when the electric field vector is almost parallel to the surface (normal incidence, NI), originating from the C $1s \rightarrow$ LUMO electronic transitions [16], and the increased spectral weight at about 292 eV due to the transition to the σ^* orbitals, thus indicating a nearly flat adsorption geometry. The presence of a shoulder extending up to about 288 eV can be explained, beside the C $1s \rightarrow$ LUMO+1, +2, +3 and +4 π^* transitions, as due to the interaction of the molecules with the substrate.

The strong modification in the electronic structure of coronene upon adsorption is confirmed by the UPS results reported in Fig. 6.1(b). These valence band (VB) spectra have been measured at normal emission ($h\nu = 34$ eV) after different surface preparations. The spectrum acquired after deposition of a monolayer of coronene on clean Ir(1 1 1) (1-red), shows several peaks attributed to molecular signals, since they appear at different binding energies with respect

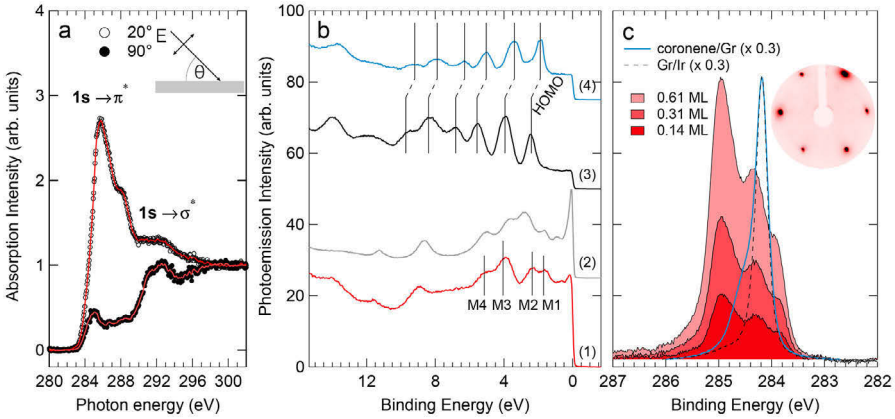

Figure 6.1: (a) C K-edge NEXAFS spectra for coronene/Ir(1 1 1) acquired with linearly polarized radiation, with the electric field vector either parallel (filled circles) or almost normal (open circles) to the crystal surface. (b) Valence band spectra measured at $h\nu = 34\,\text{eV}$ of (1-red curve) monolayer coronene on Ir(1 1 1), (2-gray curve) clean Ir(1 1 1), (3-black) multilayer coronene on Ir(1 1 1) and (4-blue) monolayer coronene on graphene/Ir(1 1 1). Identified molecular orbitals are, right to left (black bars on spectra (3), (4)): E_{2u} first peak; B_{1g}, B_{2g}, E_{1g} second peak; E_{2u}, A_{2u}, E_{2g} third peak. Molecular orbitals M1, M2, M3, and M4 on spectrum (1), associated to non-dispersing features in the ARPES maps (see Fig. 6.2), have been marked with vertical lines. (c) C 1*s* spectra measured at $h\nu = 400\,\text{eV}$ for three different coverages of coronene on Ir(1 1 1), compared with monolayer coronene on graphene/Ir(1 1 1) (blue curve) and pristine graphene on Ir(1 1 1) (dotted curve), and (inset) LEED pattern acquired at 86 eV electron energy after about 0.14 ML coronene deposition.

to those present in the spectrum of clean Ir(1 1 1) (2-gray), which is dominated by the large *d*-band density of states. These molecular states can be associated to non-dispersing features in the ARPES maps, which can be seen in Fig. 6.2. In particular the M1 peak, at 1.8 eV, together with the next state (M2) appearing at 2.4 eV can be attributed to hybridization of the coronene molecular orbitals with the Ir 5*d* bands. The Ir(1 1 1) surface's ability in creating strong π bonds with PAHs is confirmed by considering the spectral components appearing for other coronene-based interfaces with weaker interactions, *i.e.* coronene multilayers grown on Ir(1 1 1) (3-black) and for coronene on graphene/Ir(1 1 1) (4-blue). In these cases, besides the rigid shift induced by different charge transfer, the VB spectra are a clear fingerprint of the coronene molecular orbitals (E_{2u}, B_{1g}, B_{2g}, E_{1g}, E_{2u}, A_{2u}, E_{2g}), whose binding energy distribution is in excellent agreement with previous experimental findings and theoretical calculations [17–19]. Further insight into the modification of the electronic structure due to adsorption was gained by high-resolution XPS C 1*s* core level spectra, acquired at different molecular coverages (see Fig. 6.1(c)). The three-peak spectral shape and binding energies are very different from those measured for coronene on

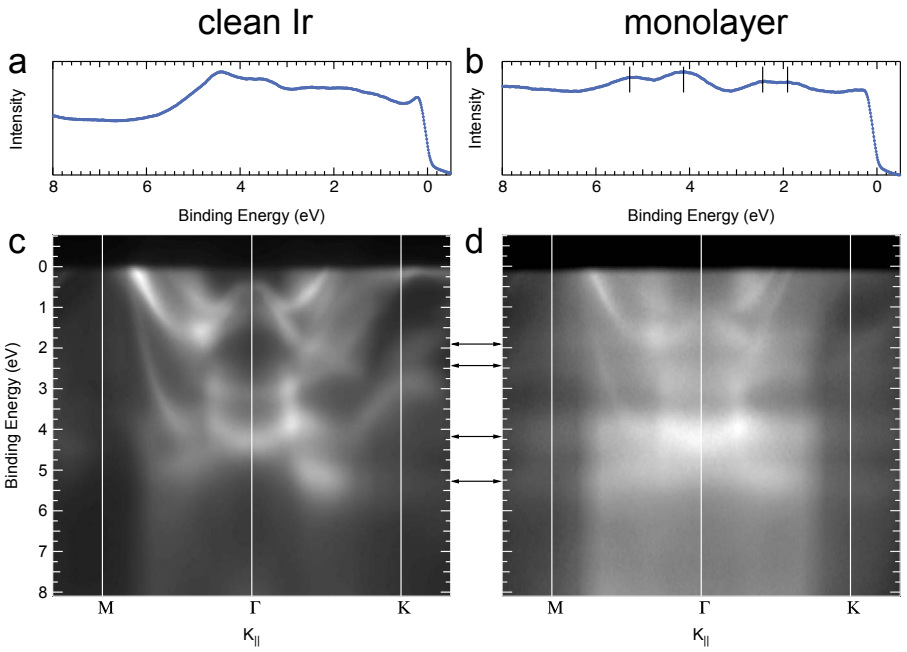

Figure 6.2: (a) Energy Dispersion Curve (EDC) for the clean Ir(111) obtained by selecting a vertical cut of the ARPES image below at the M point. (b) EDC curve for a monolayer of coronene on Ir(111) obtained by selecting a vertical cut of the ARPES image below at the M point. The molecular levels are shown superimposed (vertical bars). (c) ARPES map along the $M - \Gamma - K$ direction for the clean Ir(111) acquired at $h\nu = 34\,\text{eV}$. (d) ARPES map along the $M - \Gamma - K$ direction acquired ($h\nu = 34\,\text{eV}$) after deposition of a monolayer of coronene on Ir(111). The four clearly visible non-dispersing molecular levels are marked with arrows.

graphene (blue curve), and for coronene in gas phase, that displays a two-peak line shape [16]. In addition, the C 1*s* spectra measured at different coverages show the same line shape regardless of the coronene amount, suggesting that the adsorption configuration and site are not modified by intermolecular interactions in denser molecular layers or by the presence of surface defects, such as steps. It should be noted that the presence of three components cannot be simply justified as due to the geometrically non equivalent carbon atoms in the molecule, *i.e.* those forming the inner hexagon, the middle one, and the outer ring, because the spectral weight does not match the 1:1:2 ratio corresponding to the population of such non equivalent C atoms. The LEED pattern (see inset Fig. 6.1(c)) does not show any additional diffraction spots, besides those arising from the hexagonal symmetry of the Ir substrate, indicating that the coronene molecules do not pack forming a long-range ordered layer, but are rather randomly distributed among the free adsorption sites.

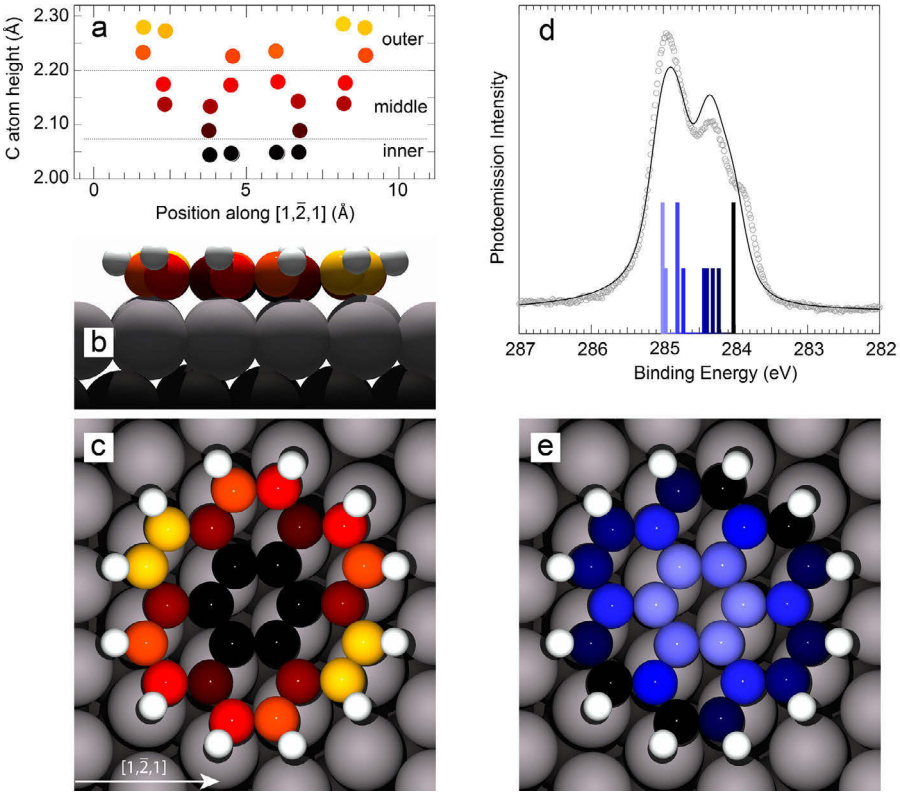

Figure 6.3: (a) Carbon-Ir distance for the non-equivalent C atoms of the coronene molecule. (b-c) Illustration of the side and top views of the $C_{24}H_{12}$ molecular orientation as found in DFT calculations. The color scale reflects the separation between the C atoms and the substrate beneath. Small differences in the C-Ir distance between apparently equivalent C atoms can be accounted for by considering the small influence of the second Ir layer, which breaks the 6-fold symmetry of the first atomic layer. (d) C 1*s* spectrum measured at normal emission and $h\nu = 400\,\text{eV}$ (empty circles) together with the fit result (solid line) and the calculated spectral distribution originated from the 24 C atoms. (e) Color scale in the model reflects the BEs of the different C 1*s* calculated components.

In order to further shed light on the coronene adsorption geometry, and on the origin of the different core level components, we performed DFT calculations. Several configurations were probed (see Fig. 6.4), including molecules with symmetry axes oriented along different directions, with different matches with respect to the high-symmetry adsorption sites of the Ir(1 1 1) surface, and also in non-planar configurations. The minimum energy configuration corresponds to coronene adsorbed with the inner C hexagon in bridge-site and the molecular axis aligned parallel to the [101] direction of Ir(1 1 1) (see Fig. 6.3(c)).

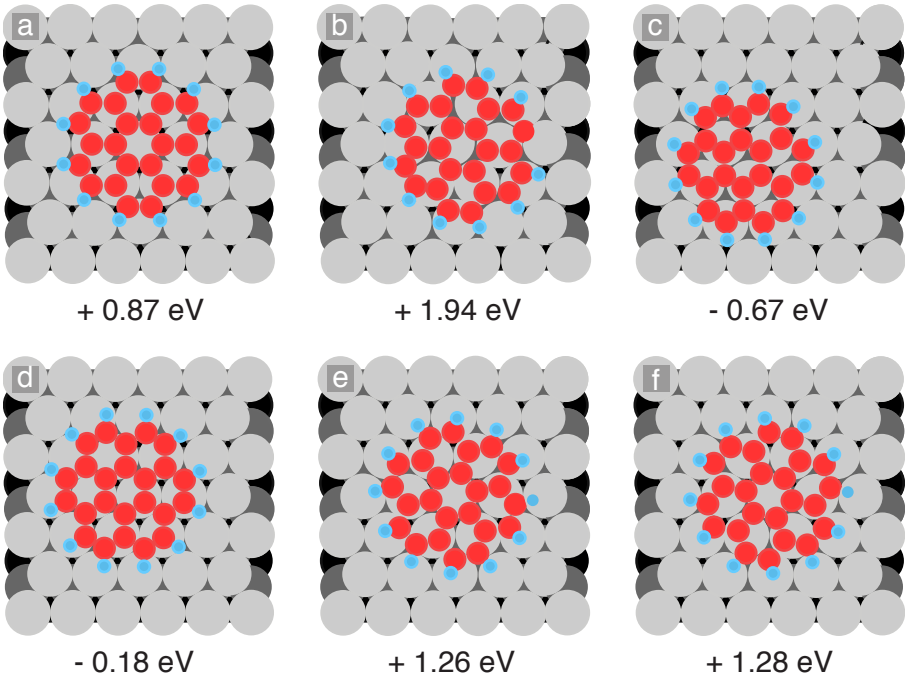

Figure 6.4: Relaxed structures for some of the geometries tested in the DFT calculations used to determine the best adsorption energy configuration. The adsorption energies are calculated with respect to the gas phase molecule configuration. The minimum energy configuration, used in the chapter, has an adsorption energy of −1.46 eV.

The molecules assume a bowl-like shape (side view shown in Fig. 6.3(b)), usually associated to π-conjugated compounds known as buckybowls or π-bowls [20, 21]. These species have been found to commonly form stable adlayers on metal surfaces, as in the case of corannulene ($C_{20}H_{10}$) on Cu(1 1 0) [22, 23] and of sumanene ($C_{21}H_{12}$) on Ag(1 1 1) [24]. In our case, the adsorbed molecule develops its bowl opening upwards: C atoms in the inner ring are about 0.23 Å closer to the surface with respect to C atoms in the outer ring (see Fig. 6.3(a)). The bowl-shaped geometry is enhanced by the hydrogen atoms displaying an average height of 2.74 Å, 0.7 Å farther from the surface than the inner C atoms, and a C−H bond angle ranging from 22° to 39° with respect to the Ir surface plane. In order to test the consistency of the minimum energy adsorption structure we compared in Fig. 6.3(d) the experimental C 1*s* core level spectra (empty circles), for which the molecule-substrate interaction is expected to have a strong influence, and fit results (solid line). We computed the C 1*s* core level binding energy (BE) for each of the 24 C atoms of the coronene molecules, including also final state effects due to core-hole screening. The

results, illustrated in Fig. 6.3(d), show that the computed BEs for the carbon atoms in the coronene molecule are not only linked to some extent to the C-metal distance (C atoms in the central ring showing the highest BEs), but are strongly dependent on the positions with respect to the first-layer Ir atoms. This is especially true for those C atoms sitting in the outer ring and bonded to H atoms, whose C 1*s* BE depends on the degree of interaction with the substrate Ir atoms, besides the bond with H instead of another C. The good agreement between experimental data and fit results strongly supports the DFT calculated molecular adsorption geometry.

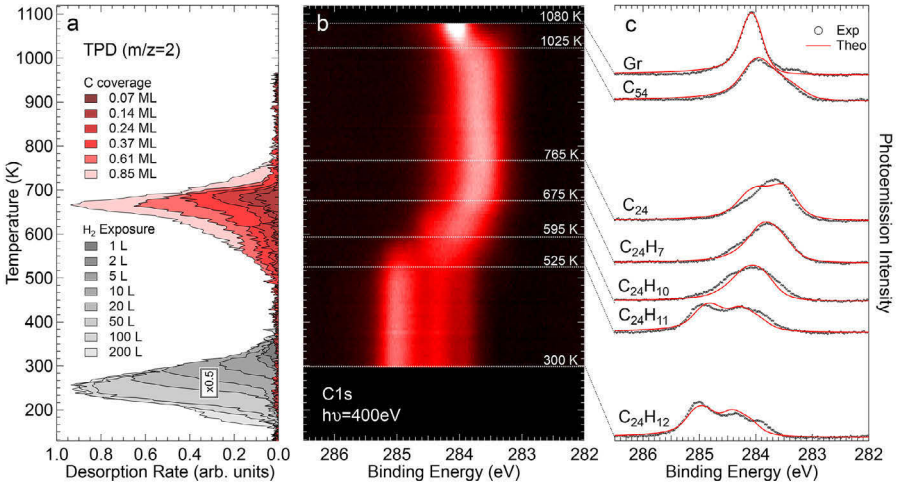

Figure 6.5: (a) Temperature programmed desorption spectra (red scale) of $m/z = 2$ after coronene deposition at different coverage and $T = 300\,\mathrm{K}$. For comparison desorption spectra (grey scale) corresponding to $m/z = 2$ after molecular hydrogen adsorption at $T = 100\,\mathrm{K}$ are reported (intensity rescaled by a factor 0.5). (b) Temperature dependent C 1*s* core level spectra (about 100 spectra) shown as a two-dimensional intensity plot. (c) Comparison between selected experimental C 1*s* core-level spectra and fit results (red curves).

In order to explore the mechanism of coronene dissociation we initially employed TPD, in the temperature range 150–950 K (see Fig. 6.5(a)), with the aim of finding the threshold of hydrogen desorption (mass to charge ratio $m/z = 2$), which can be used as a fingerprint for C−H break-up. Desorption spectra corresponding to different initial coverages of coronene are reported in red colored scale, indicating that H_2 in gas phase can be detected only above 500 K, with a maximum desorption rate at temperatures slightly higher than 650 K. To verify that on coronene the process of C−H bond dissociation does not take place at lower temperature, we compared the TPD data with a similar H_2 desorption experiment starting from hydrogen adsorption at $T = 100\,\mathrm{K}$. It is known that H_2 adsorbs dissociatively on Ir(1 1 1) [25, 26] and that the

onset of desorption is indicative of the recombination of two H atoms after surface diffusion. The large difference in H_2 formation temperature, and the lack of any overlap on the temperature scale of the desorption spectra from H_2 and $C_{24}H_{12}$, is a clear proof that coronene molecules undergo the first C−H breakup only above 500 K.

Further information about the coronene dissociation process was obtained following *in-situ* the temperature evolution of the C 1*s* core level spectrum from RT to 1120 K. The combination of a high-efficiency electron energy analyzer with a home-made delay-line detection system allowed us to measure each photoemission spectrum in about 30 s (still keeping the overall energy resolution to 40 meV), providing real-time spectroscopic visualization of the intermediate reaction stages. The image plot in Fig. 6.5 (b) shows the evolution of the C 1*s* spectrum at increasing temperature. As expected, the spectrum does not change during the initial stage of the temperature ramp, and only above 525 K, the onset temperature for H_2 desorption in the TPD spectra, clear changes are observed. The spectral intensity shifts to lower binding energy, reaching a rather constant value above 700 K, when the TPD results show that all hydrogen atoms have desorbed. Only above 1000 K the C 1*s* signal starts shifting back to higher BE. The BE value of 284.10 eV, reached above 1050 K, is a clear fingerprint of high-temperature graphene formation [27–30]. Notably, during the dissociation process, there is no loss in the overall C 1*s* spectral intensity, indicating that the energy barrier for C−H bond cleavage is lower than that for desorption of the intact molecule or C containing species. Unambiguous chemical assignment of the experimentally observed C 1*s* core-level line shape is, however, not easy, due to the high number of possible configurations of the dehydrogenated transient products. In order to interpret the C 1*s* spectral sequence, and to reach an atomistic understanding of the transient states involved in the thermal breakup of coronene, we resorted to DFT by performing extensive calculations of the energy barriers between the computed intermediate species, using the nudged elastic band (NEB) method [14].

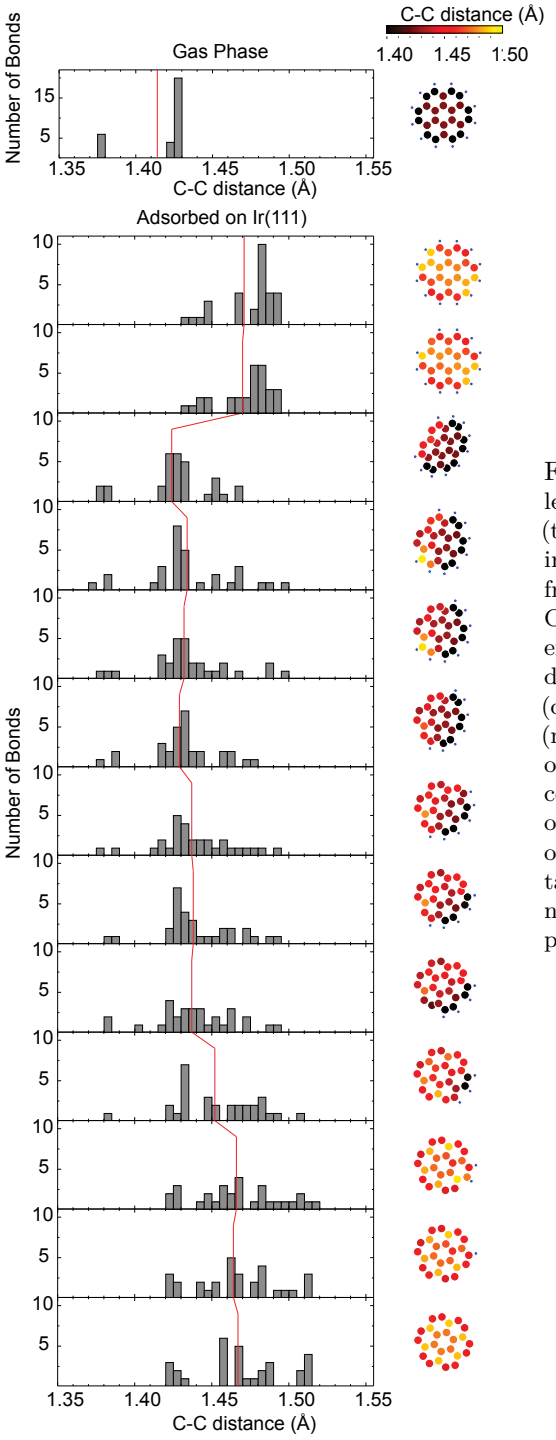

Figure 6.6: (left) C-C bond length histograms for gas phase (top), and adsorbed coronene during dehydrogenation, as obtained from DFT calculations. All the 30 C-C bonds were included. The average C-C bond length for each dissociation step is also reported (dashed red line).
(right) Schematic representation of gas phase (top), and adsorbed coronene during dehydrogenation of Ir(111). The C atoms are colored according to the mean distance from the 3 (or 2) nearest neighbors. The color scale is reported on top.

In Fig. 6.7 we show the twelve molecule-substrate configurations corresponding to the energetically most favored reaction pathway for breaking each C−H bond in n sequential steps (with n from 1 to 12), leaving the dehydrogenated molecules and an additional single H atom on the surface. The reaction-coordinate energy diagrams reported under the geometrical configurations are given with respect to the energy of the $n-1$ configuration, being $n = 0$ the intact adsorbed coronene molecule. It is important to stress that, despite the higher final state energy of each dehydrogenation step, the overall reaction can easily proceed at the temperature of our experiments, as dissociated H atoms can diffuse very rapidly on the surface forming H_2, which desorbs and is not available for the reverse process. For this reason the final state of structure n does not exactly correspond to the initial state of structure $n + 1$, where a H atom has been removed.

What is intriguing in our findings is the complex evolution of the molecular geometry during the dehydrogenation steps. Close inspection of the images shown in Fig. 6.7 (see also https://www.youtube.com/watch?v=zPDzDSWY7DQ) indicates that the stepwise dehydrogenation mechanism appears to be driven by the proximity of the C outer ring atom to the final adsorption position. At the beginning, the intact adsorbed molecule has significant internal C−C strain with respect to the gas phase configuration (see Fig. 6.6). The peripheral C closest to the most favorable position is the one which will lose an H atom in the next reaction step; the dissociation begins (see Fig. 6.7, $n = 1$) from one of the four equivalent peripheral C atoms closest to the top position, which, after losing its H atom, binds strongly to the surface and approaches its preferred adsorption site, much closer to the surface. The next key step of the dissociation, during the second dehydrogenation ($n = 2$), corresponds to the abrupt molecular lifting from the surface, resulting in an almost complete internal strain relief (see Fig. 6.6). In fact, three peripheral C atoms are positioned in equivalently favorable sites, giving therefore three candidate C−H bonds for the next dehydrogenation. But the lifting of the molecule has been found to give an energy gain of 0.67 eV with respect to the other configurations, thereby losing one of the two symmetry axes in the molecule, and causing the candidate C−H bond closest to the previously dehydrogenated one to be broken. At this point, one symmetry axis of the molecule with respect to the substrate still remains. Always keeping in mind that the driving mechanism for dehydrogenation is the proximity of the peripheral C atom to a top site, the two C atoms, adjacent to the freshly dehydrogenated carbons, are found to be equivalent. The evolution of the system towards the $n = 3$ state results in a clear twist of the molecule in one direction, in order to better accommodate the newly dehydrogenated C atom in its favored bond site on the substrate. This causes the loss of the second symmetry axis, and the remaining evolution of the dissociation reaction is fully determined. It is significant that during the dehydrogenation process also the atoms of the Ir substrate are slightly rearranged, in particular becoming more elevated with respect to the average surface plane, which eventually contributes to the formation of a stronger molecule-Ir bond. From this step on, the molecule

evolves by gradually completing the rotation to the final adsorption geometry, and by curling towards a dome shape configuration, always losing H atoms next to dehydrogenated bonds. This gradually changing shape increases the internal strain of the part attached to the substrate, whilst always keeping one end lifted until the very end, allowing for some strain to be relieved in the lifted portion of the molecule during the intermediate steps. The topology during the dissociation process is also affected by the contributions of the σ and π orbital overlap with the substrate d-bands, the former tending to cause the C rings to stand perpendicular to the surface, the latter trying to push the C ring parallel to it. The final state configuration is very similar to what has been found for the initial stages of growth of graphene using ethylene: dome-shaped C nanoislands whose interactions with the Ir substrate take place only at the cluster edges [28]. With increasing temperature, the mobility of the nanodomes becomes large enough to permit the formation of larger clusters and eventually graphene [31].

In order to confirm that the reaction intermediates, including the molecular lifting, twisting and curling, are more favorable with respect to the flat behavior, we simulated the C 1*s* core level spectra for all the carbon atoms in the most important configurations in Fig. 6.7 (1, 2, 5, 11, and 12), as well as for coronene, a larger nanodome formed by 54 C atoms - C_{54}, and graphene. The fit results, reported in Fig. 6.5(c) along with the experimental data, show an excellent agreement: the three-component line shape, associated to the $C_{24}H_{12}$ and $C_{24}H_{11}$ molecules, at 525 K changes and shifts to lower BE, and only when larger nanodomes are formed, because of coalescence and nucleation (see fit result corresponding to C_{54}), the spectral intensity distribution gets narrower. The single peak at 284.1 eV, fingerprint of graphene formation on Ir(1 1 1), appears only at high temperature (1080 K). We want to stress that the sequential dehydrogenation is a statistical process, and during the annealing there could be several different $C_{24}H_n$ species present on the surface. The amount of each species depends, besides from the energy barrier, also from pre-exponential factors and diffusion constants among other factors, which are difficult to calculate. In Fig. 6.5 (c) we report the C 1*s* core level spectra, along with the single molecular species fit result, for the most important intermediate molecules. Beside the initial and final configurations, corresponding to coronene and the C_{24} nanodome respectively, we report the spectrum associated to $C_{24}H_7$, which has the highest dehydrogenation barrier and is therefore expected to be stable for a larger temperature window on the surface. We also show the fit result associated to the tilted molecule, $C_{24}H_{10}$, since it represents a crucial step in the dissociation pathway, and to $C_{24}H_{11}$, which represents the first dissociation product. Even though the process illustrated in Fig. 6.7 is the most energetically favorable, we also tested many other reaction paths that revealed striking differences in terms of geometry, and do not include the process of molecular lifting and curling. For example we found that an alternative possibility is that, after the first dehydrogenation, the molecules break the next C−H bond but still remain flat on the surface. However the final state is 0.67 eV higher in

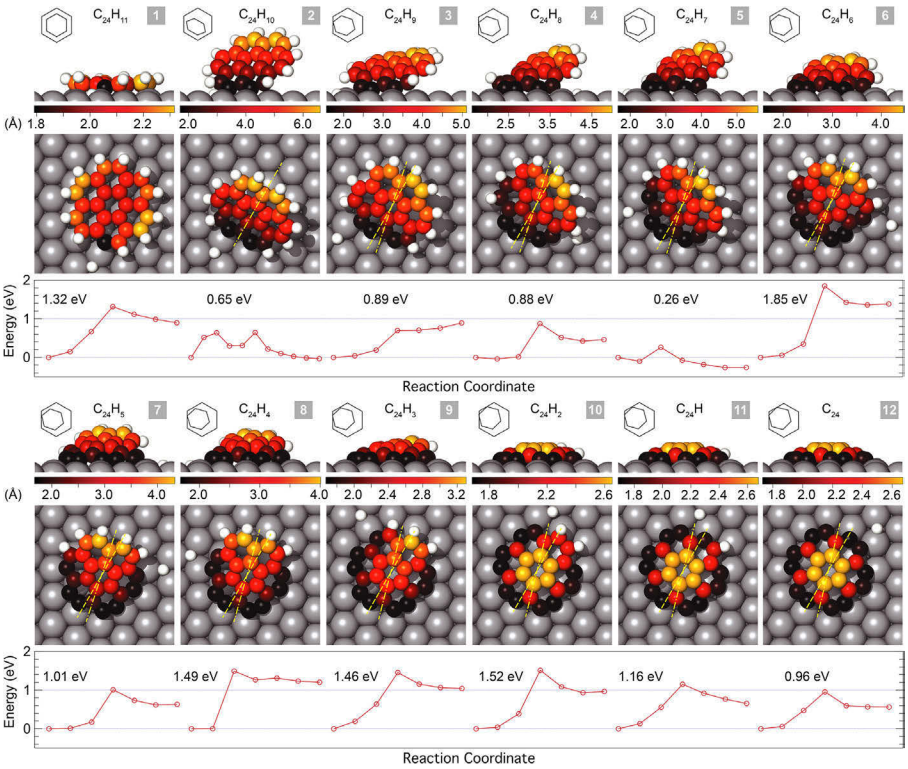

Figure 6.7: (a) Illustration of final states side and top views of $C_{24}H_n$ through the 12 sequential C−H bond cleavages that bring coronene molecules to the nanodome configuration. Different colors correspond to different C-metal substrate heights. The colors have been rescaled in each step to emphasize the geometrical differences in each configuration (the height scale in Å is also reported for each step of the reaction). Above each illustration, a schematic representation of the coronene to Ir relative orientation is reported. The yellow dash-dotted line in step 2 represents the symmetry axis shared by the adsorbed coronene molecule and the Ir substrate. In steps $n = 3-12$, the dashed line represents the original coronene orientation, while the dash-dotted line represents the current one. Below each illustration, a graph representing the energy evolution during the NEB simulations is shown with the total energy barrier for the single dehydrogenation step.

energy. Moreover, the evolution of the reaction following this new sequence would end up with a C_{24} carbon cluster in a geometrical configuration that is by far not energetically favorable. In fact, it is important to stress that the un-rotated C cluster, *i.e.* the one presenting the same azimuthal orientation as the original coronene molecule, has a 2.27 eV higher energy. Notably, the reaction path involving the flat dissociation behavior results in a calculated C 1*s* core level spectrum with an additional component growing at lower BE (at

282.9 eV), which is not experimentally observed. In fact, during the flat dissociation pathway, some Ir atoms that bind to peripheral C atoms of the partially dissociated molecule, are also bound to another C atom. This produces the theoretically predicted, but not experimentally observed, low BE component in the C 1*s* spectrum.

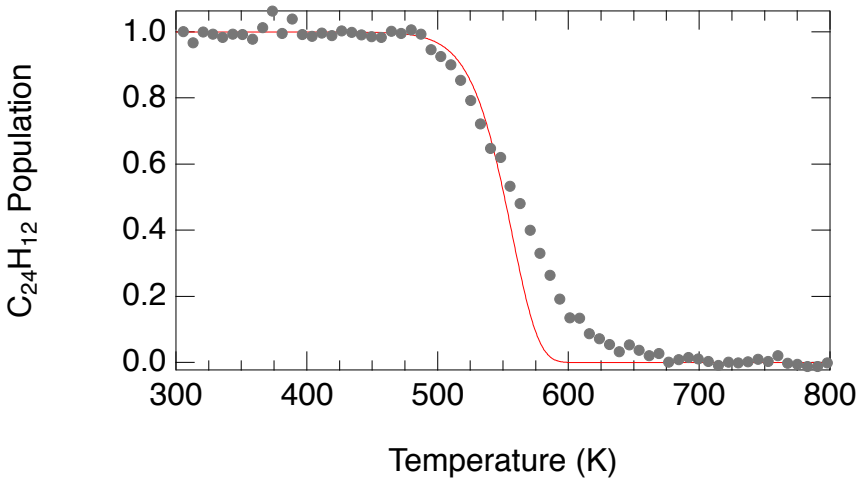

Figure 6.8: Experimental $C_{24}H_{12}$ population (grey dots) as calculated from the experimental data by judging the photoemission intensity evolution around 285 eV BE (see Fig. 6.5), where the main contribution is expected to be due to undissociated coronene. The population is normalized to the initial intensity. The rate equation theoretical model for the first dissociation, obtained from the DFT calculated energy barrier (1.32 eV) and assuming a $10^{10}\,s^{-1}$ pre-exponential factor, is also shown (red curve). At temperature above 550 K, the observed broadening of the experimental curve is due to the spectral contribution arising from the high BE tail of the C 1*s* signal due to dissociated molecules.

As a final step of our investigation, we have compared the experimental $C_{24}H_{12}$ coverage evolution with temperature, as extracted from the C 1*s* photoemission data (see Fig. 6.8), to a theoretical prediction based on a microkinetic model, assuming that the reaction rate depends on the activation energy of the first C−H bond breaking reaction step through a Boltzmann factor, with an energy barrier deduced from the NEB calculations, allowing only the pre-exponential order of magnitude as a free parameter. The temperature behavior is in good agreement with the experimentally observed decrease of the $C_{24}H_{12}$ population when the pre-exponential factor is equal to $10^{10}\,s^{-1}$. This value, that at first instance seems quite low if compared with the typical value of $10^{13}\,s^{-1}$, is however not surprising. As recently reported by Campbell *et al.* by discussing extensive experimental results [32], ν_{diss} prefactors for dissociation are found typically 1/10 to $1/10^5$ of the prefactors for desorption ν_{des} of the

same molecule, with an average ratio (ν_{diss}/ν_{des}) of about 1/1000, because of entropy loss at the transition state. It is interesting to compare our experimental finding with those obtained for the simplest aromatic molecule, *i.e.* benzene (C_6H_6) [33]. Theoretical calculations of benzene adsorption on Cu(1 0 0) show that, after the first hydrogen scission starting from its flat adsorption configuration, also the phenyl radical C_6H_5 and the ortho-benzyne species C_6H_4 assume upright configurations. It is interesting to observe that instead, the dissociation of benzene on Pt(1 1 1), which is a transition metal quite similar to Ir, results in a tilted configuration with the C atoms adsorbed through C at the top site [34]. Our results therefore suggest that the process of thermally activated molecular lifting can be a more general behavior in the dissociation process of similar molecules, also for larger PAHs. We suppose that this is the case for other transition metal surfaces, where the presence of unsaturated C bonds could lead to the development of strong interactions between the partially dehydrogenated molecules and the metal substrates. The main driving force resulting in the tilt and rotation of the molecule before curling, *i.e.* the creation of new bonds with the substrate which breaks the molecular symmetries and allows for some internal strain relief, somehow mimics what happens in the case of heterocyclic aromatic adsorbates such as pyridine, pyrrole and thiophene for which, besides flat-lying configurations, also tilted geometries have been reported [35].

6.3 Conclusions

We have shown, using a multi-method experimental approach and extensive theoretical calculations, that coronene molecules adsorbed on Ir(1 1 1) undergo major conformational changes during the dissociation process, which bring the molecules from a flat, slightly upwards-pointing bowl shape, to graphene, through a series of exotic configurations. Once again, the approach that has been extensively tested in previous experiments, has proven effective in determining otherwise hardly accessible data.

Upon the second C−H bond cleavage, the molecules tilt upward with respect to the surface, and then rotate to accommodate the reactive C terminations to the most favorable bond site with the substrate. During the lifting, the C−C strain is initially relieved, while as the dehydrogenation proceeds, the molecules experience a progressive increase in the average interatomic distance, and gradually settle to form peculiar dome shaped nanographene flakes. By exploiting this reaction mechanism, we envisage the possibility of creating new nanostructures with different functionalities by encapsulating single adatoms below the carbon dome, through diffusion of the new species underneath the carbon disk just before the formation of large carbon clusters, in a similar way as already demonstrated for larger Sn nanoparticles for applications in lithium batteries [36]. It is clear that this concept would require an accurate control of the status of the molecular structure, which is a challenging task, but the lifting of the molecule could be an important step to follow this strategy.

In fact, the process of intercalation of atomic species below already formed nanographenes, which could have interesting application in spintronics [37] and energy storage [38], is strongly hindered by the strong C-metal bonds formed at the edges which prevent the atomic penetration below the C flake. Besides the confinement of magnetic species below nanographene flakes, also the presence of chemically inert species below the nanographenes is expected to modify the electronic edge states giving rise to interesting magnetic phenomena [39]. The use of nanostructured surfaces, such as those formed by a high density of monoatomic steps or vacancies, could be a possibility to reduce the geometrical degree of freedom forced by the hexagonal surface of Ir(1 1 1), with C_{3v} symmetry, and achieve an easier control of the reaction parameters. Finally, the control of molecular tilt in PAHs could tailor their chemical reactivity, by activating or inhibiting specific reactions that are usually catalyzed by the surface, as reported for example in the case of different carbonyl compounds, more specifically aldehydes, on transition metal substrates [40, 41].

References

[1] Son, Y.-W.; Cohen, M. L.; Louie, S. G. Half-metallic graphene nanoribbons. *Nature* **2006**, *444*, 347.

[2] Yang, L.; Park, C.-H.; Son, Y.-W.; Cohen, M. L.; Louie, S. G. Quasiparticle Energies and Band Gaps in Graphene Nanoribbons. *Physical Review Letters* **2007**, *99*, 186801.

[3] Chen, Y.-C.; de Oteyza, D. G.; Pedramrazi, Z.; Chen, C.; Fischer, F. R.; Crommie, M. F. Tuning the Band Gap of Graphene Nanoribbons Synthesized from Molecular Precursors. *ACS Nano* **2013**, *7*, 6123.

[4] Ruffieux, P.; Cai, J.; Plumb, N. C.; Patthey, L.; Prezzi, D.; Ferretti, A.; Molinari, E.; Feng, X.; Müllen, K.; Pignedoli, C. A.; Fasel, R. Electronic Structure of Atomically Precise Graphene Nanoribbons. *ACS Nano* **2012**, *6*, 6930.

[5] Fujii, S.; Enoki, T. Nanographene and Graphene Edges: Electronic Structure and Nanofabrication. *Accounts of Chemical Research* **2013**, *46*, 2202.

[6] Narita, A.; Feng, X.; Müllen, K. Bottom-Up Synthesis of Chemically Precise Graphene Nanoribbons. *The Chemical Record* **2015**, *15*, 295.

[7] Otero, G.; Biddau, G.; Sanchez-Sanchez, C.; Caillard, R.; Lopez, M. F.; Rogero, C.; Palomares, F. J.; Cabello, N.; Basanta, M. A.; Ortega, J.; Mendez, J.; Echavarren, A. M.; Perez, R.; Gomez-Lor, B.; Martin-Gago, J. A. Fullerenes from aromatic precursors by surface-catalysed cyclodehydrogenation. *Nature* **2008**, *454*, 865.

[8] Cai, J.; Ruffieux, P.; Jaafar, R.; Bieri, M.; Braun, T.; Blankenburg, S.; Muoth, M.; Seitsonen, A. P.; Saleh, M.; Feng, X.; Müllen, K.; Fasel, R. Atomically precise bottom-up fabrication of graphene nanoribbons. *Nature* **2010**, *466*, 470.

[9] Müllen, K.; Rabe, J. P. Nanographenes as Active Components of Single-Molecule Electronics and How a Scanning Tunneling Microscope Puts Them To Work. *Accounts of Chemical Research* **2008**, *41*, 511.

[10] Narita, A.; Wang, X.-Y.; Feng, X.; Müllen, K. New advances in nanographene chemistry. *Chemical Society Reviews* **2015**, *44*, 6616.

[11] Treier, M.; Pignedoli, C. A.; Laino, T.; Rieger, R.; Müllen, K.; Passerone, D.; Fasel, R. Surface-assisted cyclodehydrogenation provides a synthetic route towards easily processable and chemically tailored nanographenes. *Nature Chemistry* **2011**, *3*, 61.

[12] Baraldi, A.; Comelli, G.; Lizzit, S.; Cocco, D.; Paolucci, G.; Rosei, R. Temperature programmed X-ray photoelectron spectroscopy: a new technique for the study of surface kinetics. *Surface Science* **1996**, *367*, L67.

[13] Doniach, S.; Šunjić, M. Many-electron singularity in X-ray photoemission and X-ray line spectra from metals. *Journal of Physics C: Solid State Physics* **1970**, *3*, 285.

[14] Henkelman, G.; Uberuaga, B. P.; Jónsson, H. A climbing image nudged elastic band method for finding saddle points and minimum energy paths. *The Journal of Chemical Physics* **2000**, *113*, 9901.

[15] Köhler, L.; Kresse, G. Density functional study of CO on Rh(1 1 1). *Physical Review B* **2004**, *70*, 165405.

[16] Fronzoni, G.; Baseggio, O.; Stener, M.; Hua, W.; Tian, G.; Luo, Y.; Apicella, B.; Alfé, M.; de Simone, M.; Kivimäki, A.; Coreno, M. Vibrationally resolved high-resolution NEXAFS and XPS spectra of phenanthrene and coronene. *The Journal of Chemical Physics* **2014**, *141*, 044313.

[17] Boschi, R.; Clar, E.; Schmidt, W. Photoelectron spectra of polynuclear aromatics. III. The effect of nonplanarity in sterically overcrowded aromatic hydrocarbons. *The Journal of Chemical Physics* **1974**, *60*, 4406.

[18] Schroeder, P. G.; France, C. B.; Parkinson, B. A.; Schlaf, R. Orbital alignment at p-sexiphenyl and coronene/layered materials interfaces measured with photoemission spectroscopy. *Journal of Applied Physics* **2002**, *91*, 9095.

[19] Medjanik, K.; Kutnyakhov, D.; Nepijko, S. A.; Schonhense, G.; Naghavi, S.; Alijani, V.; Felser, C.; Koch, N.; Rieger, R.; Baumgarten, M.; Müllen, K. Electronic structure of large disc-type donors and acceptors. *Physical Chemistry Chemical Physics* **2010**, *12*, 7184.

[20] Wu, Y.-T.; Siegel, J. S. Aromatic Molecular-Bowl Hydrocarbons: Synthetic Derivatives, Their Structures, and Physical Properties. *Chemical Reviews* **2006**, *106*, 4843.

[21] Tsefrikas, V. M.; Scott, L. T. Geodesic Polyarenes by Flash Vacuum Pyrolysis. *Chemical Reviews* **2006**, *106*, 4868.

[22] Parschau, M.; Fasel, R.; Ernst, K.-H.; Gröning, O.; Brandenberger, L.; Schillinger, R.; Greber, T.; Seitsonen, A.; Wu, Y.-T.; Siegel, J. Buckybowls on Metal Surfaces: Symmetry Mismatch and Enantiomorphism of Corannulene on Cu(1 1 0). *Angewandte Chemie International Edition* **2007**, *46*, 8258.

[23] Xiao, W.; Passerone, D.; Ruffieux, P.; Aït-Mansour, K.; Gröning, O.; Tosatti, E.; Siegel, J. S.; Fasel, R. C_{60}/Corannulene on Cu(1 1 0): A Surface-Supported Bistable Buckybowl–Buckyball Host–Guest System. *Journal of the American Chemical Society* **2008**, *130*, 4767.

[24] Jaafar, R.; Pignedoli, C. A.; Bussi, G.; Aït-Mansour, K.; Groening, O.; Amaya, T.; Hirao, T.; Fasel, R.; Ruffieux, P. Bowl Inversion of Surface-Adsorbed Sumanene. *Journal of the American Chemical Society* **2014**, *136*, 13666.

[25] Hagedorn, C. J.; Weiss, M. J.; Weinberg, W. H. Dissociative chemisorption of hydrogen on Ir(1 1 1): Evidence for terminal site adsorption. *Physical Review B* **1999**, *60*, R14016.

[26] Moritani, K.; Okada, M.; Nakamura, M.; Kasai, T.; Murata, Y. Hydrogen-exchange reactions via hot hydrogen atoms produced in the dissociation process of molecular hydrogen on Ir(1 1 1). *The Journal of Chemical Physics* **2001**, *115*, 9947.

[27] Preobrajenski, A. B.; Ng, M. L.; Vinogradov, A. S.; Mårtensson, N. Controlling graphene corrugation on lattice-mismatched substrates. *Physical Review B* **2008**, *78*, 073401.

[28] Lacovig, P.; Pozzo, M.; Alfè, D.; Vilmercati, P.; Baraldi, A.; Lizzit, S. Growth of Dome-Shaped Carbon Nanoislands on Ir(1 1 1): The Intermediate between Carbidic Clusters and Quasi-Free-Standing Graphene. *Physical Review Letters* **2009**, *103*, 166101.

[29] Lizzit, S.; Baraldi, A. High-resolution fast X-ray photoelectron spectroscopy study of ethylene interaction with Ir(1 1 1): From chemisorption to dissociation and graphene formation. *Catalysis Today* **2010**, *154*, 68.

[30] Presel, F.; Jabeen, N.; Pozzo, M.; Curcio, D.; Omiciuolo, L.; Lacovig, P.; Lizzit, S.; Alfè, D.; Baraldi, A. Unravelling the roles of surface chemical composition and geometry for the graphene-metal interaction through C1s core-level spectroscopy. *Carbon* **2015**, *93*, 187.

[31] Coraux, J.; N'Diaye, A. T.; Engler, M.; Busse, C.; Wall, D.; Buckanie, N.; zu Heringdorf, F.-J. M.; van Gastel, R.; Poelsema, B.; Michely, T. Growth of graphene on Ir(1 1 1). *New Journal of Physics* **2009**, *11*, 023006.

[32] Campbell, C. T.; Árnadóttir, L.; Sellers, J. R. Kinetic prefactors of reactions on solid surfaces. *Zeitschrift für Physikalische Chemie* **2013**, *227*, 1435.

[33] Lesnard, H.; Bocquet, M.-L.; Lorente, N. Dehydrogenation of Aromatic Molecules under a Scanning Tunneling Microscope: Pathways and Inelastic Spectroscopy Simulations. *Journal of the American Chemical Society* **2007**, *129*, 4298.

[34] Gao, W.; Zheng, W. T.; Jiang, Q. Dehydrogenation of benzene on Pt(1 1 1) surface. *The Journal of Chemical Physics* **2008**, *129*, 164705.

[35] Jenkins, S. J. Aromatic adsorption on metals via first-principles density functional theory. *Proceedings of the Royal Society A* **2009**, *465*, 2949.

[36] Cui, G.; Hu, Y.-S.; Zhi, L.; Wu, D.; Lieberwirth, I.; Maier, J.; Müllen, K. A One-Step Approach Towards Carbon-Encapsulated Hollow Tin Nanoparticles and Their Application in Lithium Batteries. *Small* **2007**, *3*, 2066.

[37] Sicot, M.; Leicht, P.; Zusan, A.; Bouvron, S.; Zander, O.; Weser, M.; Dedkov, Y. S.; Horn, K.; Fonin, M. Size-Selected Epitaxial Nanoislands Underneath Graphene Moiré on Rh(1 1 1). *ACS Nano* **2012**, *6*, 151.

[38] Xu, F.; Tang, Z.; Huang, S.; Chen, L.; Liang, Y.; Mai, W.; Zhong, H.; Fu, R.; Wu, D. Facile synthesis of ultrahigh-surface-area hollow carbon nanospheres for enhanced adsorption and energy storage. *Nature Communications* **2015**, *6*, 7221.

[39] Fujii, S.; Ziatdinov, M.; Ohtsuka, M.; Kusakabe, K.; Kiguchi, M.; Enoki, T. Role of edge geometry and chemistry in the electronic properties of graphene nanostructures. *Faraday Discuss.* **2014**, *173*, 173.

[40] Chiu, M. E.; Watson, D. J.; Kyriakou, G.; Tikhov, M. S.; Lambert, R. M. Tilt the Molecule and Change the Chemistry: Mechanism of S-Promoted Chemoselective Catalytic Hydrogenation of Crotonaldehyde on Cu(1 1 1). *Angewandte Chemie* **2006**, *118*, 7692.

[41] Brandt, K.; Chiu, M. E.; Watson, D. J.; Tikhov, M. S.; Lambert, R. M. Chemoselective Catalytic Hydrogenation of Acrolein on Ag(1 1 1): Effect of Molecular Orientation on Reaction Selectivity. *Journal of the American Chemical Society* **2009**, *131*, 17286.

Chapter 7

Reversible dehydrogenation of pentacene on Ir(1 1 1)

In this chapter, reversible temperature-induced dehydrogenation of pentacene molecules on Ir(1 1 1) is demonstrated. This novel phenomenon has interesting applications to graphene nanoribbons, opening new possibilities for experiments supporting the many theoretical calculations that are being performed on these systems [1–3].

Quite recently, major advances have been made in the application of bottom-up approaches for graphene nanoribbon growth by exploiting the Ullmann reaction [4–6], so that it has become possible to consistently obtain nanoribbons with excellent edge smoothness. It is become evident that, as theoretically predicted, the edges of graphene nanoribbons play a major role in determining their properties [2, 3, 7, 8]. For example, it has been predicted that in nanoribbon-based transistors, edge defects and the associated localized states induced in the band gap cause larger leakage currents and smaller on currents [9], showing that the exact nature of the edges of graphene nanoribbons should be one of the main concerns for technological applications.

As already stated, graphene nanoribbons are a versatile tool for bandgap engineering in graphene [10–12], and although they are in principle relatively simple structures, there are quite a few ways to tailor their electronic band structure. The width is one of the principal parameters [1, 13], but also termination (zigzag vs armchair) [3] and hydrogen passivation [2, 14] are crucial in determining the properties. However, the vast majority of studies have been carried out for hydrogen terminated graphene nanoribbons. But hydrogen can negatively affect many properties: its presence as an edge passivator, for example, reduces carrier mobility [14], and has detrimental effect on thermal transport in graphene nanoribbons [15]. Ideal graphene nanoribbons are predicted to have thermal conductivities that, in the worst case, are 3 times that of diamond.

Edge roughness or the presence of hydrogen have about the same effect, with thermal conductivity values that are about 1/3 of the smooth, non hydrogen terminated edge case. For these reasons, it might be a central issue to find new ways to remove or add the hydrogen atoms at the edges. Reversible hydrogen removal from the highly perfect nanoribbons obtained by bottom-up approaches such as dehalogenation might lead to interesting switching applications, for example in thermal transport. Our simple molecular model is representative of true graphene nanoribbons in the de/rehydrogenation process, and represents a first step for this new approach to graphene nanoribbon property tuning.

Another recent hot topic has been the reversible hydrogenation of graphene-based hydrogen storage solutions [16]. New materials like graphane [17, 18] and graphone [19] are seen as interesting approaches because of the stability of the graphene support, and because of the good release properties for H [16]. In our case, however, even not considering the substrate's effect to the total density, the system would only reach a maximum hydrogen weight density of 5 $wt\%$. To put this number in perspective, in 2015 the Fuel Cell Technology Office of the Unites States Department of Energy set the 2020 target of 5.5 $wt\%$ and an ultimate target of 7.5 $wt\%$ for the gravimetric storage capacities of onboard hydrogen storage materials for light-duty vehicles [20]. Catalyst assisted reversible hydrogenation of graphene-based materials is not a viable approach for hydrogen storage, because of the unsustainable weight of the catalyst atoms necessary for the reactions. Furthermore, even without the catalysts, only graphane theoretically reaches an efficiency level compatible with the targets, at 7.7 $wt\%$, while already with graphone the gravimetric density is 4.0 $wt\%$.

As a last comment, dehydrogenation of the pentacene molecules themselves might be of interest. In fact, pentacene is considered a benchmark organic semiconductor for electronic devices, giving pentacene a long history as the central component for molecular and organic electronics [21–25]. However, most applications rely on crystalline frameworks or molecular nanocrystals, but the π-conjugated electronic structure, the relatively small HOMO-LUMO gap and the relatively high carrier mobility makes these molecules interesting even in the isolated form. Furthermore, upon hydrogen removal, the general trend for bandgaps in graphene nanoribbons is to become smaller [14]. It might be reasonable to expect a similar behavior for pentacene, with a HOMO-LUMO gap becoming compatible with single molecule electronic devices upon hydrogen removal, and perhaps allowing switching between 2 gap values by reversible de/rehydrogenation.

7.1 Methods

Single adlayers of pentacene on Ir(1 1 1) have been characterized by LEED, XPS, TPD, STM, and DFT calculations. LEED, SPA-LEED, and TPD experiments were carried out in the UHV chamber of the Surface Science Laboratory, while High resolution XPS and TP-XPS experiments were carried out at the

SuperESCA endstation. In both cases the base pressure was below 10^{-10} mbar. STM measurements have been performed by Emil Sierda with the LHe-STM of the STM/SPSTM laboratory [26] at the Physics Department of the University of Hamburg. The UHV chamber has a base pressure better than 5×10^{-11} mbar. DFT calculations were performed by Prof. Dario Alfè at University College London.

The Ir(1 1 1) single crystal was cleaned following the usual recipe: repeated sputtering/annealing cycles were performed using 1.5 keV Ar^+ at two different angles for the sputtering, and using 3 W filaments placed close to the back side of the sample (about 1 mm) for heating by electron bombardment to 1420 K. Temperature was monitored by using 2 independent k-type thermocouples spot welded on the back of the sample, close to opposite sides. After each sputtering/annealing cycle, the surface was subject to 5 oxidation and 5 reduction cycles to completely remove residual C and O contamination from the surface. At the SuperESCA beamline, it was possible to monitor *in situ* the C 1*s* and O 1*s* core levels to determine in real time the residual contamination. The sample was cooled to 77 K for all LEED, SPA-LEED, and high resolution XPS measurements.

Commercially available (Sigma-Aldrich) pentacene powder (triple-sublimed grade, >99.995% purity) was used throughout the experiment. The molecules were deposited on the Ir surface at 320 K in the preparation chamber by sublimation from a home-built BN crucible heated by a Ta wire and equipped with a thermocouple in direct contact with the pentacene powder for temperature monitoring during the evaporation. The empty crucible was cleaned from volatile impurities in a separate UHV chamber by heating it for 10 h at 670 K. The pentacene was then placed in the crucible and purified in the experimental chamber by repeated flashing at temperatures up to 430 K. All evaporations were performed by heating the pentacene in the crucible to 420 K. The pentacene coverage and evaporation rate for all the experiments were calibrated by comparing the C 1*s* core level spectrum area after pentacene deposition to the C 1*s* core level spectrum area of a full graphene layer grown by temperature programmed growth from ethylene (following the recipe in Ch. 4, the reference coverage was assumed to be 2.47 ML). Coverages in this work should always be intended as the number of C atoms for every substrate atom, so that the ML units refer to the C coverage.

C 1*s* spectra were acquired in the Surface Science Laboratory by using a conventional X-ray Mg K_α source. At the SuperESCA beamline, C 1s spectra were measured with photon energies between 375 eV and 400 eV, and were acquired along with a measurement of the Fermi level, which was used to align the binding energy scale. In order to check for possible X-ray induced molecular break-up we performed several scans along the surface to search for C 1s spectral modifications, without finding appreciable differences. All XPS measurements were performed in normal emission geometry.

TP-XPS experiments have been performed by acquiring *in situ* XPS spectra at normal emission, with a photon energy of 400 eV, while annealing the

sample with a linear temperature ramp at 0.25 K/s from 100 K to 1280 K, after pentacene deposition. The average time per spectrum was about 15 s, corresponding to temperature intervals of less than 4 K. In the TP-XPS experiments, in order to determine the amount of pristine pentacene for each spectrum between 100 K and 600 K, in a simple picture where one species transforms into another, a fitting procedure was employed where, in effect, a sum of two spectral distributions was fitted to each spectrum. The fits were performed by only using 3 free parameters, leaving all others fixed. Free parameters were the relative intensities of the two spectral distributions, and an extra Gaussian component, to account for thermal broadening. The first spectral distribution was obtained by using a sum of 3 D-S functions with a Shirley background that empirically describes well the observed high resolution C 1*s* spectrum at low temperature. A similar procedure was used to empirically determine the lineshape of the C 1*s* spectrum at 600 K. These two spectral distributions were then used to fit the TP-XPS spectra.

TPD curves have been acquired using an SRS 200 residual gas analyzer (RGA) for a mass to charge ratio $m/z = 2$, giving the H_2 desorption rate from the surface: after pentacene deposition, the sample was annealed at a fixed rate of 2.5 K/s while continuously acquiring the intensity of the signal generated by the RGA.

Density functional theory calculations have been carried out using the VASP code. The Projector Augmented Wave (PAW) method was used to account for the core electrons, with the 6*s* and 5*d* electrons of Ir and the 2*s* and 2*p* electrons of C explicitly included in the valence. Single particle orbitals were expanded in plane-waves using a kinetic energy cut-off of 400 eV. Surfaces were modeled with the usual slab geometry, using a (12 x 6) supercell with 4 layers, of which the bottom two were kept frozen at the bulk interatomic distances. The large cell was chosen so that a densely packed layer with 4 molecules could be simulated. The vacuum was ~ 17.8 Å for the clean surface and ~ 15 Å for the system with the pentacene molecules adsorbed on the surface. Only the Gamma point was used to sample the Brillouin zone. C 1*s* core-level BEs have been estimated in the final-state approximation, therefore including also final state effects due to core-hole screening.

Similar to previous experiments on coronene and graphene, the C 1s spectra were analyzed using a sum of 22 D-S functions convoluted with Gaussians, including a Shirley type background. The relative BE shifts between the components were constrained to the values found by DFT, while a rigid shift was imposed to align the experimental BE scale to the theoretical one. Experimental data and fitting results have been displayed after subtracting the background found by the fitting operation.

STM images were acquired for the pentacene covered surface with a coverage of 0.3 ML. The measurements were performed at 25 K, with tunneling voltage $V = -500$ mV, tunneling current $I = 100$ pA. The substrate crystallographic directions were determined by the direction of a dislocation that was found on the clean surface.

7.2 Results and Discussion: Pristine Molecules

First, we performed LEED measurements for 0.5 ML of pentacene deposited on Ir(1 1 1). The LEED patterns (see Fig. 7.1) reveal a (3×1) superperiodicity. This pattern with large spots and diffraction intensity at low $k_{//}$ is typical of systems where thin, long structures form random close packed arrangements, placed side-by-side at fixed distances, and therefore with a single observed periodicity in the short direction, like graphene nanoribbons on (1 1 1) transition metal surfaces [27]. Our case is similar: the average pentacene-pentacene distance along the short molecular axis is compatible with such a superperiodicity, which would be determined by a flat-laying, side-by-side molecular packing. However, it is hard to say whether the superperiodicity is a true (3 × 1), especially in the ×1 direction. One hypothesis is that the individual hydrocarbon rings are epitaxial with the substrate, with 5 diffracting units giving the observed LEED intensity. This number is quite small, and a more likely explanation

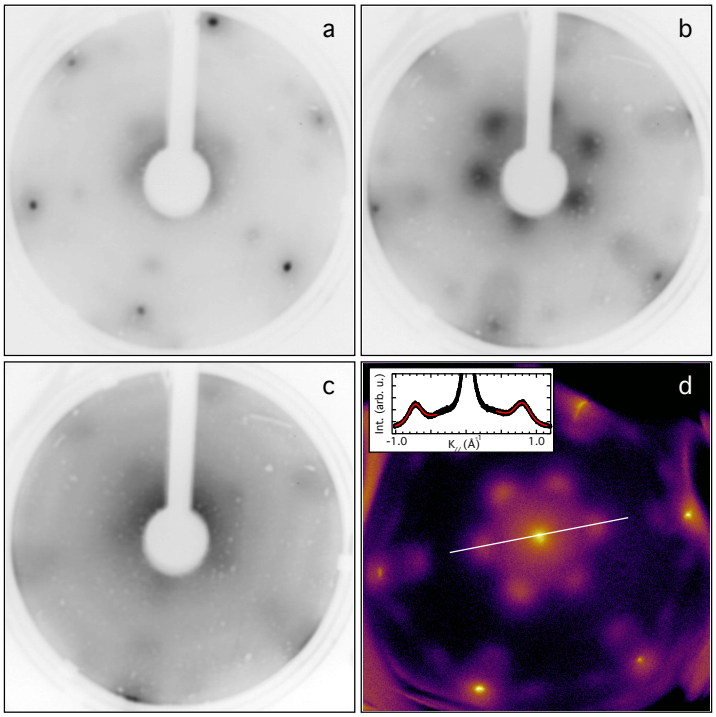

Figure 7.1: LEED images acquired after deposition of 0.5 ML of pentacene (carbon coverage), at 68 eV (a), 54 eV (b), and 42 eV (c). In (d), a SPA-LEED image shows the diffraction pattern around the (0,0) spot at 54 eV, and the inset shows a high statistics profile that was used to calculate the pentacene superstructure's spot width. Fits of the profile are marked in red.

is that the periodicity along the ×1 direction is actually undefined. Relative shifts between rows of pentacene molecules would be hardly detectable by LEED, because of the long periodic nature of the pentacene molecules: rows of molecules with translational disorder on the long molecular axis, but with a fixed distance between them along the short axis, could still give such a diffraction pattern. In any case, the spot profile analysis (Fig. 7.1(d), inset) reveals that the average domain size is 25 Å in the short (3×) periodicity direction, which is close to the size of 9 unit cells of the Ir(1 1 1) substrate. Together with the superstructure determined by the LEED patterns, it would seem that there are islands consisting of pentacene rows, and that these are, on average, 3 rows wide. In the long axis direction, the spot width is 1.5 times as large, giving an average ordered domain size of 17 Å, almost compatible with a single molecular length. The diffraction intensity visible near the (0,0) spot

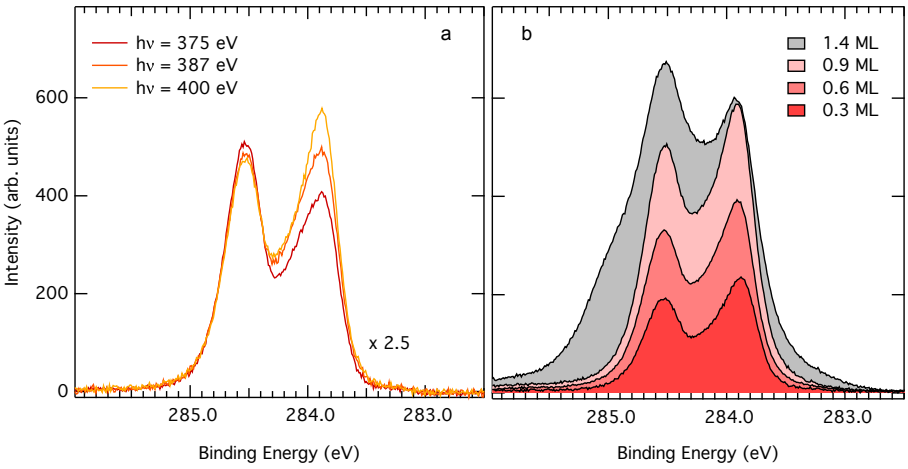

Figure 7.2: High resolution XPS references acquired (a) for 0.3 ML of pentacene at several different photon energies, normalized by the photoemission cross section with respect to the cross section at 400 eV of photon energy, and (b) for several coverages at $h\nu = 400$ eV.

(Fig. 7.1(d)) is similar to the typical streaks observed for Fourier transformed STM images of graphene nanoribbons on (1 1 1) surfaces, which are the result of thin islands just a few ribbons wide. Also in this case, the main diffraction spots are very wide in the short periodicity direction, due to the small number of ribbons that are placed side-by-side in single domains, on average. Streaks are observed in the Fourier transformed image, from the main spots to the origin. They are located at lower spatial frequency with respect to the main spots, and are associated to the finite size of the ordered islands or to holes in the adlayer, with typical sizes larger than the ribbon-ribbon distance. Also in our case, we can associate the diffraction intensity at low spacial frequencies to either islands or holes in the pentacene adlayer. The diffraction experiments,

therefore, give a strong indication that the surface is covered by a random close packed layer of pentacene molecules for coverages of 0.5 ML.

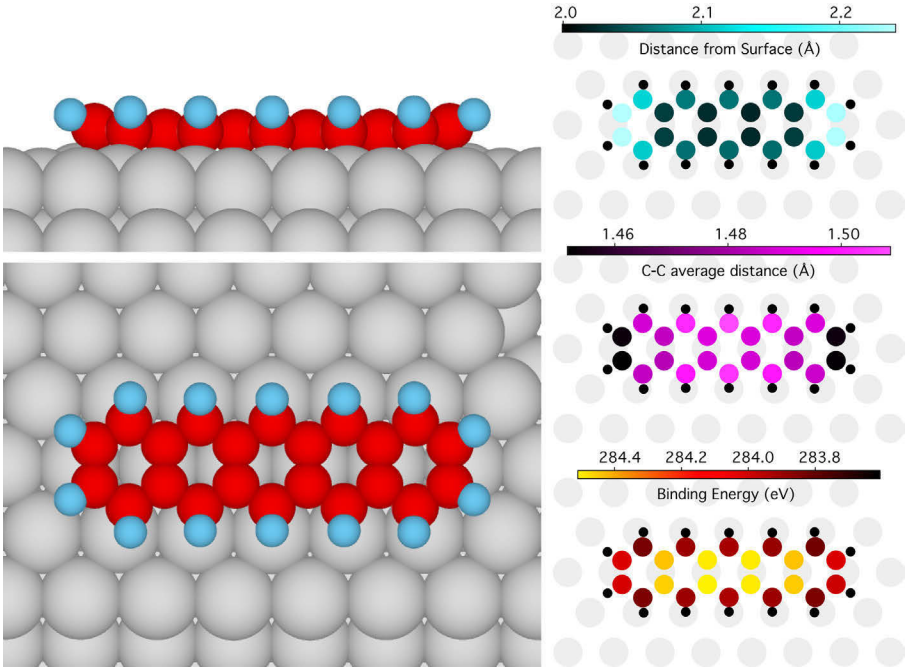

Figure 7.3: The relaxed structure for pentacene on Ir(1 1 1), as obtained by the DFT calculations. To the right, from the top to the bottom, the distance from the surface plane, the average C-C distance, and the calculated C 1*s* BE, are color coded for each ball model. H atoms are shown in black, Ir atoms in gray.

Next, high resolution XPS was employed in order to characterize the pristine pentacene molecules. The C 1*s* core level spectra have been acquired at several photon energies, in order to assess the effects of diffraction on the relative intensities of the individual components in the C 1*s* spectrum (see Fig. 7.2(a)). Indeed, there is an evident modulation, so that the photon energy of 400 eV was chosen for the experiments because it has the highest kinetic energy, minimizing back-scattering effects, while still having a large enough photoemission cross section. The two-peak line shape resembles that of pentacene in gas phase [28], although the spectral weights are inverted. In addition, C 1*s* spectra were measured at increasing pentacene coverages (see Fig. 7.2(b)), and show the same line shape regardless of the pentacene amount, suggesting that increasing molecular coverage does not influence the adsorption site and that the interaction with defects, such as step edges, is negligible even at the lower coverages like in the case of coronene (see Ch. 6). At coverages higher than 0.9 ML, shoulders start to appear at higher and lower BEs, indicating that a multilayer is starting to form. Also, these data show that before this coverage

a single molecular layer is present.

In order to interpret the XPS spectra, and to gain information on the pentacene adsorption geometry, we resorted once again to DFT calculations. DFT calculations were, at first, performed for isolated molecules. As a starting point for the relaxation, several different high-symmetry rotations were tested, as were several shifted configurations. The most stable structure was found to have the molecular axis aligned to a substrate crystallographic axis, and with the central aromatic ring centered on a substrate bridge position (see Fig. 7.3). The top and bottom C rows of the pentacene molecules are situated near top sites, while the two central rows form C bridges close to substrate top sites. The C atoms at the extremes are slightly raised away from the surface, giving a somewhat curved configuration (see Fig. 7.3, top). The bowl-shaped geometry that was present for coronene (see Ch. 6) is translated to a U-shape in this monodimensional polyaromatic molecule, and is again enhanced by the hydrogen atoms displaying an average height of 2.73 Å, 0.7 Å farther from the surface than the central C atoms. The C-C distance (see Fig. 7.3, middle) is always larger than the equivalent value for pentacene in isolated molecules [29], where the distances are smaller that 1.46 Å, and at the extremes even shorter than 1.43 Å. In our case, distances are stretched by at least 3%, implying a substrate-induced strain is present. Regarding the C 1*s* BEs (see Fig. 7.3, bottom), they can be divided in two families, so that C atoms on the periphery have a substantially lower BE, likely as a result of the bond with H.

A densely packed molecular layer was also simulated, with a 3×6 periodicity

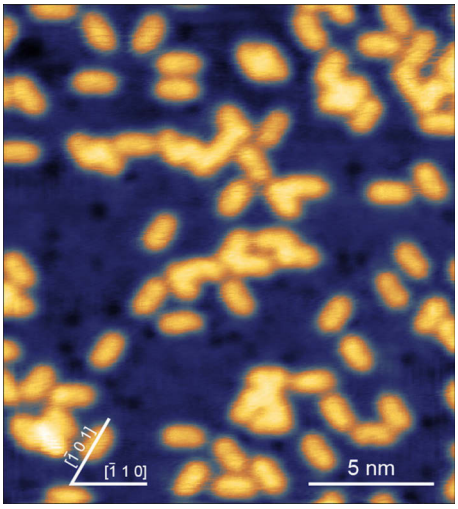

Figure 7.4: STM image of a pentacene adlayer on Ir(1 1 1). Scanning parameters were: tunneling voltage $V = -500\,\text{mV}$, tunneling current $I = 100\,\text{pA}$. The substrate crystallographic directions have been marked.

determined by LEED in the molecules' short axis direction, and determined by close packing in the long axis direction, so that 4 molecules would reside on the simulated slab. The results show that there is little change, both in adsorption configuration and C 1*s* BEs, confirming that the interaction between the molecules is less important than the interaction with the substrate. STM measurements performed for the adsorbed pentacene molecules (see Fig. 7.4) corroborate the DFT calculations and give a direct confirmation of the structure, showing that the molecular axes are aligned with the crystallographic directions, as predicted. Following the usual approach, we also compared in

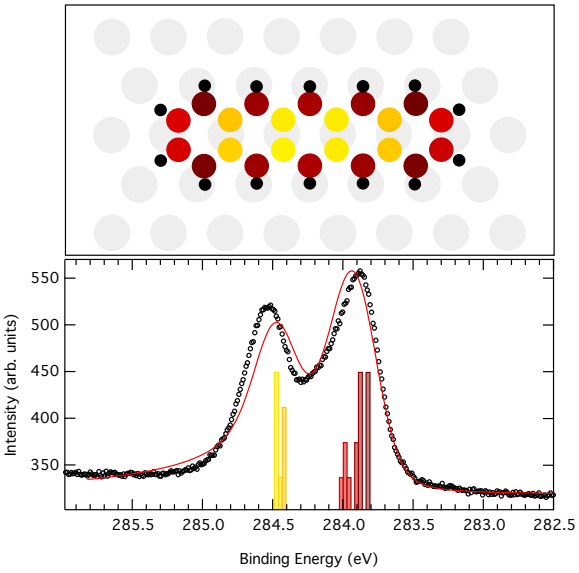

Figure 7.5: Results of the DFT for the C 1*s* BEs for all the carbon atoms in the relaxed pentacene molecule on Ir(1 1 1). In the lower part of the image, a high resolution C 1*s* spectrum obtained with photon energy $h\nu = 400\,\text{eV}$ after deposition of 0.75 ML (black markers) of pentacene has been fitted with DS functions with BEs given by the DFT calculations (red line). The histogram shows the distribution of the calculated BEs, and the color scale of the histogram reflects the color scale for the ball model in the upper part of the image.

Fig. 7.5(bottom) the experimental C 1*s* core level spectrum (black circles) to the DFT results by performing a fit (red line) that included 22 D-S functions (all with the same line shape, intensity, and relative BE shifts determined by DFT). The good agreement between experimental data and fit results further strongly supports the DFT calculated molecular adsorption geometry, including the adsorption site. Comparing the BE values to gas phase data, it becomes evident that the carbon atoms situated at the molecular extremes, when adsorbed on Ir, have a much lower C 1*s* BE with respect to the gas phase (by 400 meV). The other atoms behave in a similar manner, with internal atoms at high BE,

around 284.4 eV, and peripheral atoms at low BE, at 283.9 eV, resulting in a two peak distribution that, however, has inverted component weights in the two cases.

7.3 Results and Discussion: Dehydrogenation

TP-XPS experiments have been performed in order to understand the thermal dissociation process for pentacene on Ir(1 1 1) (see Fig. 7.6, center). The temperature evolution of the spectra shows that dissociation starts at 500 K, at which point the spectra rapidly settle to a shape that remains relatively unchanged up to 650 K, when it starts to gradually resemble the C_{54} spectrum in Ch. 6. Then, once 1000 K are reached, again the spectrum changes rapidly and the fingerprint of graphene formation is observed: a sharp peak at 284.4 eV emerges as the central component of the spectral distribution. A small shoulder in the C 1*s* graphene spectrum at higher BE is commonly identified as defects in graphene, but is completely absent in this case, indicating that high quality graphene is formed using pentacene as a precursor on this surface. Regarding the initial spectral modification at 500 K, the TPD spectra (see Fig. 7.6, left) show that the pentacene molecules are losing all the hydrogen atoms between 480 K and 560 K, indicating that this first observed spectral change corresponds to the dehydrogenation process. A discrepancy of about 30 K is observed for the temperature ranges for this reaction in TPD and TP-XPS, likely as a result of the different annealing rate.

In a second set of experiments, upon reaching selected temperatures, the annealing ramp was interrupted and the sample rapidly cooled to 300K, where HR-XPS spectra have been acquired for intermediate species (see Fig. 7.6, right). The spectra after annealing to 670 K, 870 K, and 1040 K have a similar spectral distribution to the DFT data from the C_{54} (see Ch. 6), indicating that very small graphene islands are starting to form already at such low temperatures, with the main graphene peak rising as the central component of the spectra compatible with carbon nanodomes of increasing size [30].

Since the transition observed by TP-XPS at 500 K seemed quite abrupt, a reasonable hypothesis to make was that the dissociation barrier for the first hydrogen is much higher than all the following, rendering the process equivalent to a single reaction. A simple way to test this is to generate an Arrhenius plot for the reaction, where a reaction rate is plotted against inverse temperature in a log-lin plot, giving an unambiguous way of determining the validity of this hypothesis. In fact, supposing a linear distribution of the data points is observed, a fit of the Arrhenius plot with a single exponential can yield both the barrier and the attempt frequency for a reaction, from which it is possible to make a simple but interesting consideration to interpret the results obtained from the TP-XPS measurements. If the spectral integrated intensity associated to a particular species A is proportional to the concentration of this species in the reaction A $\longrightarrow$ B (with only a single direction possible), then the

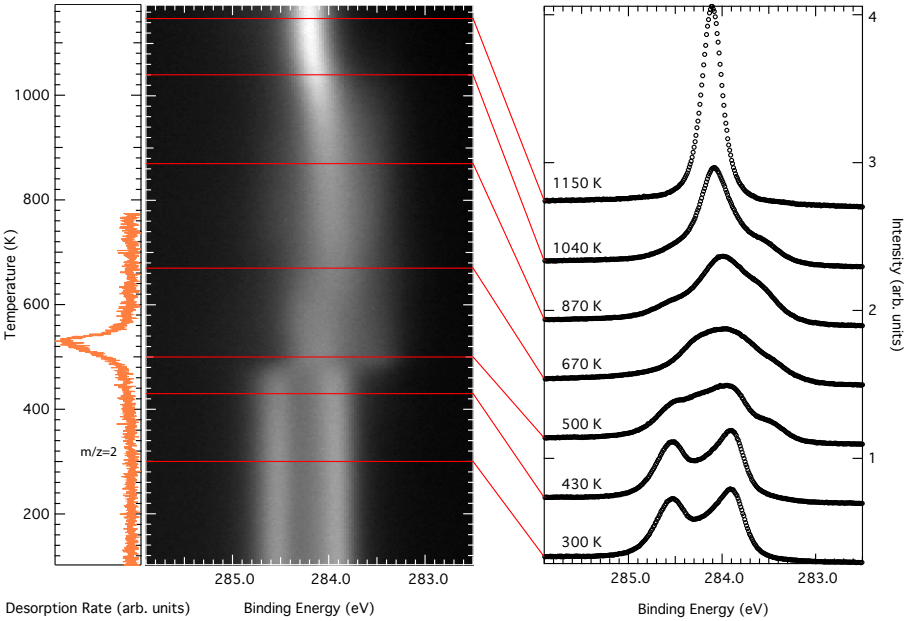

Figure 7.6: TP-XPS results for a temperature ramp at 0.25 K/s. On the left, a background subtracted TPD curve for $m/z = 2$ executed at a rate of 2.5 K/s shows the desorption rate of H_2 from the surface. In the image, each horizontal line is an XPS spectrum acquired *in situ* at a different annealing temperature. On the right, high resolution references acquired after annealing to selected temperatures and cooling to 77 K. All spectra were acquired with photon energy $h\nu = 400$ eV.

concentration of A on the surface obeys the differential equation

$$-\frac{d[\mathrm{A}]}{dt} = [\mathrm{A}] \cdot k \tag{7.1}$$

with k the reaction rate, which depends on the temperature T:

$$k = \nu e^{-\frac{E_{ab}}{k_B T}} \tag{7.2}$$

with ν the attempt frequency, E_{ab} the energy barrier for the reaction, k_B the Boltzmann constant. If the temperature is in a linear relationship with time, $T = r \cdot t$, then the differential equation becomes

$$-\frac{d[\mathrm{A}]}{dt} = [\mathrm{A}] \cdot \nu e^{-\frac{E_{ab}}{k_B r \cdot t}} \tag{7.3}$$

which has an analytic solution. Supposing the photoemission intensity I is proportional to the concentration of A, inverting for the temperature, and substituting T/r for the time, the observed photoemission intensity for the

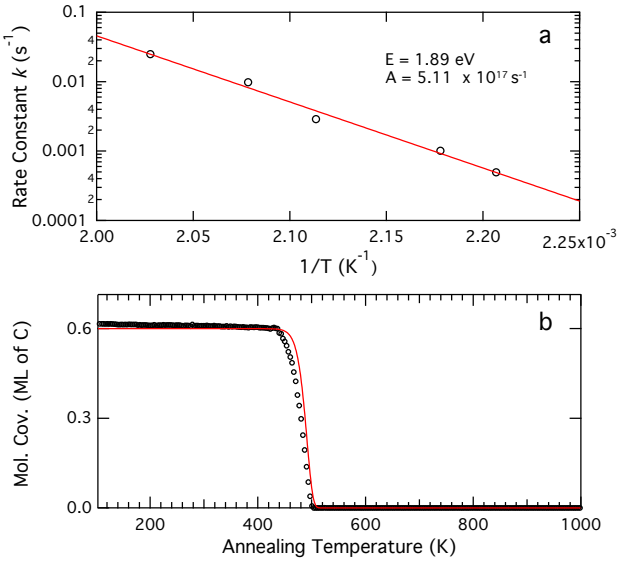

Figure 7.7: (a) Arrhenius plot obtained for the first step of the pentacene thermal dissociation reaction on Ir(1 1 1). The reaction rates (black markers) have been plotted as a function of inverse temperature in a log-lin plot. A fit with an exponential function is shown in red. In (b), the pristine pentacene coverage as obtained from fits of the TP-XPS spectra is plotted as a function of temperature (black markers) alongside a plot of the function in Eq. 7.4 (red line) using the parameters obtained from the Arrhenius plot and an annealing rate of 0.25 K/s.

pristine molecules can be described by

$$I = I_0 exp\left\{ \frac{\nu T}{r} e^{-\frac{E_{ab}}{k_B T}} - \frac{\nu E_{ab} Ei(-\frac{E_{ab}}{k_B T})}{r k_B} \right\} \tag{7.4}$$

with I_0 the initial intensity, and $Ei(x)$ the exponential integral function. Once the form of this equation is known, it is straightforward to compare the results obtained from the Arrhenius plot to the TP-XPS data.

For this reason, the necessary data to generate an Arrhenius plot has been acquired by following a straightforward approach. While acquiring real time XPS spectra, the sample was quickly brought to a selected temperature, chosen between 450 K and 500 K, by following a step-like temperature profile. Continuous XPS measurements were then carried out until pristine molecules were no longer detectable in the spectra. Next, the intensity of the pristine molecules was determined as a function of time by the fitting procedure described in Sec. 7.1. These curves represent the concentration of the pristine molecular species in the chemical reaction at fixed T, and therefore obey Eq. 7.1, with a fixed k. The rates k at the chosen temperatures was determined by fitting

these curves in the time interval that the temperature is constant. Finally, once the reaction rates have been measured as a function of temperature, they are plotted against inverse temperature on a logarithmic scale, and the Arrhenius plot is generated (see Fig. 7.7, top). Supposing the reaction rate is given by Eq. 7.2, and fitting this function to the data points, it is possible to find both the reaction barrier E_{ab} and the attempt frequency ν.

The observed values were, for the barrier $E_{ab} = 1.89\,\text{eV}$, and for the attempt frequency $\nu = 5.11 \times 10^{17}\,\text{s}^{-1}$. Furthermore, the good linearity of the resulting plot gives a strong indication that indeed the reaction rate depends on a single barrier. A plot of Eq. 7.4 inserting the two parameters that were found from the Arrhenius plot, it is possible to directly compare these data to the observed photoemission intensity for pentacene (see Fig. 7.7, bottom). Indeed, the temperature interval for the reaction and the evolution of the intensities is strikingly similar. Furthermore, it is possible to evaluate that a rate 10 times higher, namely the rate used for the TPD experiment, shifts the reaction curve by 30 K to lower temperatures, explaining the small discrepancy between these measurements and the TP-XPS curves. This would place the end of hydrogen desorption at 530 K, in agreement with the XPS spectra that at 530 K are identical to the spectra at 600 K, where the TPD curves show unambiguously that no more hydrogen is present on the surface.

Next, we tested annealing the pentacene covered surface (0.6 ML) in a hydrogen atmosphere ($P = 5 \times 10^{-7}\,\text{mbar}$). If the ramp is stopped at 520 K and the sample rapidly quenched to 420 K, the spectra have been observed to mostly return to the original configuration after the expected change above 500 K (see Fig. 7.8(a,b)). This process has been observed to be reproducible for a few times, even though every time the reforming of pentacene molecules is about 80% efficient, with spectra showing a slightly shallower minimum in between the two main components associated to pentacene. We interpreted this as an almost complete rehydrogenation, after complete dehydrogenation of the individual pentacene molecules. In fact, even though some residual hydrogen is desorbing from the surface at these temperatures, and even though the spectra are still changing for 10 K above this temperature (in agreement with the TDP data after correcting for the different rate), the individual molecules that have lost hydrogens should have already overcome all the reaction barriers, and be completely dehydrogenated. The single barrier hypothesis, in fact, is confirmed by the linearity observed in the Arrhenius plot and by the agreement of the evolution of the pristine pentacene molecules as a function of temperature with Eq. 7.4: residual hydrogen will come from still intact pentacene molecules that dehydrogenate completely in a single step.

There exist a few possible explanations to the incomplete rehydrogenation observed. In the first, the molecules might sinter and start forming for example small nanodomes. This is unlikely, since the spectra reveal a shape compatible with nanodomes only at higher temperatures, but they might still be forming dimers or longer n-mers, generating spaghetti-like structures like in the case of pentacene on Ni(1 1 1) [31]. A small number of intact molecules might prevent

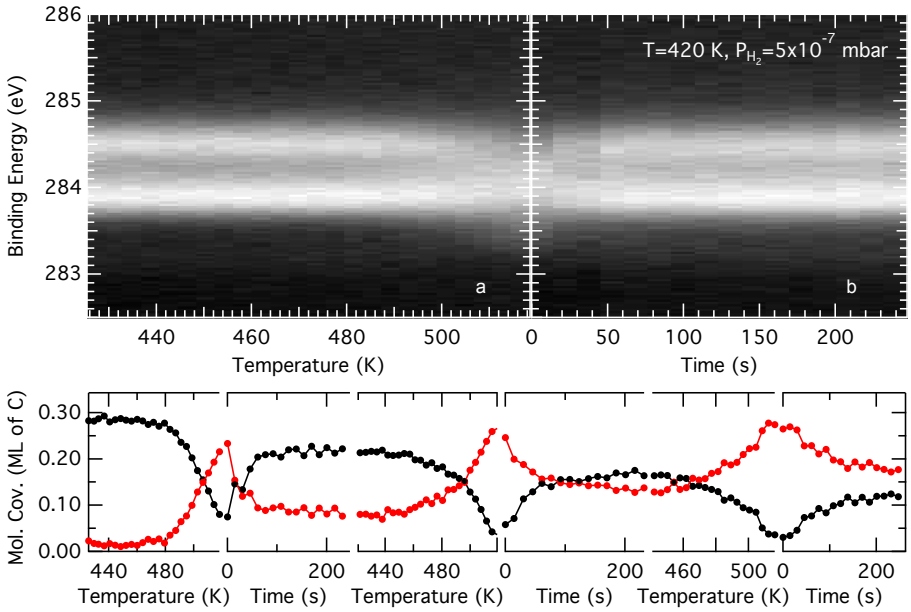

Figure 7.8: (a) A TP-XPS experiment performed with photon energy $h\nu = 400\,\text{eV}$ for 0.3 ML of pentacene at 0.25 K/s, abruptly interrupted at 520 K. (b) A Hydrogen uptake experiment, performed at 420 K, for the dissociated pentacene molecules. The bottom graph shows several sequential plots of the intensities of pentacene (black) and dissociated pentacene (red) during 3 dehydrogenation/rehydrogenation cycles, the first of which is shown in (a,b).

this sintering, and experiments with coadsorbed layers with other molecules with different dehydrogenation temperatures could prove this hypothesis. A second explanation might be that, upon losing the hydrogen atoms, the molecules move a little with respect to their original positions, since the hydrogens are not keeping them apart. The XPS spectra might not change, since the interaction with the substrate could still be the leading factor in determining the spectral lineshape, but the free surface between the molecules would not be large enough for hydrogen dissociative adsorption and diffusion to favorable sites. Hydrogen atoms necessary for the rehydrogenation would not be available close to the molecules, which could be a crucial requirement for rehydrogenation, since the surface residence time of atomic hydrogen on the hot Ir surface is very small, and the dissociative H adsorption process would have to happen very close to the molecules in order for the rehydrogenation reaction to take place.

7.4 Conclusions

Pentacene single layers have been characterized by multiple spectroscopic and electron diffraction techniques, with the fundamental aid of DFT calculations that have been directly confirmed by STM measurements. The adsorption geometry for pentacene on Ir(1 1 1) was found to be almost flat, displaying only a slight U-shaped configuration, the molecular axis being oriented along the substrate's crystallographic axes, with the central aromatic ring adsorbed in a bridge position. The molecules were found to have an average lateral distance of around 3 substrate unit cells, as determined by LEED, and the side-by-side rows were found to be, on average, 3 molecules wide. Also, the molecules were found to form single adlayers before starting to form the second layer for coverages higher than about 0.9 ML. For the single adlayers, coverage was found to have little effect on the XPS spectra, both in the DFT calculations and experimentally.

Next, the thermal dehydrogenation of pentacene on Ir(1 1 1) has been characterized by TP-XPS during a temperature ramp from 100 K to 1280 K, where the formation of very high quality graphene is observed. High resolution XPS references for selected annealing temperatures have also been acquired. The dehydrogenation was found to happen between 450 K and 550 K, as confirmed by TPD measurements for $m/z = 2$. The experiments reveal that the dehydrogenation process is compatible with a single reaction barrier, as confirmed by the abrupt change in the XPS spectra as a function of temperature in correspondence of the TPD peak. The spectra acquired after annealing to temperatures higher than 670 K strongly resemble carbon nanodomes of increasing size. Also, an Arrhenius plot has been acquired, and it displays an excellent linearity, confirming the thermal dehydrogenation process is equivalent to a single reaction. Furthermore, the parameters extracted from the plot, together with the solution of a simple differential equation with the assumptions that only a single barrier exists, give an excellent description of the observed quantity of pristine pentacene on the surface as a function of temperature.

Finally, a novel phenomenon was observed. After dehydrogenation of the pristine pentacene adlayer, and upon cooling the sample in a H_2 atmosphere ($P = 5 \times 10^{-7}$ mbar), it was possible determine by real time XPS measurements that the molecules were dehydrogenated and rehydrogenated in up to 3 cycles. This has interesting applications for the understanding of the fundamental properties of graphene nanoribbons, that to date have been prevalently synthesized in a hydrogen capped form. Graphene nanoribbons are predicted to have higher mobilities and better thermal transport when dehydrogenated, so that this reaction also has interesting technological applications: the thermal switching capabilities of nanoribbons might be of interest. Furthermore, the electronic structure of individual pentacene molecules might allow for a similar switching application, where the molecules' HOMO-LUMO gap is switched between different values.

References

[1] Son, Y.-W.; Cohen, M. L.; Louie, S. G. Energy Gaps in Graphene Nanoribbons. *Physical Review Letters* **2006**, *97*, 216803.

[2] Wang, Z. F.; Li, Q.; Zheng, H.; Ren, H.; Su, H.; Shi, Q. W.; Chen, J. Tuning the electronic structure of graphene nanoribbons through chemical edge modification: A theoretical study. *Physical Review B* **2007**, *75*, 113406.

[3] Yang, L.; Park, C.-H.; Son, Y.-W.; Cohen, M. L.; Louie, S. G. Quasiparticle Energies and Band Gaps in Graphene Nanoribbons. *Physical Review Letters* **2007**, *99*, 186801.

[4] Cai, J.; Ruffieux, P.; Jaafar, R.; Bieri, M.; Braun, T.; Blankenburg, S.; Muoth, M.; Seitsonen, A. P.; Saleh, M.; Feng, X.; Müllen, K.; Fasel, R. Atomically precise bottom-up fabrication of graphene nanoribbons. *Nature* **2010**, *466*, 470.

[5] Zhang, H.; Lin, H.; Sun, K.; Chen, L.; Zagranyarski, Y.; Aghdassi, N.; Duhm, S.; Li, Q.; Zhong, D.; Li, Y.; Müllen, K.; Fuchs, H.; Chi, L. On-Surface Synthesis of Rylene-Type Graphene Nanoribbons. *Journal of the American Chemical Society* **2015**, *137*, 4022.

[6] Li, X.; Wang, X.; Zhang, L.; Lee, S.; Dai, H. Chemically Derived, Ultrasmooth Graphene Nanoribbon Semiconductors. *Science* **2008**, *319*, 1229.

[7] Ritter, K. A.; Lyding, J. W. The influence of edge structure on the electronic properties of graphene quantum dots and nanoribbons. *Nature Materials* **2009**, *8*, 235.

[8] Wang, S.; Talirz, L.; Pignedoli, C. A.; Feng, X.; Müllen, K.; Fasel, R.; Ruffieux, P. Giant edge state splitting at atomically precise graphene zigzag edges. *Nature Communications* **2016**, *7*, 11507.

[9] Yoon, Y.; Guo, J. Effect of edge roughness in graphene nanoribbon transistors. *Applied Physics Letters* **2007**, *91*, 073103.

[10] Ruffieux, P.; Cai, J.; Plumb, N. C.; Patthey, L.; Prezzi, D.; Ferretti, A.; Molinari, E.; Feng, X.; Müllen, K.; Pignedoli, C. A.; Fasel, R. Electronic Structure of Atomically Precise Graphene Nanoribbons. *ACS Nano* **2012**, *6*, 6930.

[11] Chen, Y.-C.; de Oteyza, D. G.; Pedramrazi, Z.; Chen, C.; Fischer, F. R.; Crommie, M. F. Tuning the Band Gap of Graphene Nanoribbons Synthesized from Molecular Precursors. *ACS Nano* **2013**, *7*, 6123.

[12] Zhang, X.; Yazyev, O. V.; Feng, J.; Xie, L.; Tao, C.; Chen, Y.-C.; Jiao, L.; Pedramrazi, Z.; Zettl, A.; Louie, S. G.; Dai, H.; Crommie, M. F. Experimentally Engineering the Edge Termination of Graphene Nanoribbons. *ACS Nano* **2013**, *7*, 198.

[13] Han, M. Y.; Özyilmaz, B.; Zhang, Y.; Kim, P. Energy Band-Gap Engineering of Graphene Nanoribbons. *Physical Review Letters* **2007**, *98*, 206805.

[14] Wang, G. Effect of edge-hydrogen passivation and saturation on the carrier mobility of armchair graphene nanoribbons. *Chemical Physics Letters* **2012**, *533*, 74.

[15] Evans, W. J.; Hu, L.; Keblinski, P. Thermal conductivity of graphene ribbons from equilibrium molecular dynamics: Effect of ribbon width, edge roughness, and hydrogen termination. *Applied Physics Letters* **2010**, *96*, 203112.

[16] Tozzini, V.; Pellegrini, V. Prospects for hydrogen storage in graphene. *Physical Chemistry Chemical Physics* **2013**, *15*, 80.

[17] Sofo, J. O.; Chaudhari, A. S.; Barber, G. D. Graphane: A two-dimensional hydrocarbon. *Physical Review B* **2007**, *75*, 153401.

[18] Elias, D. C.; Nair, R. R.; Mohiuddin, T. M. G.; Morozov, S. V.; Blake, P.; Halsall, M. P.; Ferrari, A. C.; Boukhvalov, D. W.; Katsnelson, M. I.; Geim, A. K.; Novoselov, K. S. Control of Graphene's Properties by Reversible Hydrogenation: Evidence for Graphane. *Science* **2009**, *323*, 610.

[19] Zhao, W.; Gebhardt, J.; Späth, F.; Gotterbarm, K.; Gleichweit, C.; Steinrück, H.-P.; Görling, A.; Papp, C. Reversible Hydrogenation of Graphene on Ni(1 1 1)—Synthesis of "Graphone". *Chemistry – A European Journal* **2015**, *21*, 3347.

[20] Target Explanation Document: Onboard Hydrogen Storage for Light-duty Fuel Cell Vehicles. *US Department of Energy Technical report* **2015**,

[21] Lin, Y. Y.; Gundlach, D. J.; Nelson, S. F.; Jackson, T. N. Stacked pentacene layer organic thin-film transistors with improved characteristics. *IEEE Electron Device Letters* **1997**, *18*, 606.

[22] Dimitrakopoulos, C.; Malenfant, P. Organic Thin Film Transistors for Large Area Electronics. *Advanced Materials* **2002**, *14*, 99.

[23] Karl, N. Charge carrier transport in organic semiconductors. *Synthetic Metals* **2003**, *133–134*, 649.

[24] Yamashita, Y. Organic semiconductors for organic field-effect transistors. *Science and Technology of Advanced Materials* **2009**, *10*, 024313.

[25] Wang, G.; Luo, Y.; Beton, P. H. High mobility organic transistors fabricated from single pentacene microcrystals grown on a polymer film. *Applied Physics Letters* **2003**, *83*, 3108.

[26] Pietzsch, O.; Kubetzka, A.; Haude, D.; Bode, M.; Wiesendanger, R. A low-temperature ultrahigh vacuum scanning tunneling microscope with a split-coil magnet and a rotary motion stepper motor for high spatial resolution studies of surface magnetism. *Review of Scientific Instruments* **2000**, *71*, 424.

[27] Simonov, K. A.; Vinogradov, N. A.; Vinogradov, A. S.; Generalov, A. V.; Zagrebina, E. M.; Mårtensson, N.; Cafolla, A. A.; Carpy, T.; Cunniffe, J. P.; Preobrajenski, A. B. Effect of Substrate Chemistry on the Bottom-Up Fabrication of Graphene Nanoribbons: Combined Core-Level Spectroscopy and STM Study. *The Journal of Physical Chemistry C* **2014**, *118*, 12532.

[28] Baldacchini, C.; Mariani, C.; Betti, M. G. Adsorption of pentacene on filled d-band metal surfaces: Long-range ordering and adsorption energy. *The Journal of Chemical Physics* **2006**, *124*, 154702.

[29] Endres, R.; Fong, C.; Yang, L.; Witte, G.; Wöll, C. Structural and electronic properties of pentacene molecule and molecular pentacene solid. *Computational Materials Science* **2004**, *29*, 362.

[30] Lacovig, P.; Pozzo, M.; Alfè, D.; Vilmercati, P.; Baraldi, A.; Lizzit, S. Growth of Dome-Shaped Carbon Nanoislands on Ir(1 1 1): The Intermediate between Carbidic Clusters and Quasi-Free-Standing Graphene. *Physical Review Letters* **2009**, *103*, 166101.

[31] Dinca, L. E.; De Marchi, F.; MacLeod, J. M.; Lipton-Duffin, J.; Gatti, R.; Ma, D.; Perepichka, D. F.; Rosei, F. Pentacene on Ni(1 1 1): room-temperature molecular packing and temperature-activated conversion to graphene. *Nanoscale* **2015**, *7*, 3263.

Chapter 8

Commissioning of a size-selected nanocluster source

Clusters of atoms are objects that have been exploited in technology since ancient times, for example Au nanoparticles in ruby glass [1, 2]. More recently, technology has allowed for unprecedented manipulation of matter, and nanoclusters have become of great interest in many fields of science, beginning from catalysis [3], where they can be exploited for fuel cells [4], for photochemistry [5], or for chemical sensors [6], for example. Further important applications include optoelectronics [7, 8] and even medicine [9]. However, one of the greatest challenges that still remain in nanocluster science is a method of producing clusters that are all alike. In fact, when dealing with clusters, they behave for many aspects like very large molecules: some properties are smoothly scalable, mainly those related to the fraction of atoms at the surface. Others, which depend on quantum effects, display discontinuous behavior due to completion of shells in systems with delocalized electrons [10]. For this reason, the number of atoms the nanoclusters are made of, when they are very small (less than 100 atoms), can greatly affect their characteristics: structural, physical, and chemical properties are all known to be dramatically size-dependent [11–14].

In view of the work presented in this thesis, these objects are of great interest for example in the case of carbon nanoclusters, where small clusters made up by a handful of C atoms can be deposited on transition metal surfaces, like Ir(1 1 1), so that the initial stages of graphene nucleation can be studied. Other applications might be on the graphene/Ru(1 0 $\bar{1}$ 0) system, where noble metal clusters can be tailored to fit in the one dimensional moiré that forms when graphene is grown on the surface, and have the potential of forming new long range ordered nanostructures. Moreover, clusters of a fixed amount of C atoms with specific shapes might be used to directly grow new nanostructures on this surface, in a similar approach to [15], where the Ullmann reaction is exploited

for the growth of graphene nanoribbons, but exploiting nanocluster equality and substrate anisotropy instead of molecular dehalogenation.

Regarding the study of the nanoclusters themselves, much progress has been made in nanocluster isolation with methods that are UHV compatible, which is an important prerequisite for efficient, surface science compatible generation methods. In this way, the cluster's properties are preserved, undisturbed by the harshness of ambient conditions on these sometimes very reactive structures. Furthermore, in UHV conditions it is possible to soft-land the intact nanoclusters on inert substrates that help in inhibiting their sinterization, one of the main issues that has hindered research on many types of clusters. For example, a very successful sinter-resistant method relies on soft landing the nanoclusters on graphene moiré superstructures that form on (1 1 1) transition metal surfaces [16, 17]. Another focus of research is currently on finding new ways of fabricating clusters that are mono-dispersed. This is a critical point, because many cutting-edge techniques that are applied in surface science, like synchrotron based photoelectron spectroscopies, give space averaged information. This is an intrinsic limit that many non-local probes have, and they give data that are very difficult to interpret when a distribution of cluster sizes is present on the sample.

Supersonic beam expansion in vacuum has proven to be a reliable way of obtaining nanoclusters from metal vapors or from precursor solutions, and most modern UHV compatible nanocluster generation techniques rely on this key step. In any case, a few methods have been developed and successfully applied for mono-dispersed nanocluster creation, like the conventional "bottom-up" chemistry based approaches that exploit transition metal precursors for the creation of functionalized metal nanoclusters, by which a handful of cluster types can be synthesized, like in the case Au_{25} [18] or Au_{54} [19]. Electrospray ionization is a cheap and reliable evolution of these methods, and allows the production of large fluxes of clusters in UHV conditions [20]. In this technique, a solution of the cluster precursors flows through a capillary where a strong electric field is present. Charges build up in the solution, and electrostatic repulsion eventually counteracts the surface tension close to the nozzle tip, stretching the liquid meniscus at the end of the capillary. At a critical voltage, a stream of liquid erupts from the surface in a point known as the Taylor cone: electrostatic repulsion prevails and the solution is ejected in vacuum. In this way, the material can be electrosprayed through a buffer gas that undergoes supersonic beam expansion into a vacuum chamber, causing the precursors to form the mono-dispersed metal clusters. This technique, however, is limited to those clusters for which stable precursor solutions can be obtained and electrosprayed, and therefore suffers from similar limitations to the conventional "bottom-up" approach. Other approaches, best suited to high melting point metals, typically rely on vaporization or sputtering techniques. Metal vapors are collected by a stream of inert gas, such as helium, that undergoes supersonic expansion causing the clusterization to happen. A widely used such technique consists in using magnetron sputtering to create a metal plasma that is ejected

from the target into the noble gas atmosphere, where clusterization occurs again because of supersonic jet expansion [21]. The drawback of this approach is that it presents difficulties when dealing with ferromagnetic materials

Laser ablation of target elements, on the other hand, is a very versatile and reliable approach that allows for the creation of plasmas of most elements. After plasma generation, the carrier gas, like in the other cases, transports the charged particles and forms the clusters through supersonic jet expansion. Pioneering machines of this kind have been developed by Smalley [22] and Maruyama [23], and more recently, important advances have been made by the Heitz group [24, 25]. Due to their flexibility and reliability, these machines have already been used in a number of cluster deposition experiments on transition metals and insulating substrates [26–29].

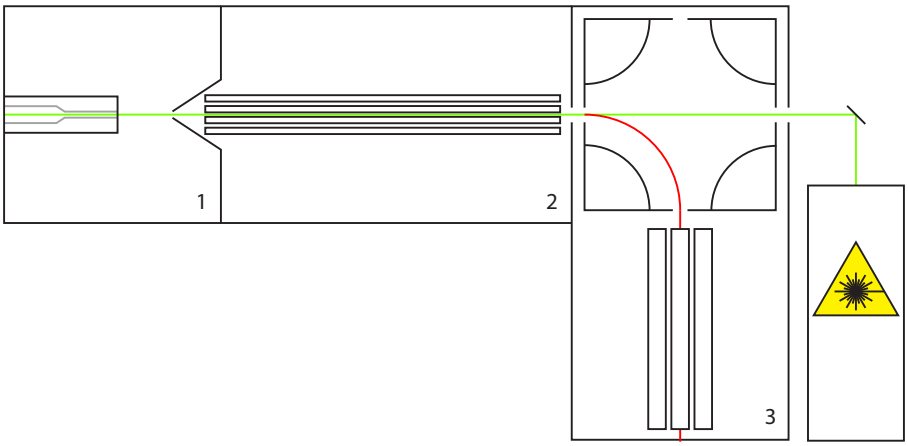

Figure 8.1: Schematic view of the size-selected nanocluster source. The laser beam path is marked in green, while the positively charged clusters' path is marked in red. In sections 1 and 2, the paths overlap. In section 1, the cluster are generated by supersonic expansion in a specially shaped nozzle. In section 2, after being skimmed from the zone of silence of the free expansion jet, the beam is transported to a region of better vacuum by using an RF octupole ion guide. In region 3, cluster selection happens by passing through an electrostatic bender and a quadrupole mass spectrometer. Electrostatic lenses present in the actual setup are not shown in this schematic.

Alongside my research activity, a significant portion of my work was dedicated to the setup of such a laser ablation size-selected nanocluster source that is currently operational as a stand-alone machine in the Surface Science Laboratory at Elettra. Although this machine has not been used in any of the experiments described in the previous chapters, its development has been an important part of my PhD project, and it will be described in this chapter.

The design is based on the one developed by Heiz and coworkers [24, 25]: this machine can be schematically divided in several sections (see Fig. 8.1),

in the first of which the clusters are generated. Laser ablation of a suitable target and supersonic jet expansion of helium generate the clusters inside a specially shaped nozzle. At the nozzle exit, the clusters are basically already formed with a tight dispersion in mass that depends on many parameters that determine the generation characteristics. The rest of the machine is dedicated to cluster transport towards regions of increasingly better vacuum, and cluster selection: after cluster generation, the clusters are transported through a differential pumping stage by exploiting an octupole ion guide in the second section. In the third section, the clusters are selected in charge after passing through an electrostatic bender. For mass selection, in fact, a specific charge sign is necessary, so the particles are first discriminated according to their charge. Then, an Extrel 16 000 u quadrupole mass spectrometer (QMS) filters out all the clusters except the ones with the wanted m/z ratio. Finally, the clusters can be soft landed in the deposition stage. Future plans for this nanocluster machine include attaching it to the experimental chamber of the surface science laboratory, and eventually to the SuperESCA end-station, so that *in situ* experiments can be carried out on the beamline, rendering the setup unique. For an overview of the nanocluster source we have developed, see Fig. 8.2.

8.1 Cluster Generation

Ablation of the target material is, as discussed, the first step in the cluster generation process. The laser-generated plasma is the feedstock of the clusters that will be formed, and it is created by using a focused Nd:YAG laser with second harmonic generation (light wavelength is 532 nm). The laser pulses that hit the target last 7 ns, and the pulse energy is tunable between 3 mJ and 140 mJ, allowing to change the amount of metal vapors that are produced in each cycle; the repetition rate is 120 Hz, and the spot on the target is less than 1 mm across. This is achieved by using a convex lens with a 1200 mm focal length. The beam enters the machine still unfocused through a fused silica window placed 1 m away from the focal plane, so that the spot size on the window is roughly 7 mm across. Fused silica is more resistant than ordinary glass to the thermal stresses induced by the laser pulses, which are problematic even when the beam is unfocused. Next, considering the ablation target, it needs to move constantly, so that the ablation is carried out uniformly, without excessively damaging spots on the target. In some designs, this is achieved by rotating a target rod on its longitudinal axis while moving it back and forth along the same axis, similar to a fishing reel. In our case, however, a metal disk is placed perpendicular to the laser axis, and it is moved on a cycloidal path. This method achieves similar results, but with the added benefit of accommodating slight misalignments better than the rod geometry. Furthermore, it is technically easier and cheaper to remelt partially used targets or metal pellets in disk shapes with high engineering tolerances. The plasma created this way expands inside a specially formed nozzle, consisting of a larger thermalization chamber

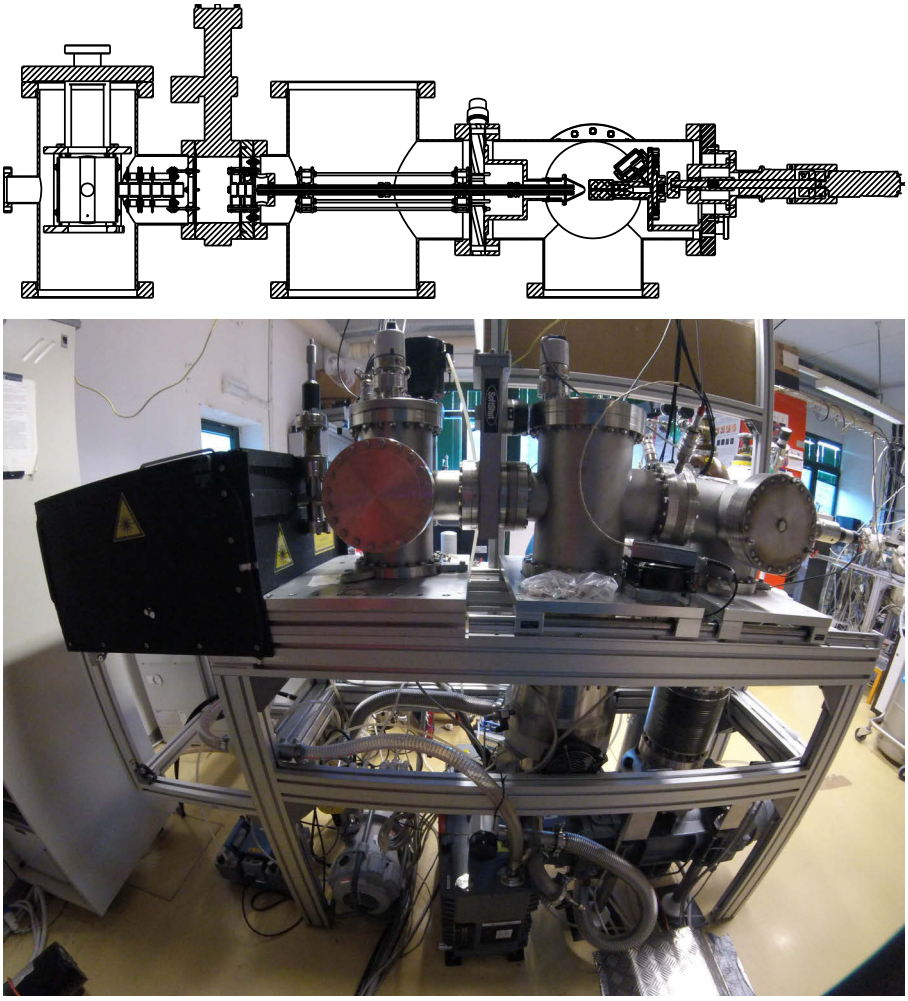

Figure 8.2: Overview of the nanocluster source from the back side. At the top, a cross section reveals all internal components up to the bender. At the bottom, all 3 stages are visible together with the pumping systems. In the left part of the image, the laser optics box, which allows for safe operation without eye protection whilst the laser is operational, is visible.

that tapers to a smaller tube where supersonic expansion of the carrier gas happens in a constrained environment (see Fig. 8.3,(b)). This is achieved by injecting the carrier He gas through an opening close to where the metal plasma is generated [30]. Thermalization of the hot laser-generated plasma happens by energy transfer to the nozzle inner walls through the carrier gas, and gives a much narrower final kinetic energy distribution. Furthermore, the

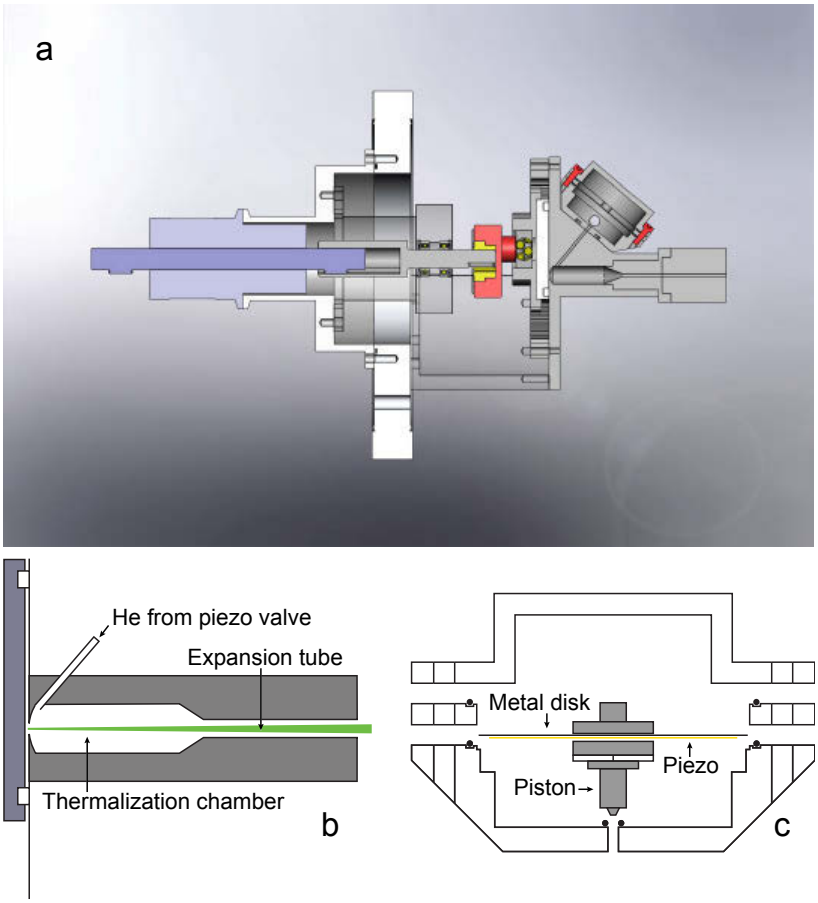

Figure 8.3: The heart of the nanocluster source. In (a), a cross section shows, from left to right, the mechanical system used to move the target on the cycloidal path within the vacuum chamber, the piezoelectric valve used for the generation of the He jets, and the nozzle. In (b), a schematic view of the nozzle shows the large thermalization chamber and the narrower expansion tube. In (c), an exploded view of the piezo valve.

special geometry allows for this thermalization to happen without excessive condensation on the nozzle walls.

The piezoelectric valve necessary for generating the He pulses was completely developed in-house. A piezoelectric ceramic disk bonded to a stainless steel diaphragm with conductive epoxy glue is subject to voltage pulses, of the order of $-400\,\mathrm{V}$, in the axial direction. The piezo disk shrinks in the radial direction, causing the metal diaphragm to bend upwards and actuating a small piston that acts as a needle valve (see Fig. 8.3(c)). The voltage pulse is antic-

ipated with respect to the laser pulse, so that the the carrier gas has enough time to travel, through a tube, from the valve to the nozzle.

Going back to the mixed and thermalized carrier gas/plasma mixture inside the thermalization chamber, it will be pushed forward towards the tapered end, where it will expand in a thin, long expansion tube, carrying the metal plasma outside the nozzle. Within this tube, where most of the clusters are created, the nucleation and growth phase of the supersonic expansion develops. In a naïve approach, one can consider adiabatic cooling as the cause of the condensation of the ablated vapors in few-atom clusters. However, a quantitative evaluation of this process is quite complicated, since the system has been brought far away from equilibrium by the extreme conditions present during supersonic expansion [31]. The observed tight dispersion in mass of the resulting clusters strongly depends on the generation parameters, like the amount of plasma generated (laser pulse energy), the duration of the He pulse, the backing pressure that causes the supersonic expansion (between 3 bar and 10 bar), the expansion tube shape [24], and temperature of the carrier gas (in our case, it is cooled to 77 K before entering the piezo valve).

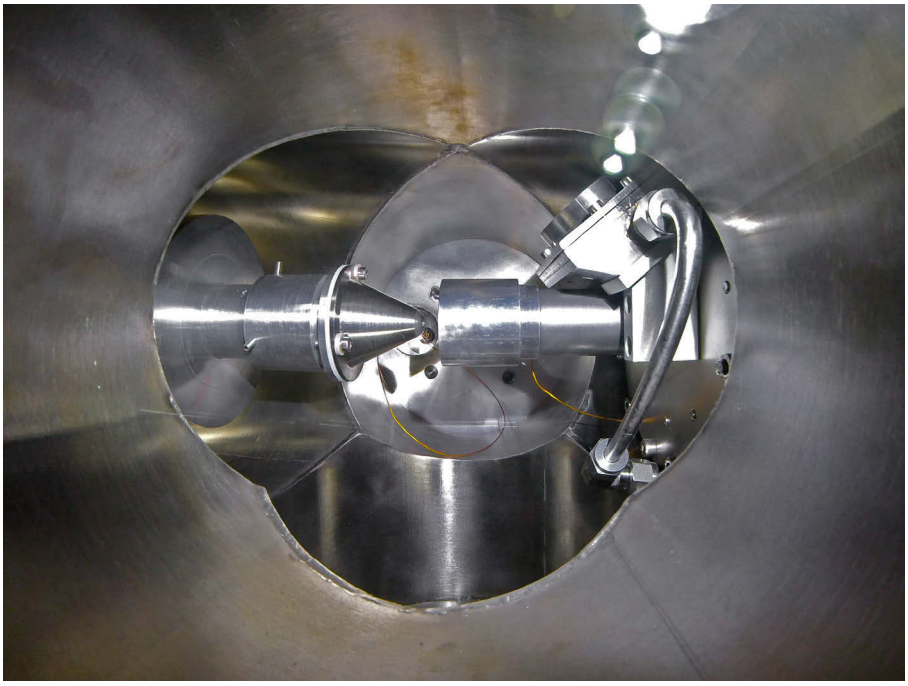

Figure 8.4: From the viewport of the first stage it is possible to see, from right to left, the piezo valve with the vacuum-tight tubes used to carry the He; the nozzle, which is removable so that different geometries can be tested; the skimmer, which is electrically isolated so that total cluster production can be measured.

The generated clusters finally exit the expansion chamber through the nozzle together with the carrier gas. Here, the supersonic expansion continues unguided by an expansion chamber tube, and the supersonic free jet can fully develop with a zone of silence, where most of the particles contained within are moving in linear trajectories without colliding with each other, and possess a narrow kinetic energy distribution. The zone of silence is bound to the sides by a barrel shock, and to the front by a Mach disk [32]. If a conical skimmer is placed within the zone of silence, piercing the Mach disk, a cluster beam is formed behind it, in a section with better vacuum. With this technique, it is possible to effectively isolate the expansion chamber, where a rough vacuum (about 10^{-1} mbar at maximum operation capacity) can be maintained by a fast pumping system, from a high vacuum chamber (pressure of 10^{-4} mbar at maximum operation capacity), in this way creating an effective first differential pumping stage with 3 orders of magnitude of pressure differential.

In order to enable supersonic jet expansion with a well developed zone of silence, large enough for the skimmer to be completely contained within, it is necessary to keep a pressure in the first section of the order of 10^{-1} mbar during the He pressure pulses. This is the only constrain to the pressure of the first chamber, since the barrel shock protects the cluster beam from contamination of residual gas in this first vacuum chamber. However, the barrel shock shrinks with increasing external pressure, to the point where the skimmer is not in the zone of silence any longer, hence the pressure constrain. Further improvements in pressure during operation beyond this constrain will not dramatically affect the base pressure in the following sections. However, since the He pulses happen at the same frequency as the laser pulses (120 Hz), it is necessary to have a very high pumping speed in this pressure range to keep the skimmer in the zone of silence. Furthermore, the faster the pumping speed at 10^{-1} mbar in this section, the more He can be injected with each pulse while still keeping the skimmer within the zone of silence. One of the fastest vacuum pumps in this pressure range are Roots blowers, and this is what is employed in this first section: an Alcatel 1500 m^3/h Roots pump is directly attached to the chamber, and is pre-pumped by a double stage 80 m^3/h Edwards rotary vane pump.

8.2 Cluster Transport

In order to efficiently work with the clusters in UHV conditions, without them being contaminated shortly after deposition, a differential pumping system is a fundamental requirement. The second chamber is dedicated to such a differential pumping system. Here, a 600 m^3/h Pfeiffer turbomolecular pump is pre-pumped by a 28 m^3/h Varian Triscroll pump that keeps the pressure at 10^{-4} mbar during cluster production. The base pressure is 10^{-8} mbar, so that the vast majority of the gas pressure during cluster production is given by inert He. A small orifice separates this chamber from the following sections, where a series of additional differential pumping stages are present. However, the large

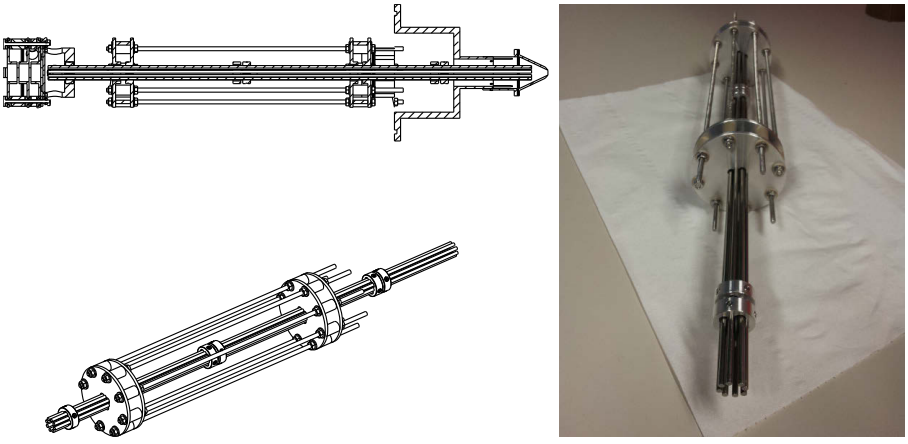

Figure 8.5: The 500 mm transport octupole. The technical drawing in the top left of the image shows its placement right behind the skimmer, and right before a conventional 3-element Einzel lens used for beam refocusing after the octupole.

part of the differential pumping happens in this section. A radio frequency (RF) octupole guides the charged clusters from just behind the skimmer hole to an Einzel lens and to the small orifice that leads to the third section. This octupole ion guide, in analogy with photon optics, acts as an optical fiber for charged particles. In fact, a fast alternating RF voltage is applied to alternating bars of the octupole, so that 4 bars are always oscillating in counter phase with the other 4.

When describing the motion of charged particles through multipole ion guides, it is often possible to consider an effective centrosymmetric potential

$$V^* = 4\frac{q^2V_0^2}{m\omega^2 r_0^2}r^6 \tag{8.1}$$

That keeps the ions within the guide. However, for this approximation to apply, some safe (sufficient, not necessary) operating conditions are generally taken into account [33]. First of all, the lateral energy of the charged particles should not be so large that positions too close to the bars are reached. Here, the effective potential approximation is no longer valid, and the motions can become unstable. The condition normally required is that the maximum turning radius $r_m < 0.8$, where the radius has been normalized to the characteristic radius r_0 (the radius of a cylinder inscribed in the octupole bars). This can actually be seen as a constrain on maximum transverse energy. The second requirement for safe operation is adiabaticity. This is defined as the possibility of separating the motions of the ions induced by the RF field in fast and secular motions. The adiabaticity parameter η is defined, for an octupole, as

$$\eta = 24\frac{qV_0}{m\omega^2 r_0^2}r_m^2 \tag{8.2}$$

With q and m the charge and mass of the particles, V_0 and ω the RF amplitude and frequency. For safe operation, the constrain for adiabaticity parameter should be $\eta < 0.3$. By choosing an appropriate RF frequency and geometry, it is therefore possible to have an effective ion guide for a large range of masses.

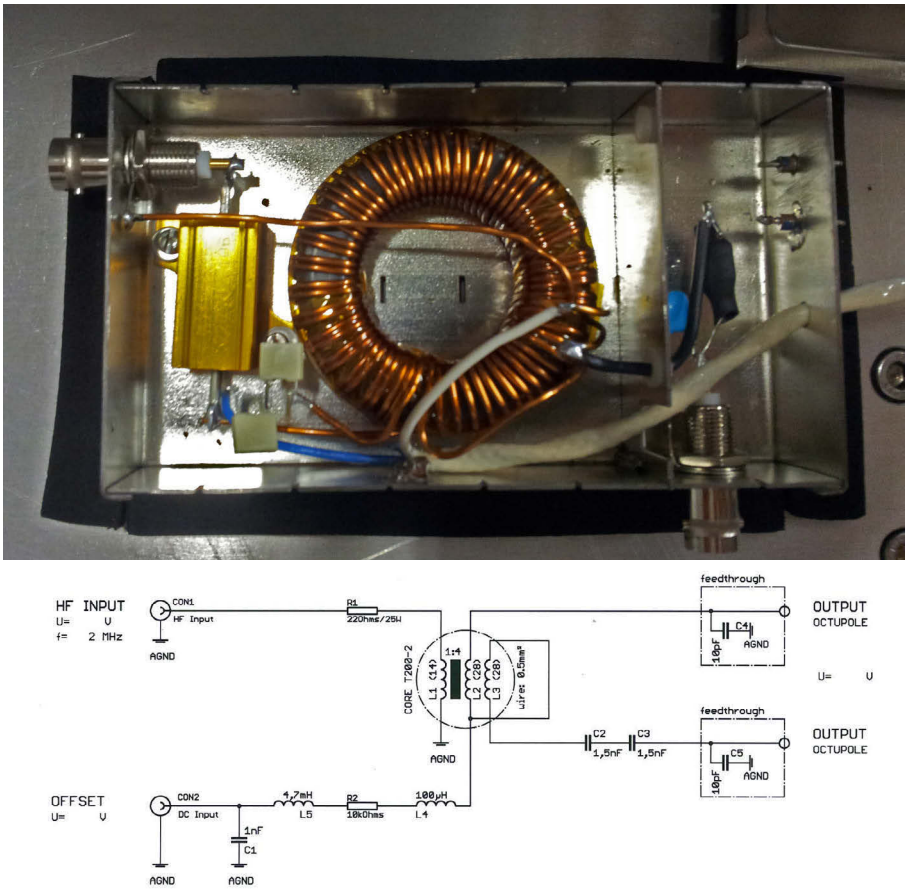

Figure 8.6: The coupling circuit used for impedance matching between the RF transceiver and the octupole bars. This coupling circuit has been designed to also allow for a DC bias to be added to the RF component. The toroidal transformer has been hand wound and is wrapped in Kapton tape in order to keep a stable winding configuration even in case of core overheating. The tuning of the LC circuit has been performed by changing the output series capacitance: the two 1.5 nF in-series capacitors can be seen to the bottom left of the transformer.

The bars of the octupole have been produced and assembled in-house. The RF voltage is provided by a Kenwood transceiver, which however does not directly connect to the octupole bars. An impedance adaptor is connected to the octupole on one side, and contains a tuned LC oscillator and a toroidal

transformer, so that it also acts to multiply the voltage that is applied on the bars. Furthermore, it is impedance matched so that reflections from the octupole bars to the transceiver are minimized, by reducing the standing wave ratio to an acceptable value of <1.5. This is accomplished by physically modifying the LC resonator circuit by changing the C part, so that reflection is minimized at around 2 MHz. In our case, geometry, frequency, and voltage have been optimized for transporting clusters with a masses of 10 u to 16 000 u.

The clusters that leave the octupole are collected by an Einzel lens that focuses them through a differential pumping pinhole, which is also biased to collimate the beam by increasing the kinetic energy, allowing it to travel a short distance without any lens: a gate valve separates the two chambers, and there is some space that must be travelled without any electrostatic element. The clusters have, by now, reached the third section.

8.3 Cluster Selection

Next, the selection stage is entered by the clusters. The bender is the first of the two main elements in this section, and it is itself necessary in order to discriminate clusters according to their charge: the mass selection part of the machine can only work if a single polarity enters, of course not considering the neutral clusters that cannot be selected. It consists (see Fig. 8.7) of four cylindrical electrodes, polarized in a quadrupole configuration, with static positive and negative voltages. The electrodes are vertically positioned, perpendicular to the beam direction. The bender is capable of separating neutral particles that, continuing their motion undisturbed, collide with a movable glass slide, positioned after the bender to protect the laser entry window.

Regarding the charged particles, in the case of a hyperbolic quadrupole field and of infinitely thin particle beams propagating along the central axis of an electrostatic deflector, it has been shown that particles can be deviated by 90° in opposite directions, without dispersion, depending on the sign of their charge [34]. Hyperbolic electrodes can be well approximated by circular electrodes, if the radius of such electrodes is chosen to be 1.15 times the distance of the electrode from the origin, and end effects are minimized if the length of the rods is at least five times the rod separation [35]. From these relations come the constrains used in constructing the electrostatic bender for this source. In any case, off-axis particles, different entrance angles, and non-monochromaticity cause some divergence to be generated during the curving motion. However, this can be corrected by placing, before and after entering the bender, two sets of 7-element electrostatic lenses (see Fig. 8.9, top left). These are used to optimize the divergence and the size of the beam, to ensure maximum transmittance in the electrostatic bender, and also to restore beam characteristics after the electrostatic bender has acted.

Particles in our setup are therefore deflected in two opposite directions according to their charge. Since electron capture during cluster production has

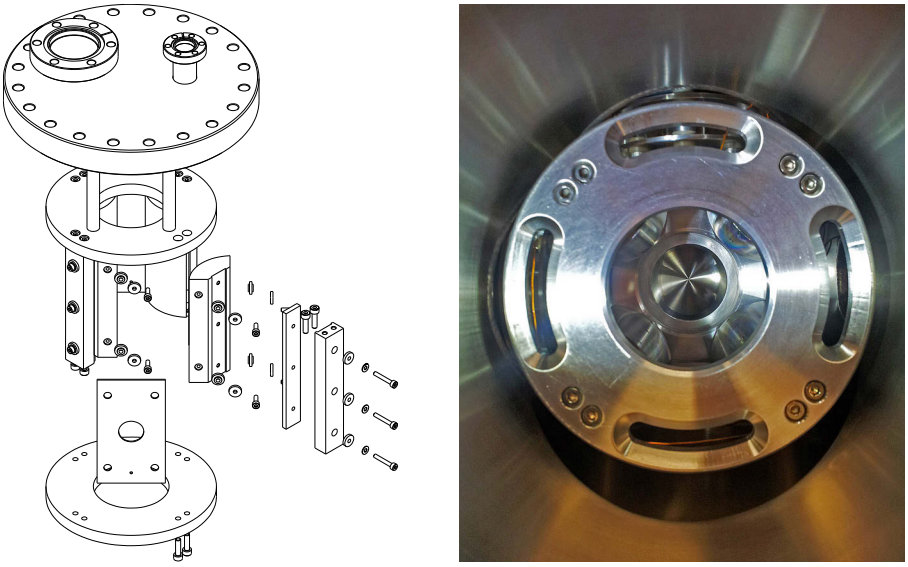

Figure 8.7: The electrostatic bender used for discriminating the clusters according to their charge. The four cylindrical plates are visible in the photograph, which is taken after installation in the bender stage UHV chamber from below.

a lower cross section with respect to electron loss, positively charged particles are preferentially created. Therefore, the system is built so that only these propagate onwards to the QMS, where the final mass selection takes place.

Subsequently, the actual size selection part of the machine is reached. The QMS that is installed is a state of the art Extrel 150QC RF-DC QMS, also acting as a last differential pumping sept before the UHV deposition chamber is reached. It is capable of selecting cluster with masses in the range 1 u to 16 000 u, which translates, for example, to clusters being made of up to 81 Au atoms, 273 Ni atoms, or 1332 C atoms. The working principle of QMSs is based on the application of a superposition of DC and an RF potentials, so that the voltage on each set of bars can be written as $\Phi = \pm(U_0 - V_0 cos(\omega t))$. The motion of the particles inside the QMS can be fully described by the Mathieu equation, whose solutions are generally interpreted and classified with the aid of the (a, q) stability diagram [33] (see Fig. 8.8). In this well known diagram, the variables a and b are defined as

$$q = 4\frac{qV_0}{m\omega^2 r_0^2} \qquad\qquad a = 8\frac{qU_0}{m\omega^2 r_0^2}$$

With r_0 the radius of a circle inscribed within the quadrupole rods. This diagram can be used to qualitatively understand the working principle of a QMS, since different regions satisfy different stability conditions [36]: considering points very close to the blue line, increasing the mass shifts the position to above

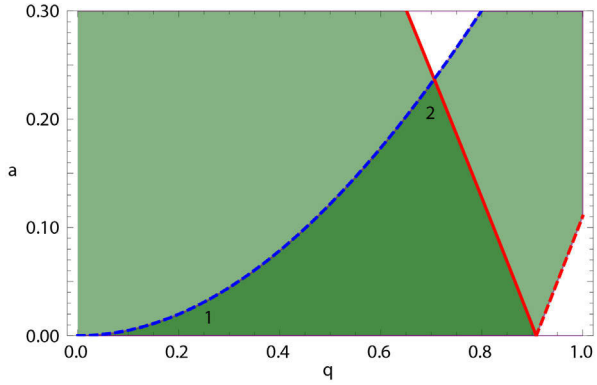

Figure 8.8: The Mathieu equation stability diagram. The darker triangular portion of the diagram corresponds to (a, q) values with stable trajectories. Points above the blue line become unstable because the static field is too large. Likewise, points to the right of the red line become unstable because the RF potential is too intense. The region marked 1 is known as the "low q" region, where the QMS acts as a low pass filter. The region marked 2 is the high resolution region.

the blue line, so that trajectories become unstable for heavier particles because the DC field is too large, causing a defocusing effect. For lighter particles, the effects of the RF potential are stronger, such that the position shifts to inside the triangular stability region, and an effective potential is able to keep trajectories stable. Considering positions close to the red line, a small decrease in mass moves the position to the right of the stability region, and the RF potential becomes too large. While lighter particles are displaced so much they eventually hit the quadrupole rods, heavier particles are transmitted. Regarding practical operating conditions, in general QMSs are operated in one of two stability regimes: the fist is in region 1 of Fig. 8.8, termed the "low q" region. Here, the adiabaticity condition is satisfied, and energy and momentum are conserved. The system acts as a low pass filter: considering increasingly large masses, the position in the diagram moves to the left of the blue line, with extremely sharp cutoffs. The second operating regime is in region 2 of Fig. 8.8. Here, the best mass resolution can be achieved, but energy and momentum are no longer conserved. Other modes of operation rely on changing V_0 and U_0 along certain paths in the Mathieu diagram, so that for example mass spectra with constant resolution can be acquired. In any case, This demonstrates how versatile this tool is, and how control over the transmitted masses can be achieved by varying only the two parameters, V_0 and U_0.

In our setup, the QMS is operated at fixed m/z when generating size-selected clusters, with mass resolution tuned by moving closer to the upper tip of the stability region. If unselected clusters are required, the "low q" region is used to achieve maximum cluster transmission.

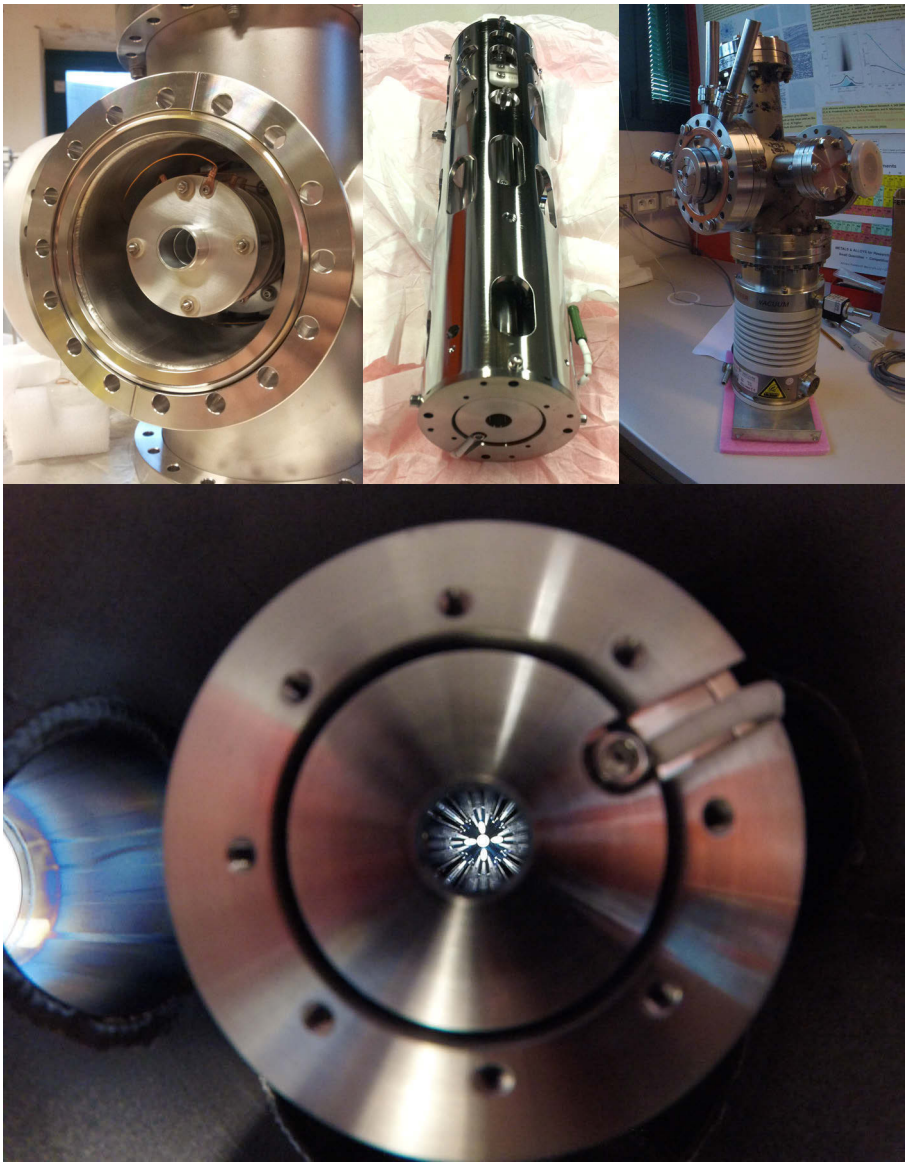

Figure 8.9: Photographs of the mass selection part of the nanocluster source. From the top left, clockwise, the transport electrostatic lenses placed at the exit of the bender, the QMS in its free standing configuration, the final vacuum chamber with the QMS mounting and pumping system, and the QMS mounted in the chamber.

After passing through the QMS, a Mo target collects the transmitted clusters. The target is connected to a Keithley model 6487/E picoammeter that,

together with custom written software, allows mass spectra to be acquired, and kinetic energy distribution curves for the clusters to be determined. Soft landing conditions can be achieved by applying a proper retarding potential to the deposition substrate: once the energy distribution curve is known, it is possible to select a retarding voltage that reduces cluster kinetic energy to below 1 eV/atom for the vast majority of the clusters, thus minimizing the possibility of atomic reordering or cluster break-up upon collision with the substrate. Pressures during operation in this stage are of the order of 10^{-7} mbar at maximum capacity.

Regarding size-selected nanocluster currents, expected values are between few tens and few hundreds of pA, depending on composition and mass of the chosen clusters, in agreement with what we have observed for Ni. This current range is already adequate for time resolved experiments. In fact, assuming a mean selected cluster current of 200 pA for single-ionized particles, this corresponds to a deposition rate of about 10^9 clusters/s. Considering a 1 mm^2 beam section, and a typical metal atomic density of 10^{15} cm^{-2}, the equivalent of 1 ML of atoms for a 10-atom cluster is deposited in about 10^3 s, corresponding to deposition times for experiments of the order of tens of minutes.

8.4 Outlook

To date, the nanocluster source at the Surface Science Laboratory is fully functional as a standalone machine. In particular, unselected Ni cluster currents of the order of 100 nA can be consistently generated, with selected currents of the order of 100 pA. Currently, one of the major points still in need of active involvement is optimization of the currents, so that a database of parameters specific for this machine can be built for different cluster sizes and different materials. Next, the connection to the experimental chambers will be of paramount importance. In the SuperESCA setup, a final set of Einzel lenses about 500 mm long, coupled with a set of bellows, will allow for the selected cluster beam to propagate in vacuum, and the clusters to be deposited *in situ*. The beam can, in this way, be focused on a particular spot on the target, where the clusters can be soft landed by applying a retarding potential. Such a transport electrostatic lens system has been chosen because of its more tunable nature with respect to RF octupoles. This is necessary since it will be placed after the QMS selection has been performed, and electrostatic lenses can be tuned for very good transmission for a selected mass. By using SIMION to simulate the electrostatic lens system (see Fig. 8.10), it has been possible to determine that 5 sections are adequate for achieving maximum transmission through the lens system for all masses of interest. This will allow the whole machine to be transported to the Surface Science Laboratory UHV chamber, and to the SuperESCA beamline, where the unique real time XPS capabilities will be applied to the study of the size-selected nanoclusters produced.

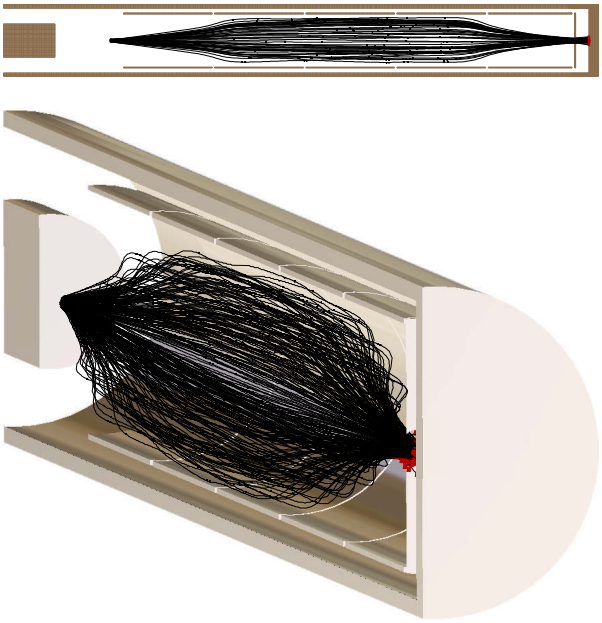

Figure 8.10: Simulations performed in SIMION for a concept 500 mm transport lens to fit inside a CF63 bellows, to be used for connecting the nanocluster source to the SuperESCA experimental chamber. Full transmission was obtained for an initial charge distribution in a 5 mm radius disk, with kinetic energy $E_K = 100$ eV, and maximum divergence half angle 8°.

References

[1] Barber, D. J.; Freestone, I. C. An investigation of the origin of the colour of the Lycurgus cup by analytical transmission electron microscopy. *Archaeometry* **1990**, *32*, 33.

[2] Wagner, F. E.; Haslbeck, S.; Stievano, L.; Calogero, S.; Pankhurst, Q. A.; Martinek, K. P. Before striking gold in gold-ruby glass. *Nature* **2000**, *407*, 691.

[3] Landman, U.; Heiz, U. *Nanocatalysis*; Springer, 2007.

[4] Atwater, H. A.; Polman, A. Plasmonics for improved photovoltaic devices. *Nature Materials* **2010**, *9*, 205.

[5] Jin, R.; Charles Cao, Y.; Hao, E.; Metraux, G. S.; Schatz, G. C.; Mirkin, C. A. Controlling anisotropic nanoparticle growth through plasmon excitation. *Nature* **2003**, *425*, 487.

[6] Anker, J. N.; Hall, W. P.; Lyandres, O.; Shah, N. C.; Zhao, J.; Van Duyne, R. P. Biosensing with plasmonic nanosensors. *Nature Materials* **2008**, *7*, 442.

[7] Maier, S. A.; Brongersma, M. L.; Kik, P. G.; Meltzer, S.; Requicha, A. A. G.; Atwater, H. A. Plasmonics—A Route to Nanoscale Optical Devices. *Advanced Materials* **2001**, *13*, 1501.

[8] Noginov, M. A.; Zhu, G.; Belgrave, A. M.; Bakker, R.; Shalaev, V. M.; Narimanov, E. E.; Stout, S.; Herz, E.; Suteewong, T.; Wiesner, U. Demonstration of a spaser-based nanolaser. *Nature* **2009**, *460*, 1110.

[9] Arvizo, R. R.; Bhattacharyya, S.; Kudgus, R. A.; Giri, K.; Bhattacharya, R.; Mukherjee, P. Intrinsic therapeutic applications of noble metal nanoparticles: past, present and future. *Chemical Society Reviews* **2012**, *41*, 2943.

[10] Roduner, E. Size matters: why nanomaterials are different. *Chemical Society Reviews* **2006**, *35*, 583.

[11] Che, M.; Bennett, C. O. In *The Influence of Particle Size on the Catalytic Properties of Supported Metals*; D.D. Eley, H. P., Weisz, P. B., Eds.; Advances in Catalysis; Academic Press, 1989; Vol. 36; pp 55.

[12] de Heer, W. A. The physics of simple metal clusters: experimental aspects and simple models. *Reviews of Modern Physics* **1993**, *65*, 611.

[13] Nosova, L.; Stenin, M.; Nogin, Y.; Ryndin, Y. EXAFS and XPS studies of the influence of metal particle size, nature of support and H_2 and CO adsorption on the structure and electronic properties of palladium. *Applied Surface Science* **1992**, *55*, 43.

[14] Tyo, E. C.; Vajda, S. Catalysis by clusters with precise numbers of atoms. *Nature Nanotechnology* **2015**, *10*, 577.

[15] Cai, J.; Ruffieux, P.; Jaafar, R.; Bieri, M.; Braun, T.; Blankenburg, S.; Muoth, M.; Seitsonen, A. P.; Saleh, M.; Feng, X.; Müllen, K.; Fasel, R. Atomically precise bottom-up fabrication of graphene nanoribbons. *Nature* **2010**, *466*, 470.

[16] N'Diaye, A. T.; Bleikamp, S.; Feibelman, P. J.; Michely, T. Two-Dimensional Ir Cluster Lattice on a Graphene Moiré on Ir(1 1 1). *Physical Review Letters* **2006**, *97*, 215501.

[17] Cavallin, A.; Pozzo, M.; Africh, C.; Baraldi, A.; Vesselli, E.; Dri, C.; Comelli, G.; Larciprete, R.; Lacovig, P.; Lizzit, S.; Alfè, D. Local Electronic Structure and Density of Edge and Facet Atoms at Rh Nanoclusters Self-Assembled on a Graphene Template. *ACS Nano* **2012**, *6*, 3034.

[18] Wu, Z.; Suhan, J.; Jin, R. One-pot synthesis of atomically monodisperse, thiol-functionalized Au_{25} nanoclusters. *Journal of Materials Chemistry* **2009**, *19*, 622.

[19] Maity, P.; Wakabayashi, T.; Ichikuni, N.; Tsunoyama, H.; Xie, S.; Yamauchi, M.; Tsukuda, T. Selective synthesis of organogold magic clusters Au_{54}(C-CPh)$_{26}$. *Chemical Communications* **2012**, *48*, 6085.

[20] Yamashita, M.; Fenn, J. B. Electrospray ion source. Another variation on the free-jet theme. *The Journal of Physical Chemistry* **1984**, *88*, 4451.

[21] Pratontep, S.; Carroll, S. J.; Xirouchaki, C.; Streun, M.; Palmer, R. E. Size-selected cluster beam source based on radio frequency magnetron plasma sputtering and gas condensation. *Review of Scientific Instruments* **2005**, *76*, 045103.

[22] Smalley, R. E. Laser Studies of Metal Cluster Beams. *Laser Chemistry* **1983**, *2*, 167.

[23] Maruyama, S.; Anderson, L. R.; Smalley, R. E. Direct injection supersonic cluster beam source for FT-ICR studies of clusters. *Review of Scientific Instruments* **1990**, *61*, 3686.

[24] Heiz, U.; Vanolli, F.; Trento, L.; Schneider, W. D. Chemical reactivity of size-selected supported clusters: An experimental setup. *Review of Scientific Instruments* **1997**, *68*, 1986.

[25] Röttgen, M. A.; Judai, K.; Antonietti, J.-M.; Heiz, U.; Rauschenbach, S.; Kern, K. Conical octopole ion guide: Design, focusing, and its application to the deposition of low energetic clusters. *Review of Scientific Instruments* **2006**, *77*, 013302.

[26] Yoon, B.; Häkkinen, H.; Landman, U.; Wörz, A. S.; Antonietti, J.-M.; Abbet, S.; Judai, K.; Heiz, U. Charging Effects on Bonding and Catalyzed Oxidation of CO on Au_8 Clusters on MgO. *Science* **2005**, *307*, 403.

[27] Heiz, U.; Vanolli, F.; Sanchez, A.; Schneider, W. D. Size-Dependent Molecular Dissociation on Mass-Selected, Supported Metal Clusters. *Journal of the American Chemical Society* **1998**, *120*, 9668.

[28] Heiz, U.; Sanchez, A.; Abbet, S.; Schneider, W. D. Catalytic Oxidation of Carbon Monoxide on Monodispersed Platinum Clusters: Each Atom Counts. *Journal of the American Chemical Society* **1999**, *121*, 3214.

[29] Häkkinen, H.; Abbet, S.; Sanchez, A.; Heiz, U.; Landman, U. Structural, Electronic, and Impurity-Doping Effects in Nanoscale Chemistry: Supported Gold Nanoclusters. *Angewandte Chemie International Edition* **2003**, *42*, 1297.

[30] Milani, P.; deHeer, W. A. Improved pulsed laser vaporization source for production of intense beams of neutral and ionized clusters. *Review of Scientific Instruments* **1990**, *61*, 1835.

[31] Scoles, G. *Atomic and molecular beam methods*; Oxford university press New York, 1988; Vol. 1.

[32] Abbett, M. Mach disk in underexpanded exhaust plumes. *AIAA Journal* **1971**, *9*, 512.

[33] Gerlich, D. *Inhomogeneous RF Fields: A Versatile Tool for the Study of Processes with Slow Ions*; John Wiley & Sons, Inc., 2007; pp 5.

[34] Zeman, H. D. Deflection of an ion beam in the two-dimensional electrostatic quadrupole field. *Review of Scientific Instruments* **1977**, *48*, 1079.

[35] Laaksonen, R. T.; Goetsch, D. A.; Owens, D. W.; Poirier, D. M.; Stepniak, F.; Weaver, J. H. Supersonic cluster source with mass selection and energy control. *Review of Scientific Instruments* **1994**, *65*, 2267.

[36] Miller, P. E.; Denton, M. B. The quadrupole mass filter: Basic operating concepts. *Journal of Chemical Education* **1986**, *63*, 617.

Acknowledgments

In some ways, this thesis is the product of three years of my life. It has been difficult at times, but always interesting and sometimes truly exciting. During this time I met many new people, colleagues and friends, who, without any doubt, contributed to this work in many different ways. In this brief chapter I would like to thank you all.
First of all I would like to express my deepest gratitude to my supervisor Alessandro Baraldi, and to the beamline scientists of the SuperESCA beamline Silvano Lizzit and Paolo Lacovig, who have always been part of my research activity in Trieste, and from whom I have had the privilege of learning how to perform experiments, since the beginning of my scientific activity.
A truly heartfelt thank you goes to my laboratory colleagues, in particular Luca Omiciuolo, who taught me a lot during the two years of PhD that we spent together. Another special mention is for Francesco Presel and Dario De Angelis, with whom I have spent a lot of time more recently, but also Harsh Bana, Elisabetta Travaglia, Luca Bignardi, Naila Jabeen, and Cristian Tache. Thank you all for the stimulating discussions, for the sleepless nights we spent working together during beamtimes, and for all the fun we have had in these three years.
My sincere thanks also go to Prof. Dr. Sebastian Günter, from the Technische Universität München, who patiently introduced me to Scanning Tunneling Microscopy, and whose support greatly helped me in my stay in Munich.
Also, I profoundly appreciated Dario Alfè's work, which truly enabled us to make some good science together. The continuous feedback with this brilliant scientist has been a true pleasure.
I would like to thank Emil Sierda, for participating in the experiments with pentacene, and for performing the SMT measurements on this system. Also, I would like to thank Holly Tetlow for her DFT calculations that motivated some of our experiments.
Finally, I would like to thank Eugenio Nicolini, with whom we actively collaborated since the beginning for the design and realization of all the parts of the

nanocluster source, and whose incredible skills have been dedicated to building the nanocluster source piece by piece.
Last but not the least, I would like to thank my family and Jessica. Thank you for supporting me through writing this thesis and through life in general.

List of Publicaitons

Peer reviewed publications

[**1**] F. Presel, N. Jabeen, M. Pozzo, D. Curcio, L. Omiciuolo, P. Lacovig, S. Lizzit, D. Alfè, A. Baraldi "Unravelling the roles of surface chemical composition and geometry for the graphene–metal interaction through C1s core-level spectroscopy" *Carbon* **93**, 187 (2015)

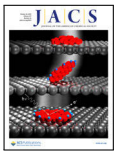

[**2**] D. Curcio, L. Omiciuolo, M. Pozzo, P. Lacovig, S. Lizzit, N. Jabeen, L. Petaccia, D. Alfè, and A. Baraldi "Molecular lifting, twisting, and curling during metal-assisted polycyclic hydrocarbon dehydrogenation" *Journal of the American Chemical Society* **138**, 3395 (2016)
The paper was featured in a spotlight article on the *Journal of the American Chemical Society*, **138**, 3253 (2016) and was awarded the cover of volume 138 (10) of JACS

[**3**] D. Curcio, E. Miniussi, P. Lacovig, S. Lizzit, R. Larciprete, J. A. Smerdon, V. R. Dhanak, R. McGrath, and A. Baraldi "Crystal to Quasicrystal Surface Phase Transition: An Unlocking Mechanism for Templated Growth" *The Journal of Physical Chemistry C* **120**, 5477 (2016)

[**4**] H. Tetlow, J. P. de Boer, I. J. Ford, D. D. Vvedensky, D. Curcio, L. Omiciuolo, S. Lizzit, A. Baraldi, and L. Kantorovich "Ethylene decomposition on Ir(111): Initial path to graphene formation" *Physical Chemistry Chemical Physics* **18**, 27897 (2016)

Submitted or in preparation manuscripts related to the PhD research project

[**1**] D. Curcio, A. Caratti, M. Pozzo, L. Omiciuolo, A. Sala, T. O. Menteş, A. Locatelli, P. Lacovig, S. Lizzit, S. Günther, D. Alfè, A. Baraldi "Growth of graphene on Ru(1 0 $\bar{1}$ 0)" *in preparation*

[**2**] D. Curcio, M. Pozzo, E. Sierda, L. Omiciuolo, F. Presel, P. Lacovig, S. Lizzit, D. Alfè, A. Baraldi "Reversible dehydrogenation of pentacene molecules on Ir(1 1 1)" *in preparation*

[**3**] F. Presel, C. A. Tache, H. Tetlow, D. Curcio, P. Lacovig, L. Kantorovich, S. Lizzit, A. Baraldi "Carbon monomers and dimers on Ir(1 1 1): and experimental and theoretical C 1*s* core level shift study" *submitted*

[**4**] H. Tetlow, D. Curcio, A. Baraldi, L. Kantorovich "Hydrocarbon decomposition kinetics on Ir(1 1 1) from first principles" *in preparation*

[**5**] J. Li, Y. Wang, D. Curcio, S. Lizzit, A. Baraldi, L. Kantorovich, A. Floris "Ethylene decomposition processes on bimetallic Ni_3Al(1 1 1) surface" *in preparation*

Other publications

[**1**] D. Curcio, L. Omiciuolo, M. Pozzo, P. Lacovig, S. Lizzit, N. Jabeen, L. Petaccia, D. Alfè, and A. Baraldi "Molecular lifting, twisting, and curling during metal-assisted polycyclic hydrocarbon dehydrogenation" *Elettra Highlights 2015-2016*